

AUTOMATIC GAIN EQUALIZATION IN WAVELENGTH-DIVISION
MULTIPLEXED COMMUNICATION SYSTEMS BY USING
FOLDED NONLINEAR-OPTICAL LOOP MIRRORS

A DISSERTATION
SUBMITTED TO THE DEPARTMENT OF APPLIED PHYSICS
AND THE COMMITTEE ON GRADUATE STUDIES
OF STANFORD UNIVERSITY
IN PARTIAL FULFILLMENT OF THE REQUIREMENTS
FOR THE DEGREE OF
DOCTOR OF PHILOSOPHY

Ueyn L. Block
December 2006

© Copyright by Ueyn L. Block 2007
All Rights Reserved

I certify that I have read this dissertation and that, in my opinion, it is fully adequate in scope and quality as a dissertation for the degree of Doctor of Philosophy.

(Martin M. Fejer) Principal Adviser

I certify that I have read this dissertation and that, in my opinion, it is fully adequate in scope and quality as a dissertation for the degree of Doctor of Philosophy.

(Michel J. F. Digonnet)

I certify that I have read this dissertation and that, in my opinion, it is fully adequate in scope and quality as a dissertation for the degree of Doctor of Philosophy.

(Robert L. Byer)

Approved for the University Committee on Graduate Studies.

Abstract

Nonlinear-optical loop mirrors (NOLMs) have historically been used primarily in applications utilizing pulsed signals, for which large peak powers are attainable, allowing for a useful nonlinear response with a relatively short fiber. However, NOLMs have not been intensively studied in applications using constant-intensity (CI) signals. When CI sources are used, the length of fiber needed to obtain modest nonlinear phase shifts can become very large. To reduce the NOLM's susceptibility to acoustic perturbations, we have folded the nonlinear loop, allowing the signals to pass through twice (once in each direction). When CI signals are used with this double-pass configuration, additional nonlinear interactions must be accounted for that, to the best of our knowledge, have never been studied.

In the research presented in this dissertation, we have studied the folded NOLM in an effort to improve its stability. The resulting improved understanding of the nonlinear effects occurring within the folded loop will have consequences for any folded-NOLM application using signals with peak and average powers of similar magnitude. To serve as a focus for our work, we chose to explore the notion of using folded NOLMs for gain equalization in optically amplified wavelength-division multiplexed (WDM) communication systems utilizing CI modulation schemes. Using this application as our motivation for developing a folded NOLM, we have observed two nonlinear effects for the first time: (1) Electrostriction-induced guided acoustic-wave Brillouin scattering (GAWBS); and (2) a phase-matched, degenerate four-wave mixing process that undermines the desired nonlinear action of the folded NOLM. Furthermore, we developed a model of the third-order nonlinear interactions in a folded NOLM that predicts the effects of (2). Using insight provided by this model, we were able to devise and demonstrate a folded NOLM that does not suffer from this effect by adding a phase modulator to one arm, thereby breaking the phase-matching condition in the folded loop. After making the aforementioned modification, we were able to demonstrate a folded NOLM that provides a power-dependent transfer function that selectively attenuates WDM channels when they become too strong, thereby providing automatic gain equalization. The proposed system does not require any feedback and can automatically adjust for system changes.

Acknowledgements

My advisors, Prof. Martin Fejer and Dr. Michel Dignonnet, deserve more credit for me being here today than the few lines of text I write here. Marty, as anyone in Ginzton Lab will tell you, is a truly amazing resource. I am still amazed at how, in just a matter of moments, he can bring himself up to speed on the details of my previous week’s work. His advice and creativity have helped me immensely. Michel, too, has been there every step of the way. His guidance was responsible for an immense portion of my work, from getting me started on my first day, to editing *every* line of this text. Because of his presence, I leave Stanford today a more capable, independent scientist than when I arrived—not to mention I’m better at fixing computers and spotting dangling participles! Thank you both.

The central gain-equalizing concept upon which this text is based was essentially handed to me by Ben Vakoc on the day I arrived. He was my primary mentor in the lab during the few years we overlapped, and I am forever thankful.

In more recent years, Stéphane Blin has provided countless hours of help debugging experiments and brainstorming on the whiteboard. I have no doubt that his presence accelerated my final two years, and only wish he had arrived sooner. Vinayak Dangui has aided me several times when I needed help. In addition to lending his mathematical ability, he helped perform countless hours of computer simulations for my “other” research project. And finally (as I sit at his old desk), Dario Falquier shared both an office and his passion for bicycles with me. I’m sure he passed on some nuggets of scientific wisdom, too, but it’s the bikes I remember most!

Which brings us to Stanford Cycling. Some of my best memories from my years here are from my time on the team. I can’t name everyone, but y’all know who you are and you’re probably not reading this anyhow! However, Art Walker might be and he really deserves to be mentioned. Art spent countless hours coaching me at the track and would accept nothing in return. That summer was the fittest and fastest I’ve ever been and I’ll always appreciate the effort he put in.

To all my friends who made life on the peninsula fun, I thank you... Learning my way around the city with Eli and Mel. Borrone with the Behroozis. Camping with Rob and Christy. TurkeyFestFeasts with Andy, Joe, Kusai, Mark, Cliff, and Kyle. Concerts with Jon and Sarah.

I wouldn't be here today without the support of my family. We have so many great memories... Singing "The Police" in the basement apartment with Dad and Kiva. Getting the Stanford sweatshirt from Connie (and proceeding to wear it daily for most of my childhood). Camping trips with Mom.

Finally, I can't possibly say enough great things about sharing my grad school experience with Jen. I've now received four degrees while we've been together (HS, BS, MS, PhD)... I promise this is the last one! She has taught me to be proud of even the smallest accomplishments along the way. She's the smiling face I rush home to every night and one of the strongest people I know. I feel like we've done it all, but also like we've barely even started. Our future has never felt brighter.

And to Jonas: Thank you for being my baby boy.

Contents

Abstract	iv
Acknowledgements	v
1 Introduction	1
1.1 Nonlinear-optical loop mirrors	1
1.2 Long-haul WDM optical communication systems	2
1.2.1 Wavelength-division multiplexing	2
1.2.2 Optical amplification	3
1.2.3 Gain equalization methods	5
1.3 Contributions of this work	8
1.4 Organization of this dissertation	9
2 Nonlinear-optical loop mirrors	11
2.1 Fiber Sagnac interferometers	11
2.1.1 Polarization evolution in fiber loop	12
2.1.2 Sagnac transfer function	13
2.1.3 3×3 coupler for improved phase sensitivity	13
2.2 Nonlinear-optical loop mirror	15
2.2.1 Nonlinear phase difference	16
2.2.2 Random polarization evolution in non-PM fiber	17
2.2.3 NOLM transfer function	17
2.2.4 Independence of WDM channels	20
2.2.5 Kerr characteristic bandwidth	20
3 Gain equalization with NOLMs	22
3.1 Cascaded loop mirrors	22
3.1.1 Asymptotic power levels	24
3.1.2 Compensation for gain inequality	26

3.2	Cascaded NALM simulations	28
3.2.1	EDFA saturation model	28
3.2.2	Chain simulations	29
3.3	NOLM amplitude instability	32
4	NOLM with folded nonlinear loop	36
4.1	Folded loop and acoustic desensitization	36
4.1.1	Acoustic pickup in Sagnac interferometers	36
4.1.2	Bias phase in folded NOLM	38
4.1.3	Nonlinear phase difference	39
4.1.4	Measurement of nonlinear phase difference	41
4.2	Amplitude stability in folded NOLMs	44
4.2.1	Arm-length mismatch	44
4.2.2	Engineering constraints	48
5	Electrostriction in folded NOLMs	51
5.1	Observation of unexpected nonlinear effects	51
5.2	Electrostriction in folded NOLM	55
5.2.1	Electrostriction in optical fibers	55
5.2.2	Electrostriction-induced polarization dynamics	57
5.3	Stimulated vibrational modes of optical fiber	60
5.3.1	Thermally induced vibrational modes	60
5.3.2	Electrostrictive stimulation of vibrational modes	61
5.4	System impact	67
6	Nonlinear response of folded NOLMs: Effects of balanced arm lengths	69
6.1	Unexpected observations in folded NOLM with balanced arms	70
6.2	Nonlinear phase shifts in folded NOLMs, revisited	73
6.2.1	Expectation value method	73
6.2.2	SPM and orthogonal, co-propagating XPM	79
6.2.3	Counter-propagating XPM	82
6.2.4	Folded loop with balanced arms	84
6.2.5	Folded loop with unbalanced arms	87
6.2.6	Inter-channel XPM	88
6.3	Intra-arm phase modulation	89
6.4	Experiments	92
6.5	Summary	97

7 Summary and discussion	99
7.1 Key developments	99
7.1.1 Gain-equalization concept	99
7.1.2 Nonlinear interactions in folded NOLMs	100
7.1.3 Electrostriction-induced acoustic modes	101
7.2 NOLM-based gain equalization: Benefits and drawbacks	102
7.3 Future research: Signal impairments	103
7.3.1 Impact of PBS and FRM on noise figure	104
7.3.2 Nonlinear signal impairments	105
A Requirement for constant-intensity signals	107
B Counter-propagating nonlinear terms ζ	110
Abbreviations	112
Symbols	114
References	115

List of Tables

3.1	Parameters used to generate Figs. 3.2, 3.3, and 3.4.	24
3.2	Parameters used for NALM chain simulations.	29
4.1	Nonlinear coefficients for linear and randomly varying SOPs.	40
5.1	Comparison of resonant frequencies from 1 st and 2 nd harmonics of f_{pm}	65

List of Figures

1.1	Point-to-point optical communication system.	3
1.2	Long-haul WDM systems with regeneration and amplification.	4
1.3	Evolution of WDM channel powers due to wavelength-dependent gain.	5
1.4	Effect of preemphasis on transmitted WDM channel powers.	6
1.5	Gain-flattening filter.	7
2.1	All-fiber Sagnac interferometer with 50% 2×2 coupler.	12
2.2	All-fiber Sagnac interferometer with 3×3 coupler.	14
2.3	Transfer functions of Sagnac interferometers with 2×2 and 3×3 couplers.	14
2.4	Nonlinear-optical loop mirrors.	15
2.5	Transfer functions of NALMs.	19
3.1	Long-haul communication system with repeated amplification.	23
3.2	Power transmitted through multiple NALM gain-loss links.	25
3.3	Transmitted power oscillates when $\Delta\phi^{nl}$ exceeds critical level.	26
3.4	NALM chain with gain variations.	27
3.5	Modeled EDFA gain spectrum vs. saturation.	30
3.6	Evolution of ten WDM signals in NALM chain.	31
3.7	Evolution of WDM signals with too much gain variation.	33
3.8	Growth of initially small amplitude modulation in NALM chain.	34
4.1	Effect of phase perturbations on folded Sagnac interferometer.	37
4.2	Polarization states in folded NALM.	40
4.3	Schematic of experiment measuring folded-NOLM phase shifts.	42
4.4	NOLM power output vs. loss asymmetry.	43
4.5	AM response of folded NALM	46
4.6	Schematic of experiment measuring nonlinear AM responsivity of NOLM	47
4.7	Experiment: AM response of NOLM	48
4.8	Amplitude stability of folded NALM vs. arm mismatch	49

5.1	Schematic of experimental setup.	52
5.2	NOLM output vs. power asymmetry for CI and 10%-DC pulses.	53
5.3	Peak-power dependence of PBS splitting ratio.	53
5.4	Schematic of NOLM with unidirectional fiber loop.	54
5.5	Electrostrictive forces and fiber deformations.	56
5.6	Effect of dynamic birefringence on folded loop.	58
5.7	Combined polarization states in folded loop.	59
5.8	GAWBS spectra for 125- μm -diameter fiber.	61
5.9	Schematic of setup used to calibrate phase modulator.	62
5.10	PBS splitting ratio vs. PM frequency.	64
5.11	Acoustic resonances versus changes in power magnitude and symmetry.	66
5.12	Magnitude of electrostrictive effects.	68
6.1	Schematic of experiment measuring $\Delta\phi^{nl}$ vs. arm mismatch.	70
6.2	Nonlinear phase difference in folded NOLM vs. arm mismatch.	71
6.3	Nonlinear phase difference in folded NOLM vs./ phase modulation.	72
6.4	Bidirectional fiber with input/output polarizers.	77
6.5	The Poincaré sphere.	78
6.6	Folded fiber loop.	84
6.7	Numerical simulation of 100 concatenated fiber sections.	85
6.8	Intra-arm phase modulation.	90
6.9	Schematic of experiment setup measuring $\Delta\phi^{nl}$ vs. intra-arm phase modulation.	91
6.10	$\Delta\phi^{nl}$ vs. PZT modulation amplitude.	92
6.11	Experimental setup used to generate Fig.'s 6.12 and 6.13.	93
6.12	NOLM switching vs. instantaneous power.	94
6.13	NOLM output vs. power at second wavelength.	96

Chapter 1

Introduction

1.1 Nonlinear-optical loop mirrors

The nonlinear-optical loop mirror (NOLM) is a common-path interferometer that utilizes the nonlinear response of an optical fiber to an applied field to modify its transmission (see Chapter 2). Since its switching ability scales with the intensity of the optical mode, it has been used primarily in applications utilizing pulsed signals, for which large peak powers are attainable, allowing for a useful nonlinear response with a relatively short fiber. Pulsed-regime applications of the NOLM include fiber-laser mode locking [1, 2], all-optical switching [3–5], pulse compression [6], wavelength conversion [7], time-division demultiplexing [8, 9], soliton transmission [10], and all-optical data regeneration [11, 12].

However, NOLMs have not been intensively studied in applications using constant-intensity (CI) signals. When CI sources are used, the length of fiber needed to obtain modest nonlinear phase shifts can become very large. The added fiber length brings an increased susceptibility to acoustic perturbations (see Sect. 4.1.1), requiring modifications to the NOLM design to improve stability of the output amplitude [8, 12]. In our research, we have *folded* the nonlinear loop to reduce acoustic pickup (see Chapter 4). The folded NOLM contains a long fiber coil through which the input signals pass twice (once in each direction). When constant-intensity signals are used, this *double-pass* configuration introduces additional nonlinear interactions that, to the best of our knowledge, have never been studied (see Chapter 6).

In the research presented in this dissertation, we have studied the folded NOLM in an effort to improve its stability. The resulting improved understanding of the nonlinear effects occurring within the folded loop will have consequences for any folded-NOLM application using signals with peak and average powers of similar magnitude. To serve as a focus for our work, we chose to explore the notion of using folded NOLMs for gain equalization in wavelength-division multiplexed (WDM) optical communication systems. Using this application as our motivation

for developing a stable NOLM, we have observed two nonlinear effects for the first time: (1) Electrostriction-induced guided acoustic-wave Brillouin scattering (Chapter 5); and (2) a phase-matched, degenerate four-wave mixing process in folded NOLMs that undermines the desired nonlinear action of the NOLM (Chapter 6). Furthermore, we developed a model of the third-order nonlinear interactions in a folded NOLM that predicts the effects of (2). Using insight provided by this model, we were able to devise and demonstrate a folded NOLM that does not suffer from this effect (Sect. 6.3).

1.2 Long-haul WDM optical communication systems

In the nearly 30 years since the first commercial fiber-optic communication system debuted, tremendous improvements in data capacity and system reach have been realized. In 1977, the Bell System began transmitting telecommunications services to customers within downtown Chicago [13, 14]. The system utilized a pair of 12-fiber ribbons to provide the bandwidth necessary to incorporate a range of services, including analog, voice, video, and 45-Mb/s data. The following three decades have brought significant improvements to every aspect of this pioneering experimental optical fiber communication system, resulting this year in a record laboratory demonstration of 14-Tb/s transmission over a single 160-km fiber [15]. Modern high-capacity transmission is possible chiefly because of two enabling technologies: wavelength-division multiplexing and optical amplification. It is the combination of these technologies that presents the challenge that this dissertation investigates, namely the difference in gain of signals with different wavelengths.

1.2.1 Wavelength-division multiplexing

A basic point-to-point optical communication system consists of a transmitter and a receiver, which are separated by a fiber that spans the distance over which the signal must travel (see Fig. 1.1(a)). The transmitter, consisting of either a directly modulated laser or a laser with an external modulator, generates light and encodes data upon it. An electrical signal carrying the data stream (not shown in Fig. 1.1) is converted to a modulation of the optical field's amplitude, phase, or frequency. The receiver performs the opposite role, converting the incoming modulated light into an electrical signal. This simple system, which operates at the wavelength of the transmitter's laser (typically around $\lambda = 1.55 \mu\text{m}$), has a maximum bit rate that is limited by a multitude of factors, including fiber nonlinearities, chromatic dispersion of the fiber, length of the fiber link, opto-electronic components, and the driving electronics.

The majority of systems being deployed today operate with channels modulated at 10 Gb/s, though 40-Gb/s and 100-Gb/s single-wavelength systems are emerging. To further increase the

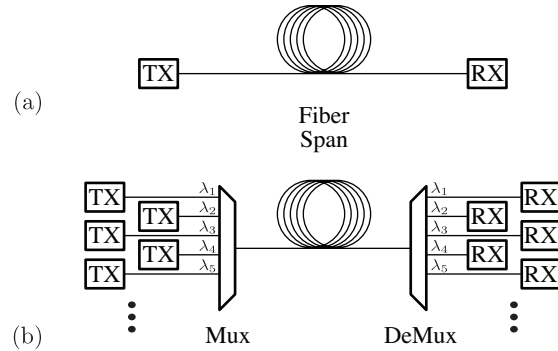


Figure 1.1: Point-to-point optical communication system.

(a) Single-channel system with transmitter (TX), receiver (RX) and fiber. (b) A wavelength-division multiplexed (WDM) system uses a multiplexer (Mux) to combine signals at discrete wavelengths λ_i onto a single fiber. After reaching the end of the fiber span, a demultiplexer (DeMux) routes each channel to a different receiver.

data-carrying capacity of an optical fiber, wavelength-division multiplexed (WDM) systems combine channels at separate wavelengths with optical multiplexers (see Fig. 1.1(b)). The channels are detected by separate receivers after being demultiplexed. The total capacity of a system with N WDM channels is NR_b , where R_b is the bit rate of a single channel.

Wavelength-division multiplexing allows large increases in transmission capacity without adding fibers to a preexisting communication link, which can be a very expensive proposition. Additionally, WDM channels can be introduced over time on an existing network, with new transmitters, receivers, and electronics purchased and installed locally only when demand increases sufficiently.

For a more detailed review of WDM networks, the interested reader is directed to Refs. [16–19].

1.2.2 Optical amplification

Through manufacturing advances, the transmission loss of single-mode optical fibers has been reduced to about 0.2 dB/km—nearly equal to the minimum theoretical attenuation level of fused silica [20]. Since this loss limits the maximum transmission distance of a single fiber span, signal regeneration or amplification is required to increase network reach beyond about 100–200 km. Traditionally, regeneration involves converting the optical signal into the electrical domain with a receiver, amplifying it electronically, and retransmitting it. This is often referred to as optical-electrical-optical (OEO) regeneration. The high-speed (≥ 10 GHz) electronics required for this operation make it an expensive endeavor, especially when you consider that each WDM channel must be detected and retransmitted separately (see Fig. 1.2(a)). Alternatively, the reach of a network may be increased by using mid-span optical amplifiers (OAs) to boost signal

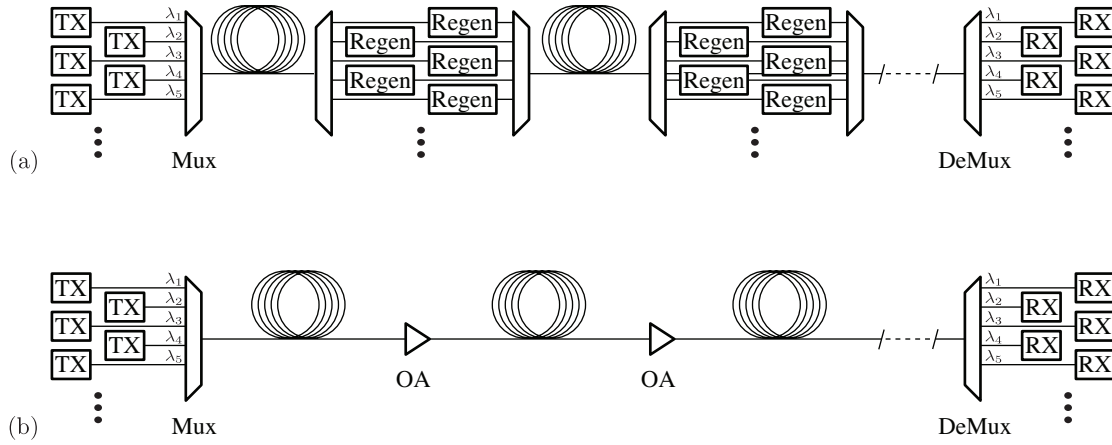


Figure 1.2: Long-haul WDM systems with regeneration and amplification.

(a) To increase network reach, WDM signals are demultiplexed, regenerated (Regen), and transmitted into next fiber span. (b) Network reach is increased by using optical amplifiers (OAs) to repeatedly boost signal power.

power (see Fig. 1.2(b)).¹ Erbium-doped fiber amplifiers (EDFAs) [22] are far and away the most common type of OA in today’s networks, though other types exist (e.g., semiconductor amplifiers and Raman fiber amplifiers). The wide bandwidth of EDFAs typically allows simultaneous amplification of all WDM channels with a single amplifier (some systems with very large channel counts do rely on separate amplifiers for each of a few bands of channels), providing a substantial cost savings compared to OEO regeneration of each channel [23].

Wavelength-dependent gain

In an ideal OA, the gain experienced by each WDM channel would be identical. In practice, however, the gain-inducing mechanism of an OA (e.g., stimulated emission, stimulated Raman scattering, etc.) is usually wavelength dependent. Therefore, two signals at different wavelengths that are launched with identical powers will not have equal power after amplification. As a result, the difference between their powers will grow with each successive amplification [22, 24, 25]. After transmission through multiple OAs with wavelength-dependent gain, the difference in the signals’ powers and signal-to-noise ratios (SNRs) will grow to unacceptable levels—the channel that experiences less gain eventually becomes too weak, with too small an SNR to be detected properly, and the info it carries is lost.

¹Optical amplifiers do not provide any signal restoration functionality other than boosting the power. OEO regenerators additionally re-shape and re-time the data stream, allowing the correction of signal distortions caused by fiber dispersion, nonlinearity, etc. All-optical (OOO) regeneration, which will allow even longer propagation distances without OEO conversion, is an active field of research [21].

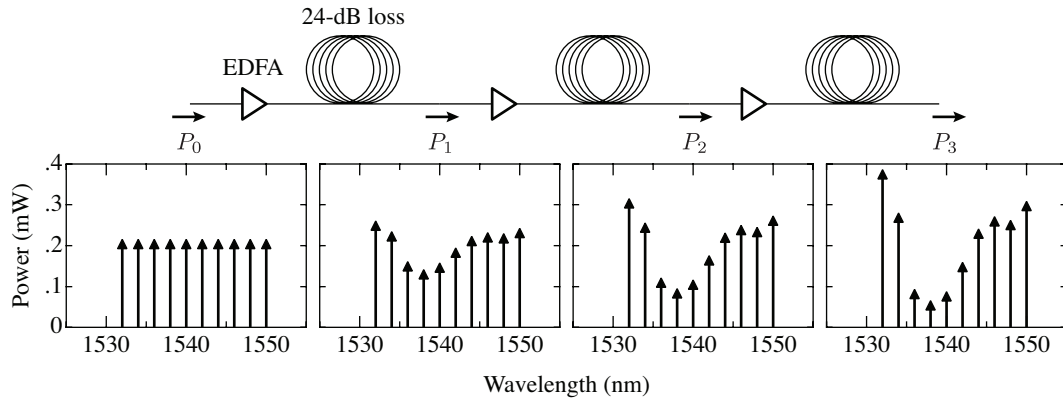


Figure 1.3: Evolution of WDM channel powers due to wavelength-dependent gain.

The powers of ten WDM channels diverge with each amplification. EDFAs are modeled using the methods presented in Sect. 3.2.1 and parameters found in Table 3.2. The EDFA gain is shown in Fig. 3.5.

As an example, we have simulated the evolution of ten WDM channels with 2-nm wavelength spacing as they propagate through three cascaded EDFAs. The modeled system is composed of EDFAs connected by approximately 120 km of fiber, resulting in a 24-dB fiber-span loss. The EDFA modeling is described in more detail in Sect. 3.2.1 (the gain spectrum is shown in Fig. 3.5). The most meaningful parameter to bear in mind for this simulation is the difference in gain between weakest-gain and strongest-gain channels, which is about 2.8 dB. Figure 1.3 shows the evolution of the WDM channel powers when the initial powers are identical. After three amplifications, the strongest channel ($\lambda = 1532$ nm) has approximately four times the power of the weakest channel ($\lambda = 1538$ nm). As this example shows, large deviations in channel powers will occur in a system that does not employ any gain equalization measures.

1.2.3 Gain equalization methods

A variety of methods have been used to compensate for the wavelength-dependent gain of optical amplifiers. In this section, we discuss the drawbacks of three gain equalization techniques: channel preemphasis, spectral filtering, and dynamic gain equalization. Understanding how these techniques work then allows us to outline how an *ideal* gain equalizer should work.

Channel preemphasis

If the total gain of an amplifier cascade is known for each WDM channel, the input power of each channel can be set such that the output powers and SNRs are similar (see Fig. 1.4) [26, 27]. This can be difficult in practice because of gain saturation, i.e., changing the input power of one

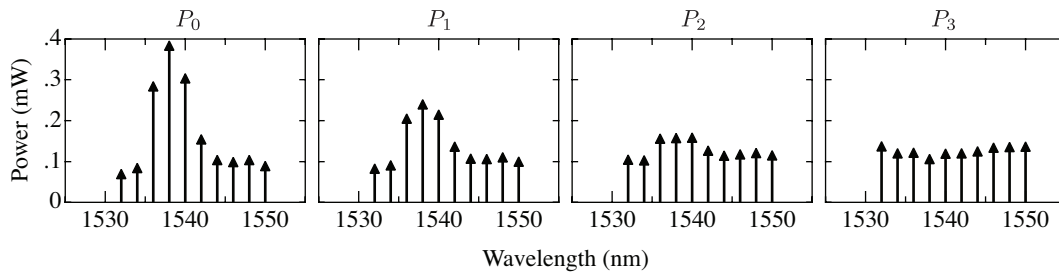


Figure 1.4: Effect of preemphasis on transmitted WDM channel powers.

The simulation shown in Fig. 1.3 is repeated using input powers that vary from channel to channel. By adjusting the input powers properly, the wavelength variation of the output spectrum can be reduced.

channel will affect the gain experienced by all channels. Telemetry can be used to relay output powers to the source, where a feedback mechanism can adjust input powers to achieve an optimal spectrum at the destination. Channel power preemphasis only provides a limited degree of gain equalization and requires active feedback to adjust for any changes in gain [24, 28].

Gain-flattening filters

An optical filter can be placed in-line with an optical amplifier to flatten its gain spectrum. The transmission spectrum of the gain-flattening filter (GFF) must closely resemble the inverse of the OA's gain spectrum in the wavelength range to be utilized (see Fig. 1.5). Alternatively, a GFF may be designed to be placed after every few amplifiers.

The two most common types of GFF are long-period fiber gratings [29–31] and dielectric thin-film filters [32, 33]. Both types of device are commonly integrated within commercial EDFA modules. The GFF is designed to flatten the amplifier gain under specific operating conditions. For a fixed set of input channel powers, gain-flattened EDFAs with gain variations as small as 0.1 dB across a 30-nm bandwidth have been demonstrated in transoceanic-scale communication systems [19, 34]. While this degree of gain uniformity is adequate for most long-haul systems, it cannot be maintained if changes in amplifier gain occur. The saturation state of an EDFA, and therefore its gain spectrum, will be different if the pump power or signal power changes. Gain-flattened amplifiers are not able to adapt to system changes such as pump deterioration and network reconfiguration. More robust solutions are desired for future networks with increased reconfigurability and reliability.

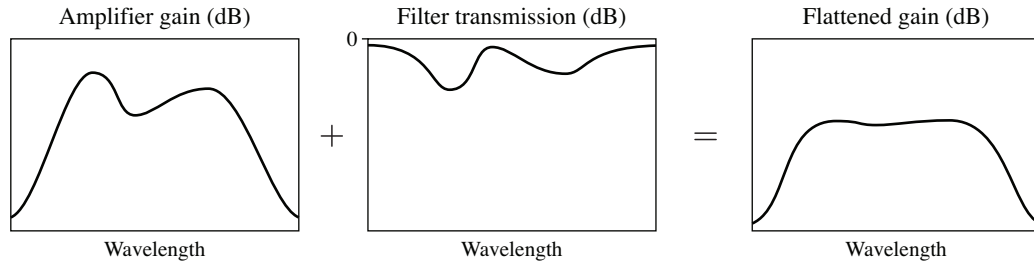


Figure 1.5: Gain-flattening filter.

By tailoring the transmission spectrum of an in-line optical filter, the net gain of an optical amplifier can be flattened.

Dynamic gain equalizers

A logical extension of gain-flattening filter technology, *dynamic* gain equalization relies upon filters with tunable transmission spectra. By monitoring the output spectrum of a network, strategically placed dynamic gain equalizers (DGEs) can be adjusted in real time to compensate for wavelength-dependent gain variations. Because of this flexibility, networks with DGEs can accommodate large system changes.

A wide variety of technologies are available (or in development) for dynamic gain equalization purposes, each of which share a common device characteristic: a voltage-controlled transmission spectrum. These technologies include tunable Bragg gratings [35], acousto-optic tunable filters [36, 37], micro-electro-mechanical systems (MEMS) [38, 39], SiO₂-based planar lightwave circuits [40–43], tunable birefringent loop mirrors [44], and tunable long-period fiber gratings [45–48], among others.

While DGE technologies offer great flexibility to the system designer, they also bring several additional drawbacks. First, feedback must be provided in order to adjust the DGE to give a specific output power spectrum. This requires signal detection, computation, and feedback electronics at each DGE, adding both cost and complexity. Second, both the feedback system and the DGE itself require electrical power. Providing the “brain” and power to control a DGE may not be of great concern for a terrestrial repeater station, but it does introduce significant challenges for distant undersea locations.

An *ideal* gain equalizer

Before presenting our research, we should first postulate how an *ideal* gain equalizer might work so that we may later use it for comparison. Let’s begin with the assumption that the optical amplifiers used do not have perfectly flat gain spectra, and state that the goal is to have equal channel powers when the signals are detected. The ideal gain equalizer would then be a device,

located either before, after, or within the optical amplifier assembly, that satisfies the following rules (in approximate order of importance):

1. The ideal DGE provides a wavelength-dependent attenuation such that the net gain is identical for each WDM channel.
2. Rule 1 is satisfied for any input WDM spectrum and amplifier gain profile.
3. The ideal DGE operates automatically, i.e., it does not require active feedback, therefore spectral monitoring is unnecessary.
4. The ideal DGE does not require electrical power (helpful for undersea repeaters).

Additionally, (just as with any optical device placed in a communication link) the ideal DGE would work for any signal modulation scheme, would be polarization independent, and would have minimal impact on the noise figure of the amplified fiber link. We must stress that we are *not* implying our device satisfies this entire list of criteria. Instead, we are simply stating that a solution with these properties would signify a distinct departure from currently available technology with multiple advantages. We will refer to this list in later chapters for comparison purposes.

1.3 Contributions of this work

The research presented in this dissertation is founded upon a simple question:

How might one devise a *nonlinear-optical* automatic gain equalizer?

To study this proposition, we focus on the nonlinear-optical loop mirror (NOLM), an all-fiber interferometer that utilizes the nonlinear interactions between signals to induce a switching behavior at its output (see Chapter 2). Preliminary investigations determined that the NOLM's transfer function might be well suited for the task if one assumes constant-intensity modulation schemes. However, significant technical hurdles were identified that had to be addressed before the NOLM could be considered for use as an automatic gain equalizer. Specifically, these issues were the NOLM's tendency to introduce intensity noise when subject to acoustic perturbations (Sect. 4.1.1) and its inherent nonlinear amplitude instability (Sect. 3.3). We determined that both of these effects could be mitigated by *folding* the loop mirror (see Chapter 4).

As is often the case in scientific research, making modifications to remove the above unwanted behavior introduced a new set of issues to be resolved. With the folded NOLM, we encountered two nonlinear effects that, to the best of our knowledge, have never been demonstrated before. First, as a consequence of the particular device configuration, we discovered that the system could stimulate resonant acoustic modes of the fiber through electrostriction (see Chapter 5).

Electrostriction also introduced an amplitude modulation at the NOLM output that would be deleterious to a communication system. Second, we discovered that a degenerate four-wave mixing process was phase matched in the long, randomly birefringent fiber in the NOLM (see Chapter 6). This unexpected result had the unfortunate consequence of eliminating the nonlinear response of the NOLM, thereby making gain equalization seemingly impossible without additional modifications to the design (Sect. 6.3). Our work represents the first published report of these effects because they are only of concern when constant-intensity signals are used.

The notion of creating a nonlinear-optical automatic gain equalizer became the framework for a detailed investigation of folded nonlinear-optical loop mirrors. We were able to overcome the two aforementioned obstacles and demonstrate the behavior necessary for gain equalization, in addition to expanding the understanding of the nonlinear processes in folded loop mirrors. As discussed in Chapter 7, further study will be required to determine whether folded NOLMs can be successfully integrated into real-world communication systems with minimal impact on signal integrity. In the “all-optical” network paradigm, a device such as the NOLM-based gain equalizer could provide much needed system functionality. However, as computational power and OEO regeneration become more affordable [49, 50], the increased availability of spectral monitoring may give the programmability of traditional DGEs an advantage in networks with the increased reconfigurability offered from having frequent OEO conversion.

1.4 Organization of this dissertation

This dissertation describes our efforts to use nonlinear-optical loop mirrors to perform gain equalization in wavelength-division multiplexed communication systems. The following chapters detail the steps taken to bring this concept to fruition.

Chapter 2 introduces the nonlinear-optical loop mirror (NOLM). We discuss using 3×3 fiber couplers for increased nonlinear phase sensitivity and provide a high-level analysis of the nonlinear phase shifts from the Kerr effect. Polarization evolution in randomly birefringent fibers is discussed, along with its effect on the nonlinear response of the fiber.

Chapter 3 describes how NOLMs perform gain equalization in a long-haul communication system by reducing the net amplification experienced by WDM channels as their power increases. Simulations are provided and the amplitude stability of the system is discussed.

Chapter 4 introduces a variation of the NOLM, namely a NOLM with a *folded* loop, that has increased amplitude stability and reduced acoustic pickup. The bias phase and nonlinear phase difference in the folded NOLM are presented. Finally, the relationship between nonlinear amplitude stability and the difference in length between the folded NOLM’s two fiber arms is discussed.

Chapter 5 begins with experimental evidence of an unexpected nonlinear effect in the folded NOLM. This effect is determined to be caused by electrostriction in the folded fiber loop. By using an input signal with long, high-power pulses, we are able to stimulate resonant acoustic modes of the fiber—the first such demonstration to be published.

Chapter 6 contains a detailed mathematical model of the third-order nonlinear effects in a long, randomly birefringent folded fiber loop. This work was necessary to explain an unexpected consequence of equalizing the folded NOLM's arm lengths, namely the disappearance of the nonlinear phase difference needed for gain equalization—this is the first report of the phase-matched degenerate four-wave mixing process that is responsible for it. The heightened understanding of the nonlinear effects in a folded loop offered by this model allows us to modify the NOLM (addition of a phase modulator) such that the nonlinear phase shift returns to its original value. At the conclusion of Chapter 6, we have demonstrated a folded NOLM with balanced arms (required for amplitude stability) with a non-zero nonlinear phase difference.

The dissertation is concluded in Chapter 7, which outlines the key developments that led to the successful demonstration of a folded NOLM-based gain equalizer. We then discuss the future research required to determine if the folded NOLM can be used in real-world networks.

Appendix A discusses the reasoning behind the requirement for constant-intensity modulation schemes. Appendix B contains a complete mathematical expression for the counter-propagating nonlinear terms in Eq. (6.22).

Chapter 2

Nonlinear-optical loop mirrors

Though it is now understood that the concept had been introduced earlier, it was Georges Sagnac’s name that was ultimately attached to the field of common-path interferometry after his experiments were published in 1913 [51]. The Sagnac interferometer, with two beams traveling in opposite directions around a common optical path, was capable of measuring rotation when the path is rotated around an axis perpendicular to its plane. In the simplest sense, the two beams travel different distances since one beam is traveling in the direction of rotation and the other beam against the direction of rotation, thus causing rotational velocity-dependent fringe shifts when they interfere.¹

This chapter discusses the use of Sagnac interferometers composed of optical fibers to accomplish functions that scale with the incident optical power. We first review the basic principles of fiber Sagnac interferometers, then introduce a power asymmetry that, through the nonlinear Kerr effect present in the fiber, provides a power-dependent phase difference between counter-propagating signals. We will describe in Chapter 3 how we use this power dependence in this dissertation to perform automatic gain equalization.

2.1 Fiber Sagnac interferometers

An all-fiber Sagnac interferometer may be constructed by connecting the two output ports of a 2×2 fiber splitter with a length of single-mode fiber (Fig. 2.1). The splitter, sometimes referred to as the “Sagnac coupler”, may be one of several types, such as a fused fiber coupler or fiber-pigtailed micro-optic component, though the [considerably less-expensive] fused variety is most commonly used. If a 50:50 splitter is used, an optical signal entering port A exits ports C and D with equal powers. These two signals counter-propagate through the fiber loop, where we refer to them as the clockwise (cw) and counterclockwise (ccw) signal, and they interfere after

¹A thorough description of the effect requires use of the General Theory of Relativity [52].

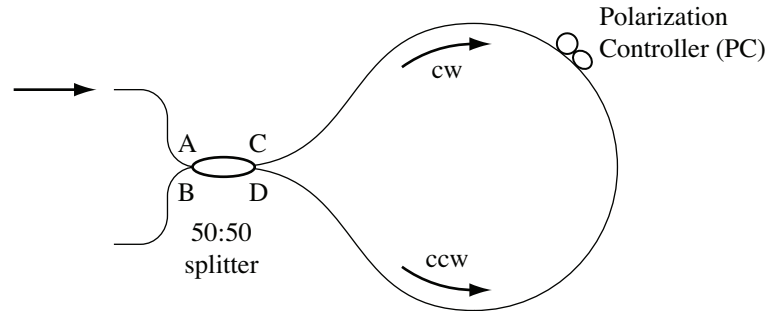


Figure 2.1: All-fiber Sagnac interferometer with 50% 2×2 coupler.

re-entering splitter ports D and C, respectively. The optical power exiting ports A and B has a ratio dependent upon their phase difference and relative state of polarization (SOP) of the two signals when they are recombined in the splitter.

2.1.1 Polarization evolution in fiber loop

It will be necessary in later chapters to have a keen understanding of the relationship of multiple signals' polarizations in fiber loops. Our work utilizes standard single-mode fibers (SMF), which have a weak, randomly varying intrinsic linear birefringence. In contrast to polarization-maintaining (PM) fibers, which are able to carry signals long distances while maintaining a linear SOP, the SOP of a signal in non-PM fibers rotates randomly during propagation [53].

In the fiber Sagnac interferometer pictured in Fig. 2.1, the cw and ccw signals are generated from the same input beam and are thus co-polarized upon entering the loop. A fiber polarization controller (PC) is used to adjust the SOP to any desired state after propagating through the loop [54]. Maximum interference is possible only when the two signals are co-polarized when they are recombined in the splitter. This state is attained when the PC is set such that the cw signal returns to the splitter at D in the same SOP as it was upon entering the loop at C. This is easily deduced by recognizing two facts: (1) Since the signals travel in the same birefringent medium (the fiber loop), which we assume is time-invariant, their polarization states have the same relationship at each location in the loop; (2) If the cw signal has the same SOP at C and D, then at D it is also co-polarized with the counter-propagating ccw signal entering the loop because the two signals enter the loop in the same SOP. Therefore, if the counter-propagating signals are co-polarized at one point, then they are co-polarized throughout the loop. When this state is attained, we say that the loop is *reciprocal* [55].

Adjusting the PC away from this setting will result in the cw and ccw signals reaching D and C, respectively, with SOPs that are not co-polarized. This will result in reduced fringe contrast at the output ports (A and B) since orthogonal portions of the signals do not interfere. The only

other PC setting that results in co-polarized interfering signals is when the counter-propagating cw and ccw signals are orthogonal throughout the loop. It is left to the reader to show that this results in co-polarized interfering signals with an added π phase difference between them.

2.1.2 Sagnac transfer function

The output fields of the fiber Sagnac interferometer may be derived for a single input power P_{in} at port A (see Fig. 2.1) by adding the fields re-entering the coupler at ports C and D after propagation through the fiber loop using the appropriate phase shifts associated with (1) propagation through the fiber loop and (2) crossing the coupler [3]. Multiplying the total field by its complex conjugate results in the output power

$$P_{out} = \frac{P_{in}}{2} [1 + \cos(\phi_{bias} + \Delta\phi)], \quad (2.1)$$

where $\Delta\phi$ is any difference in phase accumulated by the cw and ccw signals during propagation in the loop. The bias phase ϕ_{bias} depends on the output port; $\phi_{bias} = 0$ for port A and π for port B.

In general, the cw and ccw beams follow the same optical path because they are co-polarized throughout the Sagnac loop; therefore, $\Delta\phi = 0$. This simple case breaks down when the cw and ccw beams are subjected to one or more nonreciprocal effects, such as the nonlinear Kerr effect or the Faraday effect, or to a time-dependent, asymmetric perturbation such as an acoustic pressure wave (as will be discussed in Chapter 4).

As a result of one or more of the aforementioned effects, a phase difference $\Delta\phi$ may arise. For example, the sensing portion of a fiber-optic gyroscope (FOG) is a Sagnac loop, as shown in Fig. 2.1. The FOG generates a phase difference by the Sagnac effect: rotation of the FOG's Sagnac loop about its main axis yields a $\Delta\phi$ proportional to the angular velocity of rotation [56]. The output power measured at port A or B can be transformed into a rate of rotation. In this dissertation, we focus upon phase differences originating from nonlinear-optical phenomena intrinsic to the silica host material of the loop fiber.

2.1.3 3×3 coupler for improved phase sensitivity

Beyond choosing which port to use as the output, there is no simple means of changing ϕ_{bias} . Thus, the only available bias phases for a fiber Sagnac interferometer with a 2×2 coupler are zero and π . In a system where one wishes to measure P_{out} to obtain $\Delta\phi$, these bias points provide the worst possible measurement sensitivity, since when $\Delta\phi = 0$ or π the first-order response to a small change in $\Delta\phi$ is zero (see Eq. 2.1).

Alternatively, a fused 3×3 coupler may be used to yield a different bias point. In the configuration shown in Fig. 2.2, two ports of a symmetric 3×3 coupler form a fiber loop. Light entering

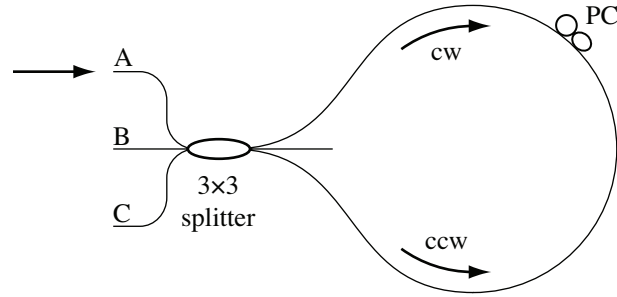


Figure 2.2: All-fiber Sagnac interferometer with 3×3 coupler.

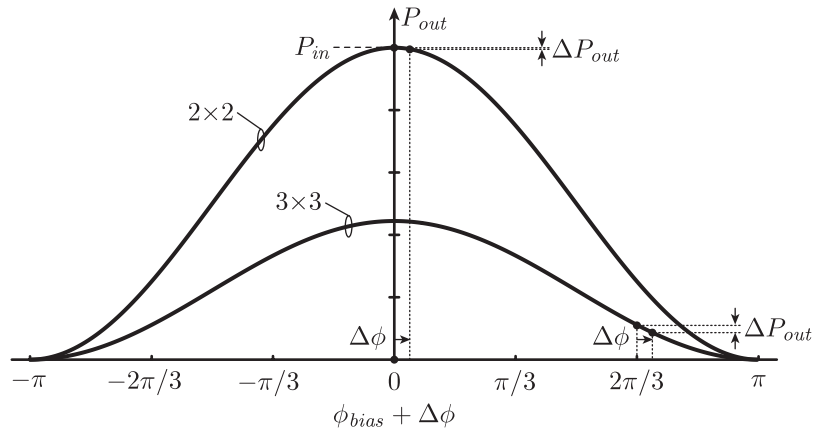


Figure 2.3: Transfer functions of Sagnac interferometers with 2×2 and 3×3 couplers.

The $\frac{2\pi}{3}$ bias from a 3×3 coupler achieves larger phase sensitivity, at the expense of lower power output.

port A is divided evenly among the three opposite ports. One-third of the input light is lost out of the unused center port on the right-hand side of the coupler. This reduction in total power is a trade-off made in order to gain the enhanced sensitivity of using a 3×3 coupler. Using the methods of [57], we find the transfer function of this configuration to be

$$P_{out} = P_{in} \frac{2}{9} [1 + \cos(\phi_{bias} + \Delta\phi)], \quad (2.2)$$

where $\phi_{bias} = 0$ for output port A, and $\pm\frac{2\pi}{3}$ for B and C. In practice, there is no way to predict which port, B or C, will have which sign. This information must be obtained empirically. The biasing advantage and reduced output power associated with using a 3×3 coupler is shown graphically in Fig. 2.3.

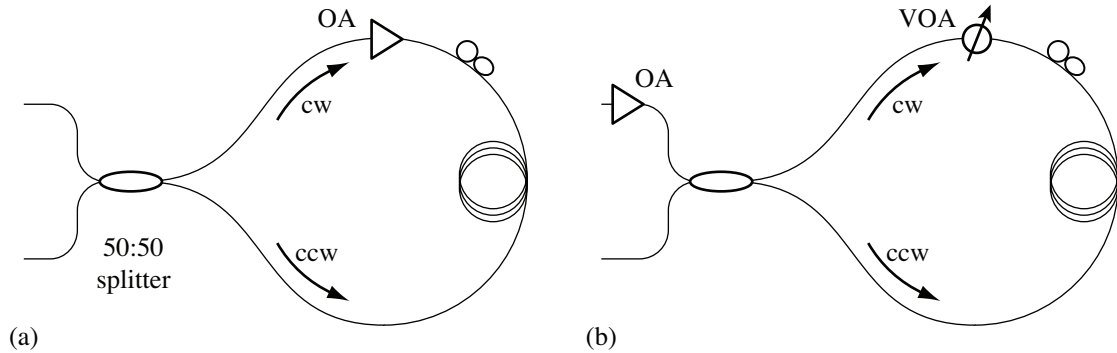


Figure 2.4: Nonlinear-optical loop mirrors.

A gain or loss element placed asymmetrically in the fiber loop generates a power difference between counter-propagating signals allowing the Kerr effect to cause a nonlinear phase difference. (a) NALM with off-center optical amplifier (OA). (b) NOLM with off-center VOA and OA at input.

2.2 Nonlinear-optical loop mirror

The fused silica that forms an optical fiber responds to an applied electric field in a complicated manner [58]. The first-order, linear response provides many common effects, such as refraction and dispersion, which are independent of the field strength. Silica, due to its non-crystalline nature, does not normally have a second-order response. The third-order response—the dipole response proportional to the product of the cube of the electric field—provides, in addition to other effects, an intensity-dependent refractive index.

The Kerr effect, as this response is commonly known, may be used to generate a power-dependent phase difference within the fiber loop of a Sagnac interferometer when the counter-propagating power is imbalanced. This imbalance may be generated in multiple ways; for instance, an asymmetric coupler could be used, which would launch more power in one direction around the loop than the other. This approach was proposed by Doran and Wood to form an ultrafast soliton switch [3], coining the term *nonlinear-optical loop mirror* (NOLM).

A power imbalance may also be created by placing an optical amplifier (OA) asymmetrically within the fiber loop [4]. As shown in Fig. 2.4(a), both cw and ccw signals will be amplified, but during propagation in the long fiber loop, the cw signal, which is amplified before traveling through the coil, will have more power than the ccw signal. The two signals will therefore accumulate different phases due to the Kerr effect. This special NOLM configuration, known as a nonlinear *amplifying* loop mirror (NALM), has the advantage of full-contrast switching due to the use of a symmetric coupler and high power from the OA.

In practice, constructing such a device—with an unisolated, bidirectional amplifier in the

loop—is not a trivial undertaking. Spurious reflections from a multitude of sources within the loop, such as splices or connectors, can cause instabilities as they travel back through the OA. Additionally, most commercially available erbium-doped fiber amplifiers (EDFAs) have isolated inputs and outputs, making bidirectional use impossible. For these reasons, we have chosen to use NOLMs that incorporate intra-loop attenuation in place of OAs to demonstrate the principles of our nonlinear gain-equalization scheme. A variable optical attenuator (VOA) replaces the OA and applies an asymmetric tunable loss to both signals upon transmission (see Fig. 2.4(b)). In this scenario, the operational principles are the same as with the NALM, and high optical powers within the loop can still be attained by placing an OA at the input to the NOLM (see Fig. 2.4(b)). The single drawback is the additional attenuation introduced by the VOA, which wastes some available optical power.

2.2.1 Nonlinear phase difference

We now present an analysis of the nonlinear phase shifts in a NALM with an intra-loop OA with gain $G > 1$. The same analysis may be used for a NOLM with a VOA by substituting G with L_{VOA} , where L_{VOA} is the optical attenuation of the VOA ($L_{VOA} < 1$). A more detailed evaluation of the phase shifts will be presented in Chapter 6. The following material is sufficient to understand the basic operation of the gain-equalization system.

A signal propagating in a fiber with nonlinear refractive index n_2 (units: m^2/W) will experience a self-induced nonlinear phase shift known as self-phase modulation (SPM). Per unit length, this nonlinear phase shift is equal to γP , where the nonlinearity $\gamma = \frac{2\pi n_2}{\lambda A_{eff}}$, A_{eff} is the fiber mode's effective area, λ is the optical signal's wavelength, and P is the signal's power [59]. There are two methods of increasing the nonlinearity of an optical fiber. First, n_2 may be increased by introducing dopants, typically germania, into the silica matrix since this parameter is an intrinsic material property [60]. Second, the waveguiding properties may be engineered to produce a more tightly confined mode with smaller A_{eff} , thus increasing the light intensity for a given total power. A combination of these two modifications has been successfully used to generate fibers with $\gamma > 20 \text{ W}^{-1}\text{km}^{-1}$, an approximate 20-fold increase compared to conventional SMF [61].

In addition to the SPM, the presence of other distinct signals generates a nonlinear refractive index as well. Cross-phase modulation (XPM) may be induced by signals at other wavelengths, in different polarization states, or traveling in the opposite direction. At this time, we are concerned with the XPM induced by a counter-propagating signal with the same linear polarization as the signal. This phenomenon is twice as efficient as SPM, resulting in $\gamma_{XPM} = 2\gamma$ [62]. It is the combination of this inequality between SPM and counter-propagating XPM effects with the imbalance between counter-propagating powers that provides a useful, nonlinear phase difference in the NOLM.

We write the nonlinear phase shifts of the signals in a NALM like that pictured in Fig. 2.4(a), then subtract them to determine the nonlinear phase difference at interference:

$$\phi^{ccw} = \gamma \frac{P}{2} \ell_{eff} + 2\gamma G \frac{P}{2} \ell_{eff}, \quad (2.3a)$$

$$\phi^{cw} = \gamma G \frac{P}{2} \ell_{eff} + 2\gamma \frac{P}{2} \ell_{eff}, \quad (2.3b)$$

$$\Delta\phi^{nl} = \gamma \frac{P}{2} (G - 1) \ell_{eff}, \quad (2.3c)$$

where P is the power input on the left side of the 2×2 coupler, G is the OA gain, and $\ell_{eff} = \frac{1}{\alpha} [1 - \exp(-\alpha\ell)]$ is the effective interaction length for a fiber loop of length ℓ with attenuation coefficient α [63]. Thus, the nonlinear phase difference scales with power and equals zero when there is no power imbalance, i.e., when $G = 1$.

In a NALM with symmetric 3×3 coupler, the input signal is evenly divided between the three coupler ports. The nonlinear phase difference is thus identical to (2.3c) after substituting a 3 for the 2 in the denominator.

2.2.2 Random polarization evolution in non-PM fiber

The analysis in Sect. 2.2.1 assumes co-linearly polarized counter-propagating signals. In non-PM fiber, the SOP is not maintained during propagation. In fact, a signal's SOP will evolve randomly during propagation through long fiber lengths since the intrinsic fiber birefringence is randomly changing along the fiber. This has the effect of reducing the magnitude of the SPM coefficient to $\frac{8}{9}\gamma$ [64–66].

In a reciprocal NOLM, the counter-propagating signals are co-polarized at all points in the loop, even though the SOP is randomly evolving along the loop (see Sect. 2.1.1). In this specific case, it has been demonstrated that the counter-propagating XPM remains precisely twice as strong as SPM [67]. Therefore, the conclusions in Sect. 2.2.1 are unchanged, other than the inclusion of an overall factor of $\frac{8}{9}$ reducing the magnitude of the nonlinear phase difference.

Since this result also applies to the folded NOLM, which is introduced in Chapter 4, a detailed derivation of this result is performed in Chapter 6. The simpler case in this section is presented without demonstration and may be inferred after one gains an understanding of Chapters 4 and 6.

2.2.3 NOLM transfer function

The switching behavior of a NALM with 2×2 coupler is described by inserting (2.3c) into (2.1), resulting in

$$P_{out} = G \frac{P_{in}}{2} \left[1 + \cos \left(\phi_{bias} + \frac{8\gamma}{9} \frac{P_{in}}{2} (G - 1) \ell_{eff} \right) \right]. \quad (2.4)$$

In the limit of zero nonlinear phase shift (e.g., with a short fiber loop or low intensity), the NALM returns all light to the same port as it entered ($\phi_{bias} = 0$). It is this behavior for which the device earned the moniker “loop *mirror*”. The presence of a nonlinear phase difference switches some or all of the light into the second output port ($\phi_{bias} = \pi$).

Similarly, by inserting (2.3c) in (2.2) we obtain the transfer function for a NALM with a 3×3 coupler:

$$P_{out} = GP_{in} \frac{2}{9} \left[1 + \cos \left(\phi_{bias} + \frac{8\gamma}{9} \frac{P_{in}}{3} (G-1) \ell_{eff} \right) \right], \quad (2.5)$$

with possible bias phases of zero and $\pm 2\pi/3$ for the three output ports.

Nonlinear loop mirrors are typically used in situations where switching between output ports is desired when a change in input power occurs. This behavior is demonstrated in Fig. 2.5(a), where $P_0 = \frac{2\pi}{\frac{8\gamma}{9}(G-1)\ell_{eff}}$ is the input power required for full switching between the output ports of a NALM with a 2×2 coupler. In comparison, a NALM with a 3×3 coupler switches the output power between three output ports; but 100% switching requires a higher power ($1.5 \times P_0$) due to the insertion loss associated with the unused right-hand coupler port (see Fig. 2.5(b)).

In Chapter 4, we will present a novel loop mirror configuration in order to improve the amplitude stability of the output signal; the *folded* NOLM incorporates a Faraday rotator mirror (FRM) at the end of a double-passed length of optical fiber. As will be detailed in Chapter 4, one benign side-effect of the FRM is the addition of a π phase difference between counter-propagating signals. Since this phase difference is constant, it may be added to ϕ_{bias} in (2.4) and (2.5), therefore inverting the curves in Figs. 2.5(a) and 2.5(b), respectively. The resulting transfer function for a 2×2 NALM simply has the two output ports’ functions reversed (see Fig. 2.5(c)). In a 3×3 NALM, though, the powers exiting the $\phi_{bias} = \pm 2\pi/3$ ports experience a three-fold increase near $P_{in} = 0$ while maintaining identical slopes (see Fig. 2.5(d)). This fortuitous behavior increases the utility of the folded NOLM.

In applications where the nonlinear phase shifts are small, either due to low power or small fiber nonlinearity and/or length, the large phase sensitivity of the 3×3 coupler’s $\pm 2\pi/3$ ports provides increased switching magnitude (see Fig. 2.5). At the other extreme, when $\Delta\phi^{nl}$ is large, a loop mirror with a 2×2 coupler can achieve full contrast switching with a larger output power, in addition to increased switching per watt of input power. Most published reports of NOLMs consider uses with pulsed signals and large peak power [3–5, 7, 10, 11]; for this reason, the benefits of a 2×2 coupler make it optimal in these situations.² Our research applies to constant-intensity (CI) modulation techniques (e.g., phase or frequency modulation) with only modest power levels, typically under 100 mW. The small nonlinear phase shifts generated under such conditions benefit from the characteristics of a system based on a 3×3 coupler.

²When using pulsed signals, one must consider the difference between instantaneous (P_{peak}) and average (P_{avg}) powers in (2.3), since the counter-propagating XPM will scale with average power. When $P_{avg} \ll P_{peak}$, the XPM terms may be neglected, thus changing the sign of (2.3c).

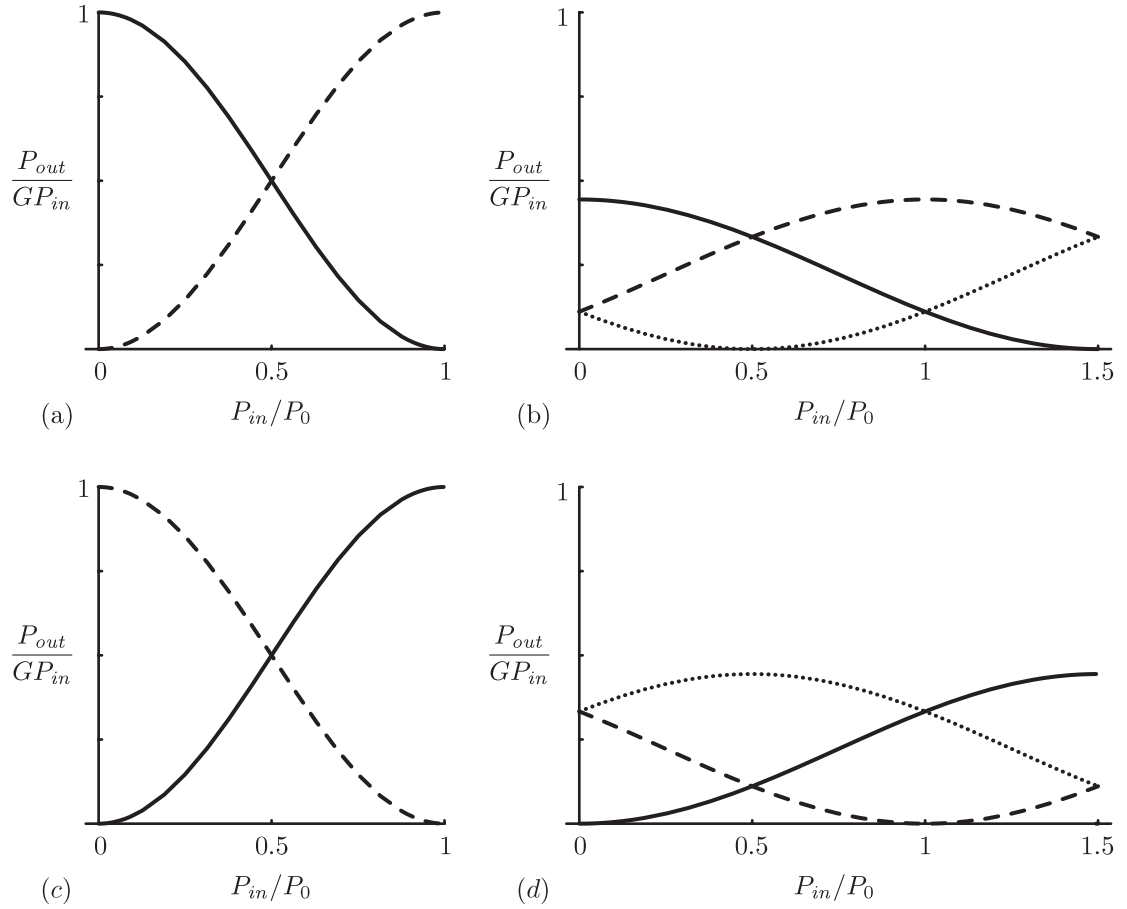


Figure 2.5: Transfer functions of NALMs.

NALM with (a) 2×2 coupler, output ports $\phi_{bias} = 0$ (solid) and π (dashed), and (b) 3×3 coupler, output ports $\phi_{bias} = 0$ (solid), $+2\pi/3$ (dashed), and $-2\pi/3$ (dotted). Folded configuration of NALM adds a π phase difference, inverting transfer functions for each output port: folded NALM with (c) 2×2 coupler, (d) 3×3 coupler. All input powers are normalized to the 2×2 full-switching power $P_0 = 2\pi / \left[\frac{8\gamma}{9} (G - 1) \ell_{eff} \right]$.

2.2.4 Independence of WDM channels

In this dissertation, as described in Chapter 3, we propose using NOLMs for automatic gain equalization in wavelength-division multiplexed (WDM) communication systems. Thus far, we have shown how a NOLM responds to the presence of a single input signal, but we must now concern ourselves with the interaction of multiple input signals centered at discrete frequencies. As in Sect. 2.2.1, we will focus on the simplest case of co-linearly polarized signals, which is only attainable in long fibers if they are PM. Again, we save the extension to non-PM fibers with randomly varying SOPs for Chapter 6.

We begin the discussion by defining two input channels with wavelengths $\lambda_1 \neq \lambda_2$ in the NALM pictured in Fig. 2.4(a). We must determine if there is any nonlinear phase difference imparted upon one signal due the presence of the second—without loss of generality, we investigate $\Delta\phi_1(P_2)$, where P_2 is the input power at λ_2 . The cw and ccw signals at λ_2 will nonlinearly interact with both counter-propagating λ_1 signals. Cross-phase modulation between signals at different wavelengths is twice as efficient as SPM for both co- and counter-propagating signals [68]. Writing the nonlinear phase shifts of the two counter-propagating λ_1 signals as a sum of co- and counter-propagating power at λ_2 , respectively, we arrive at

$$\phi_1^{ccw} = 2\gamma\frac{P_2}{2}\ell_{eff} + 2\gamma G\frac{P_2}{2}\ell_{eff}, \quad (2.6a)$$

$$\phi_1^{cw} = 2\gamma G\frac{P_2}{2}\ell_{eff} + 2\gamma\frac{P_2}{2}\ell_{eff}. \quad (2.6b)$$

Subtracting these two equations yields the nonlinear phase difference $\Delta\phi_1^{nl}(P_2) = 0$. Therefore, the nonlinear switching of a single WDM channel will not be affected by the presence of other channels.

The above statement is true when one considers the OA to be *ideal*, in particular with constant gain G . In reality, the embedded OA will saturate as a function of the total optical input power. Thus, changing the input power at λ_2 will change the NALM output power at λ_1 , but only due to amplifier saturation. The switching between output ports, and therefore the ratio of those ports' powers at a single wavelength, is only a function of the counter-propagating power at that wavelength. This value is, of course, a function of amplifier saturation—so there is some coupling between channel output powers. This effect—which does not pose a problem to the system's operation, but does complicate the analysis—will be discussed in more depth in Chapter 3.

2.2.5 Kerr characteristic bandwidth

The question must be asked: what is the minimum frequency separation $\Delta\nu$ between two co-propagating WDM channels for their Kerr interaction to be considered *cross*-phase modulation?

In other words, as $\Delta\nu$ approaches 0, eventually the total power $P_1 + P_2$ will act as one signal with SPM being the only nonlinear interaction between co-propagating signals. If this occurs, the first terms on the right-hand sides of (2.6a) and (2.6b) must be divided by two, resulting in $\Delta\phi_1^{nl}(P_2) \neq 0$. Thus neighboring WDM channels will impart nonlinear phase shifts upon each other and each channel's transfer function is no longer independent of the others.

The answer to this question, i.e., the differentiation between SPM and XPM, is intrinsically linked to fiber length and dispersion [69, 70]. A characteristic bandwidth may be defined for the Kerr effect in a fiber loop as

$$\Delta\nu_0 = \frac{1}{2\pi} \sqrt{\frac{|A|}{\ell}}, \quad (2.7)$$

where ℓ is the length of the fiber and A is the group-velocity dispersion, defined by $A^{-1} = d^2\beta/d\omega^2$, where β is the signal's propagation constant and ω is the angular frequency of the signal. Self-phase modulation occurs in the regime $\Delta\nu \ll \Delta\nu_0$, while signals separated by $\Delta\nu \gg \Delta\nu_0$ interact with XPM. As discussed above, the lack of an XPM effect would eliminate the independence of WDM channels.

We can now place practical limitations on the WDM channel spacing, bandwidth, and fiber choice. Fiber dispersion, typically reported as $D = \frac{-2\pi c}{\lambda^2} A^{-1}$, must be small enough that the entire bandwidth of a single WDM channel falls within $\Delta\nu_0$, but large enough that the separation between neighboring channels $\Delta\nu_{WDM} \gg \Delta\nu_0$. Since a single channel's bandwidth is a function of the data encoded upon it, the fiber parameters must be chosen appropriately. The bandwidth required for detection can be as large as six times the bit rate R_b for some modulation schemes [71], though increasing spectral efficiency toward (or beyond) 1 bit/Hz is one of the drivers of coherent communication methods. By assuming a near-unity spectral efficiency, we require $R_b \ll \Delta\nu_0$, i.e., the Kerr characteristic bandwidth is larger than the signal bandwidth.

Fiber dispersion commonly lies in the range $0 < |D| < 20$ ps nm⁻¹km⁻¹. If we choose $D = 5$ ps nm⁻¹km⁻¹—a value possible with non-zero dispersion-shifted fiber (NZ-DSF)—and a 1-km fiber loop, the resulting Kerr bandwidth $\Delta\nu_0 \approx 60$ GHz would be appropriate for modern WDM system with channel spacing $\Delta\nu_{WDM} \approx 100$ GHz and bit rate $R_b \approx 10$ GHz.

Chapter 3

Gain equalization with NOLMs

In this chapter, we propose a method of automatic gain equalization that utilizes NALMs in place of standard OAs in a long-haul WDM optical communication system. The NALM's channel-independent, nonlinear transfer function introduced in Chapter 2 returns an output power for each WDM channel that is a function of its input power. We will use this ability to construct a system in which each WDM channel experiences a gain that depends on its input power, lower powers experiencing a higher gain and vice versa, so that the powers of all channels converge to a similar level after multiple amplifications. We will show that this behavior occurs passively, making channel monitoring and feedback unnecessary.

For simplicity, all examples in this chapter consider NALMs with embedded OAs. All concepts presented can also be applied to a system using NOLMs with intra-loop attenuation, with only slight modification of the analysis necessary. Later chapters use this second arrangement for ease and additional flexibility in experimentation.

Finally, all communication signals presented henceforth are assumed to be constant-intensity (CI). This assumption prohibits the use of amplitude-modulated systems and requires either phase- or frequency-modulation schemes. The reasons for this requirement are discussed in Appendix A.

3.1 Cascaded loop mirrors

The intrinsic attenuation of an optical fiber at wavelengths near $1.5 \mu\text{m}$ is small (typically < 0.2 dB/km), but its presence limits the geographical range of a single communication trio, consisting of transmitter, fiber, and detector. To increase this range, launch power may be increased to a point, but practical considerations will limit the maximum possible launch power. For instance, parasitic nonlinear effects such as four-wave mixing and stimulated Brillouin scattering require power levels to remain below a certain level [72, 73]. To traverse long distances, mid-span optical

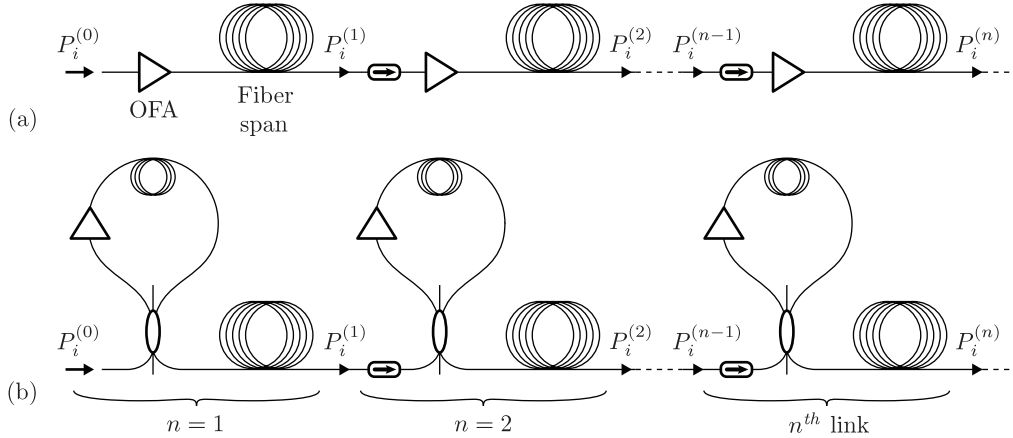


Figure 3.1: Long-haul communication system with repeated amplification.

- (a) Chain of gain-loss links; OAs boost the optical power repeatedly between long fiber spans. (b) OAs replaced with NALMs in proposed system with automatic gain equalization.

amplifiers (OAs) and fiber lengths are chained repeatedly, forming a long communication line containing multiple links, each of which is typically 50 to 100 km in length (see Fig. 3.1(a)).

In our novel system, we propose replacing each OA with a NALM, as shown in Fig. 3.1(b). The NALM serves two purposes: It provides (1) amplification to the WDM signals and (2) automatic gain equalization through the nonlinear switching behavior. The output power of the n^{th} gain-loss link in Fig. 3.1(b) is determined by multiplying (2.5) by the signal loss from the fiber link L_{link} :

$$P_i^{(n)} = GL_{link}P_i^{(n-1)}\frac{2}{9}\left[1 + \cos\left(\phi_{bias} + \frac{8\gamma P_i^{(n-1)}}{9}\frac{(G-1)\ell_{eff}}{3}\right)\right], \quad (3.1)$$

where i denotes the nominal WDM channel number. The link loss L_{link} contains the attenuation associated with the fiber span and NALM fiber loop, in addition to the insertion losses of any other components.

The astute reader can now grasp the fundamentals of the gain-equalizing concept from (3.1). If ϕ_{bias} is chosen correctly, the NALM will provide a level of gain to each channel that is a function of its power. Thus, strong signals will receive more loss than weak ones. This is accomplished because the NALM switches power away from one output coupler port (the one connected to the following link) to the two other ports. The optical isolators between links (see Fig. 3.1) prevent light switched back through the input port to reach the previous NALM, which would upset its operation. Thus the NALM chain cannot be operated bidirectionally.

Table 3.1: Parameters used to generate Figs. 3.2, 3.3, and 3.4.

Parameter	Value
γ	$20 \text{ W}^{-1}\text{km}^{-1}$
ϕ_{bias}	$\pi/3$
L_{link}	-20 dB
ℓ_{loop}	500 m
α_{loop}	-0.5 dB/km
L_{loop}	-0.25 dB
ℓ_{eff}	486 m

3.1.1 Asymptotic power levels

The signals' powers transmitted through the amplifier chain of Fig. 3.1(b) may be analyzed by repeatedly operating the transfer function (3.1) upon the input powers $P_i^{(0)}$. We perform this procedure for a NALM chain with parameters shown in Table 3.1. The gain has been fixed at 28 dB, thus lacking any saturation effects; though not realistic, this is done without loss of generality to simplify the illustration of the gain-equalizing principle. The total link loss has been set equal to -20 dB, which includes 0.25 dB from the highly nonlinear (HNL) fiber in the NALM, thus leaving 19.75 dB for the fiber span between NALMs and component losses. This is equivalent to a fiber span of nearly 100 km of standard fiber at -0.2 dB/km. The $\pi/3$ bias phase is achieved using a 3×3 coupler and a folded nonlinear loop (see Chapter 4).

The result of the above analysis is shown graphically in Fig. 3.2. The transfer function (3.1) is plotted in Fig. 3.2(a) along with a line signifying $P^{out} = P^{in}$. A dotted line is traced vertically from the input power of the i^{th} channel, $P_i^{(0)}$. The ordinate of the point where this line intersects the transfer function curve is, by definition of this curve, the output of the first link $P_i^{(1)}$. This value becomes the input of the second link, so we trace horizontally to the $P^{out} = P^{in}$ line and repeat this process for the second link of the chain. After several iterations, i.e., propagating through several links, the power approaches a stable steady-state value $P_i^{(\infty)}$.

This simple graphical illustration demonstrates the important fundamental premise of this work: After just a few links (i.e., amplifiers), the signal power traveling through the transmission line reaches an asymptotic value, and this asymptotic value *remains the same* for the rest of the transmission line, however long it might be. Furthermore, by repeating this graphic example with a different input power $P_i(0)$, it is easy to show (and see by simply looking at Fig. 3.2(a)) that the steady-state value $P_i^{(\infty)}$ is *independent of the input power* $P_i(0)$.

Furthermore, if multiple signals with different wavelengths but the same OA gain are launched

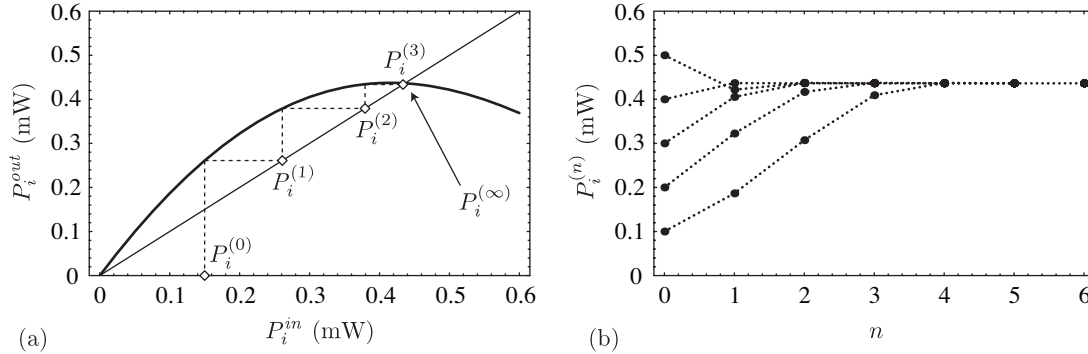


Figure 3.2: Power transmitted through multiple NALM gain-loss links.

Analysis parameters are found in Table 3.1 with $G = 28$ dB. (a) Graphical representation of asymptotic power level. (b) Evolution of five signals with varying input powers.

into the chain, they all approach $P_i^{(\infty)}$ after several gain-loss links and remain at that level indefinitely¹ (see Fig. 3.2(b)). Thus, the chain of cascaded NALMs is able to equalize the transmitted power of multiple signals with different input powers.

The steady-state power $P_i^{(\infty)}$ can easily be found analytically by solving the transfer function $P_i^{(n)} = P_i^{(n-1)}$:

$$P_i^{(\infty)} = \frac{27}{8\gamma(G_i - 1)\ell_{eff}} \left[\cos^{-1} \left(\frac{9}{2G_i L_{link}} - 1 \right) - \frac{\pi}{3} \right]. \quad (3.2)$$

If we increase the gain to 30 dB in the above analysis, we observe that the asymptotic-power analysis breaks down (see Fig. 3.3). The resulting oscillating power behavior occurs because the transfer function's slope has increased to a magnitude greater than 1 at $P_i^{in} = P_i^{(\infty)}$, therefore preventing the transmitted power to stabilize at $P_i^{(\infty)}$. When this occurs, the power of a signal fluctuates around $P_i^{(\infty)}$ indefinitely.²

Setting the derivative d/dP_{in} of (3.1) equal to -1 and inserting (3.2), we can define the condition where this behavior is initiated:

$$\frac{9}{2G_i L_{link}} = 1 + \cos \left(\frac{6}{\sqrt{4G_i L_{link} - 9}} + \frac{\pi}{3} \right). \quad (3.3)$$

The solution $G_i L_{link} \approx 9.775$ states that the oscillatory behavior will exist if the OA gain exceeds the link-loss magnitude by more than 9.9 dB ($10 \log_{10} 9.775 \approx 9.9$ dB). The onset of this behavior

¹While we say that channel power stays at $P_i^{(\infty)}$ indefinitely, it should be implicitly understood that the power of a channel varies within a single gain-loss link (i.e., it is strong after the OA and gets weaker as it propagates along the fiber span). We only show the power level between gain-loss links in Fig. 3.2(b); it is the power as measured at these discrete locations that remains "constant".

²If the launched power is *precisely* equal to $P_i^{(\infty)}$, it will be maintained indefinitely. Of course, it is highly unlikely that this would happen in practice, and there will certainly be some variation in parameters from link to link, so it is a purely academic concept.

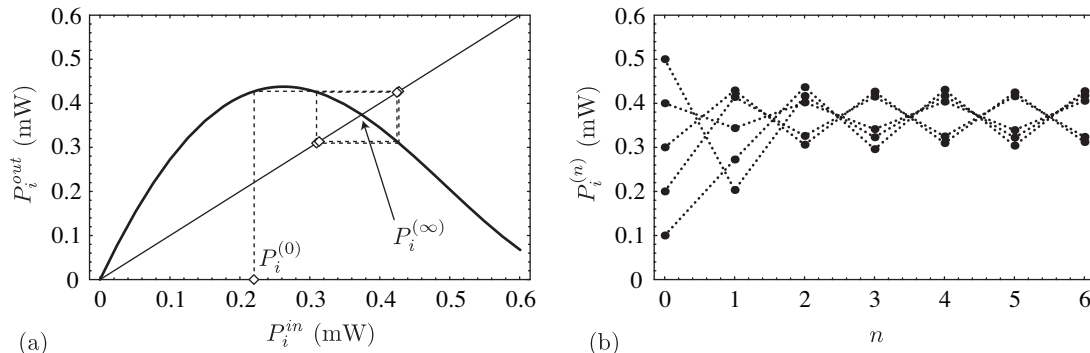


Figure 3.3: Transmitted power oscillates when $\Delta\phi^{nl}$ exceeds critical level.

Analysis parameters are found in Table 3.1 with $G = 30$ dB. (a) Graphical representation of oscillating power level. (b) Evolution of five signals with varying input powers.

identifies the maximum OA gain allowable in the system.³ Notice that this limit appears to be independent of fiber nonlinearity. In practice, though, the nonlinearity affects the steady-state power (3.2), which changes G_i through amplifier saturation, thereby coupling the upper gain limit and the fiber nonlinearity.

The minimum tolerable gain occurs when the OA gain equals the link loss plus insertion loss associated with the 3×3 coupler. When biased at $\pi/3$ and $\Delta\phi^{nl} = 0$, one-third of the light entering the 3×3 coupler will be transmitted into the fiber span—an insertion loss of 4.77 dB. Therefore, the link will stay stable provided $G_i L_{link}$ remains between 4.77 dB and 9.9 dB, or a maximum gain span $\Delta G_{max} \approx 5.13$ dB. This shows that when using a 3×3 coupler, an asymptotic power solution is found when the OA gain is within about a 5 dB range of values, whose level is dictated by the link loss (including the insertion losses of the components in the NALM).

3.1.2 Compensation for gain inequality

The true function of the cascaded NALM chain is to balance the gain experienced by WDM channels when the OAs have non-uniform gain spectra. The particular OAs used may generate gain from a variety of phenomena, be it stimulated emission, Raman gain, etc. In all cases, wavelength-dependent gain variations will cause WDM channel powers to diverge after repeated amplifications, therefore necessitating a gain-equalization solution.

The steady-state power $P_i^{(\infty)}$ for channel i in a NALM chain is a function of the operating parameters, including gain. When the gains of channels i and j differ ($G_i \neq G_j$), each channel will seek a unique power level after repeated amplifications ($P_i^{(\infty)} \neq P_j^{(\infty)}$). To illustrate this point, we show the transfer function for five OA gain values in Fig. 3.4(a) using the parameters in

³This is a “soft” limit since a small amount of oscillation may be acceptable.

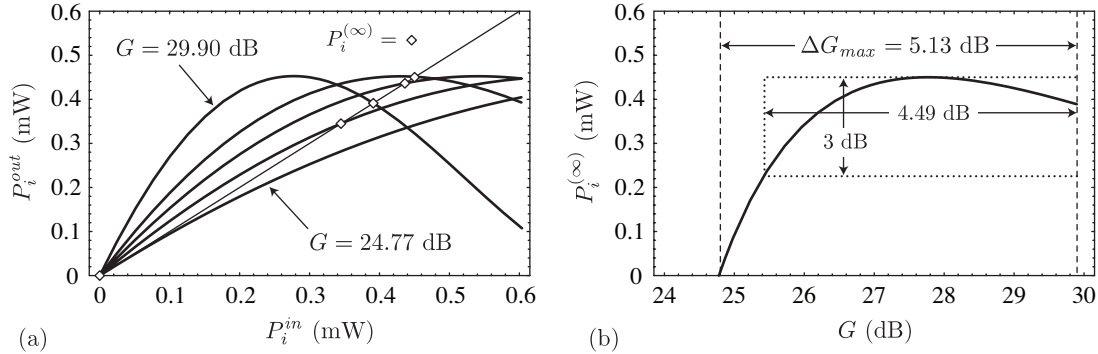


Figure 3.4: NALM chain with gain variations.

Analysis parameters from Table 3.1. (a) Steady-state power level $P_i^{(\infty)}$ varies with gain; $G = 24.77$, 26, 27, 28, and 29.9 dB shown. (b) $P_i^{(\infty)}$ as a function of gain; maximum allowable gain variation is 5.13 dB (4.49 dB if channel powers are required to differ by less than 3 dB).

Table 3.1. When $G \approx 24.77$ dB, the OA gain is just large enough to overcome the insertion loss associated with the 3×3 coupler plus the link ($L_{link} = 20$ dB). This is the minimum allowable gain, since $P_i^{(\infty)} = 0$. As G is increased, $P_i^{(\infty)}$ increases until it reaches a maximum, then declines slightly before reaching $G \approx 29.9$ dB—the upper gain limit, above which oscillatory behavior exists.

By solving (3.1) for G when $P^{out} = P^{in}$, the steady-state power versus G may be determined and is shown in Fig. 3.4(b). This curve may be used to determine the power levels of WDM channels if their gains are known. As can be seen, individual channels *do not* maintain identical powers unless they have equal gain. But more importantly, the WDM channel powers *will not diverge* with repeated amplifications—each will approach a unique $P_i^{(\infty)}$ that depends on its OA gain and remain at that level indefinitely. This state may exist as long as the WDM channel gains vary by no more than $\Delta G_{max} \approx 5.13$ dB (see Sect. 3.1.1). If any two channels have an OA gain difference larger than ΔG_{max} , either the channel with more gain will exhibit oscillatory behavior, the channel with less gain will approach $P_i^{(\infty)} = 0$, or both will occur. Therefore, $\Delta G_{max} \approx 5.13$ dB defines the maximum amount of OA gain variation that the NALM chain with 3×3 couplers can compensate for. System requirements will dictate a maximum allowable $\Delta P_i^{(\infty)}$, which in turn will impose the maximum allowed ΔG . For example, if the strongest and weakest channel are allowed to differ by up to 3 dB, the NALM chain in this example can compensate for ~ 4.5 dB of OA gain variation (see Fig. 3.4(b)).

3.2 Cascaded NALM simulations

The analysis in Sect. 3.1 demonstrates the fundamental principles of NALM-based gain equalization and gives the reader insight into the amount of OA gain variation that may be compensated, but it does not include the effects of OA gain saturation. Because the OA gain spectrum is a function of the total input power, the gain experienced by any single WDM channel will be coupled to the powers of all other channels. Therefore, determining $P_i^{(\infty)}$ requires knowing $P_j^{(\infty)}$ for all $j \neq i$. We shall now present analyses that include saturation by performing numerical simulations of OA gain within an iterative model of a NALM chain carrying multiple WDM channels.

3.2.1 EDFA saturation model

Our model incorporates erbium-doped fiber amplifiers (EDFAs) as the gain element in the NALMs. An in-house developed EDFA simulator is used to predict the gain spectrum for a given set of input signal powers, pump powers, and doped-fiber specifications. (REF POL-SIM) Since this software was not integrated within the program that simulates propagation of the signals through a chain of NALMs, it must be run in advance to generate look-up tables of the gain at each signal wavelength. These values are then used in the chain simulation.

Since the signals' powers will vary from link to link and we wish to run multiple chain simulations with different signal sets, the number of combinations of saturating signals to be run through the EDFA simulator quickly grows unwieldy. Instead, we incorporate a saturating-tone model that can accurately predict the gain spectrum using a limited number of saturating signals, as reported in [74].

The EDFA simulator is run with a single strong saturating tone at 1545 nm with power P_s and multiple weak signals ($P_i = 1$ nW) spaced at 1-nm intervals from 1525–1564 nm. The code outputs the gain of each channel G_i for saturating power P_s . This is repeated for saturating tones with power $0.1 < P_s < 400$ mW, and the results are tabulated. At any given λ_i , the gain is determined by interpolating between the gain values of the two closest values of P_s in the look-up table.

To simulate an EDFA in a WDM system with n channels, the saturating power should be determined using a weighted sum of the signal powers, weighted by the gain of each signal: [74]

$$P_s = \frac{1}{\lambda_s G_s} \sum_{i=1}^n P_n G_n \lambda_n. \quad (3.4)$$

Since we have no knowledge of the G_i 's at the outset, we first set $P_s = \sum_{i=1}^n P_i$ and look up the preliminary gains G_i' 's in the data table. We now use the G_i' 's with (3.4) to find a refined value of P_s , which can be used to find new gain values G_i'' 's. This process may be repeated iteratively

Table 3.2: Parameters used for NALM chain simulations.

NALM	Value	EDFA	Value
γ	$20 \text{ W}^{-1}\text{km}^{-1}$	λ_{pump}	1480 nm
ϕ_{bias}	$\pi/3$	λ_s	1545 nm
ℓ_{loop}	2.5 km	$P_{pump,1}$	200 mW
α_{loop}	-0.5 dB/km	$P_{pump,2}$	200 mW
ℓ_{eff}	2.17 km	ℓ_{EDF}	7.0 m
L_{span}	-18.75 dB	Er concentration	$6 \times 10^{24} \text{ ions/m}^3$
		Lifetime	$6 \times 10^{-3} \text{ s}$
		EDF A_{eff}	$9.08 \times 10^{-12} \text{ m}^2$

until both P_s and G_i remain constant. We have found that two iterations is typically enough to give a gain error $\delta G_i < 0.2$ dB (5%), which is sufficient for this demonstration.

When the EDFA is located within a NALM, the signals are entering from both ends of the EDFA. To simplify the EDFA model, we assume the gain is identical in both directions (which is a very good assumption under most circumstances) and the saturating tone's power is calculated by summing the total input power from each end. For the NALM shown in Fig. 3.1(b), the input power $P_i^{(0)}$ is divided into thirds, one of which directly enters the EDFA, one is unused, and the third enters the EDFA after propagating through a long fiber with loss $L_{loop} = \alpha_{loop}\ell_{loop}$. Therefore, the total EDFA input power is $P_{EDFA}^{in} = \left(\frac{1}{3} + \frac{L_{loop}}{3}\right) P_i^{(0)}$, where L_{loop} has linear units. It is this value that is used to determine the saturating-tone power for the EDFA simulation.

3.2.2 Chain simulations

To simulate a chain of NALMs with EDFA saturation, we first define the operating parameters for our example (see Table 3.2), all of which represent readily available technology. The highly nonlinear (HNL) fiber chosen for the NALM loop is similar to the dispersion-shifted fiber (DSF) ‘‘Fiber A’’ published in [61], which combines a large nonlinear coefficient with minimal attenuation of 0.5 dB/km. The specific EDF modeled is a custom fiber used in our laboratory and pumped from each end at $\lambda_{pump} = 1480$ nm with a combined pump power of 400 mW. This choice was dictated by the availability of fiber specifications for simulation; however, it could easily be replaced by one of many commercially available fibers. The calculated gain spectrum of this EDFA is shown in Fig. 3.5 at four different saturation levels.

Using the parameters in Table 3.2, the chain simulation simply calculates the power of a set of WDM channels transmitted through each link of the NALM chain using (3.1). At each link, the total NALM input power is used to determine the EDFA gain G_i using the methods

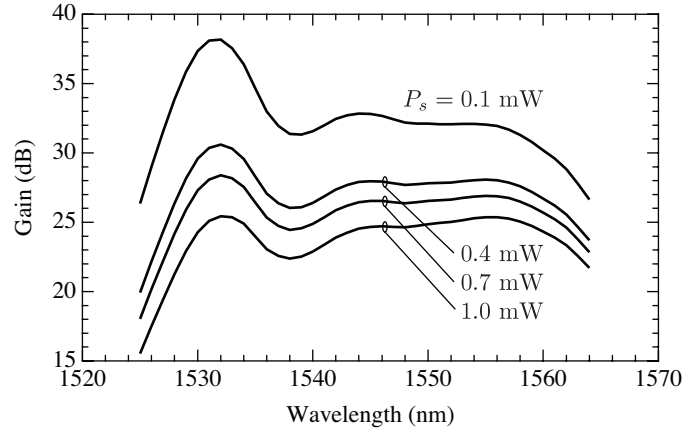


Figure 3.5: Modeled EDFA gain spectrum vs. saturation.

EDFA with parameters listed in Table 3.2. A strong signal at 1545 nm with power P_s is used to adjust saturation level of amplifier, while weak signals spaced every 1 nm between 1525–1564 nm probe the gain spectrum.

of Sect. 3.2.1. To keep the analysis similar to Sect. 3.1, a fiber span loss of 18.75 dB is chosen. When combined with the NALM fiber-loop loss of 1.25 dB, the total propagation loss becomes $L_{link} = -20$ dB. This is advantageous since it allows us to directly compare the channel gains with the limits derived in Sect. 3.1.

To demonstrate the gain-equalizing ability of the NALM chain, we simulate the transmission of ten WDM channels spaced evenly between 1532–1550 nm. This portion of the EDFA gain spectrum (see Fig. 3.5) represents the most non-uniform region of the C-band ($\sim 1530 \rightarrow 1560$ nm), hence the most adverse conditions to operate the NALM chain. The channels are launched with powers chosen randomly between 0.01 and 0.10 mW to simulate an actual transmission system in which the input powers of the various channels are not the same. The result (Fig. 3.6(a)) shows that after just one gain-loss link, all channel powers have converged to within ± 0.025 mW of the same value. After several links, the powers have stabilized near their steady-state values, which are maintained indefinitely. This simulation confirms the three key aspects of the system already demonstrated in the absence of gain saturation in Sect. 3.1: (1) the powers of channels with different input power converge after only a few links; (2) once the steady-state condition is reached, the effective gain of all channels are equal and the channels' powers do not diverge; and (3) the steady-state power levels are similar, but not equal.

We can inspect the performance more closely using the data presented in Fig. 3.6(b). The EDFA gain changes as the input power adjusts in the early links, but once the steady-state condition is reached the NALM chain is compensating for 4.2 dB of gain variation across the wavelengths launched. The output powers $P_i^{(20)}$ of the 20th link are a function of G_i , as in

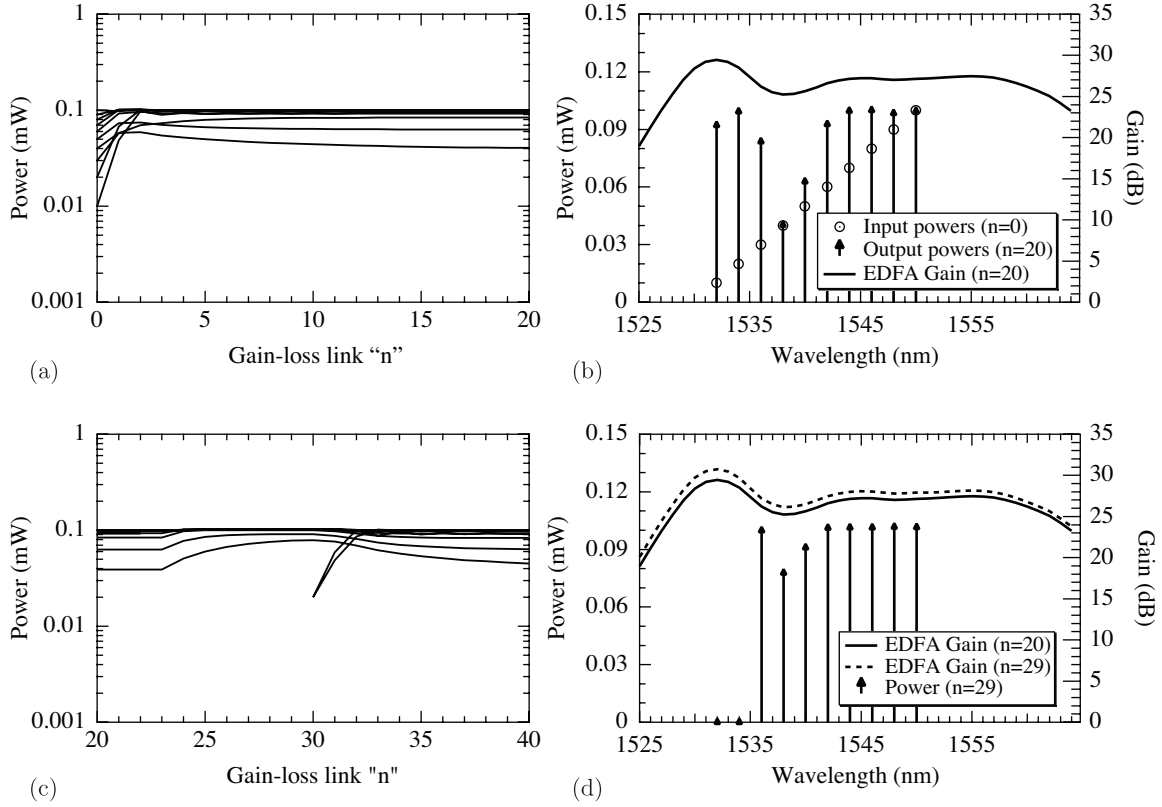


Figure 3.6: Evolution of ten WDM signals in NALM chain.

System parameters shown in Table 3.2. (a) Power evolution through 20 gain-loss links after launching with unequal levels. Signals converge to similar power levels during first few links and are maintained at these levels indefinitely. (b) Power and gain spectra at $n = 20^{\text{th}}$ link. NALM-based gain-equalization system is compensating for $\Delta G \approx 4.2$ dB. (c) Channels at wavelengths $\lambda = 1532$ nm and $\lambda = 1534$ nm are dropped at link $n = 23$ and reintroduced at link $n = 30$ to demonstrate the system's response to a system reconfiguration. (d) Power and gain spectra at $n = 29^{\text{th}}$ link.

Fig. 3.4. The behavior of the NOLM gain equalizer when channels are added or dropped is demonstrated in Fig. 3.6(c), in which we continue the simulation starting at link $n = 20$ from Fig. 3.6(a). At $n = 23$ we drop the channels at wavelengths $\lambda = 1532$ nm and $\lambda = 1534$ nm by setting their powers to zero. In the subsequent links, the EDFA gain increases (since there are fewer channels present), which causes the powers of the remaining channels to converge to new steady-state levels. The gain and spectrum at $n = 29$ is shown in Fig. 3.6(d). At the $n = 30^{\text{th}}$ link, the two channels are reintroduced with powers $P = 0.02$ mW. Within a few links, the system returns to its original power levels. Similar shifts in channel power would be expected if, for instance, a change in EDFA pump power occurred. This demonstration highlights the NOLM's robust response to system changes.

In Fig. 3.6, notice that the gain of all channels fell within the acceptable range 24.77–29.9 dB, with the weakest channel (1538 nm) having the least gain ($G \approx 25.2$ dB). To demonstrate the result of a channel's gain falling below the acceptable limit, we reconfigure the above example by moving two channels to $\lambda = 1526$ and 1564 nm. These wavelengths lie toward the edge of the EDFA gain spectrum and consequently they experience a lower gain. The evolution of the ten channels is shown in Fig. 3.7(a) and the gain and power spectra at $n = 20$ in Fig. 3.7(b). The gain at $\lambda = 1526$ and 1564 nm is 21.8 and 23.6 dB, respectively; both of them are below the minimum tolerable level, causing them to be attenuated with each gain-loss link. The gain from the available inverted Er^{3+} ions is now shared essentially by only eight channels, which increases the gain each channel experiences. This increase pushes the gain at $\lambda = 1532$ nm above $G = 29.9$ dB, causing the signal at this wavelength to exhibit oscillatory behavior (see Fig. 3.7). The oscillations are small, about $\pm 5\%$, and are likely not a problem. The upper gain limit, therefore, is *soft*. It does not define a condition where a signal is immediately unusable, but it does mark the point at which any increase in gain will cause added instability.

Since the gain magnitude is driven by the total EDFA input power, the system designer's job is to include enough channels such that the peak gain is $\lesssim 29.9$ dB (for the parameters used here). Additionally, he/she must assure that the weakest gain remains greater than 24.77 dB. Since this minimum gain level corresponds to $P_i^{(\infty)} = 0$, a higher minimum must be defined in terms of the minimum allowable channel power. Since $P_i^{(\infty)}$, G_i , L_{link} , and $\gamma\ell_{eff}$ are all coupled through the gain saturation, this must be done through numerical simulations like those shown in this section. The system tolerances become more lax when the OA gain spectrum is more uniform.

3.3 NOLM amplitude instability

The theory presented thus far in Chapter 3 has assumed input signals whose intensities don't vary in time. In practice, though, *all* signals will have a non-constant time dependence at some

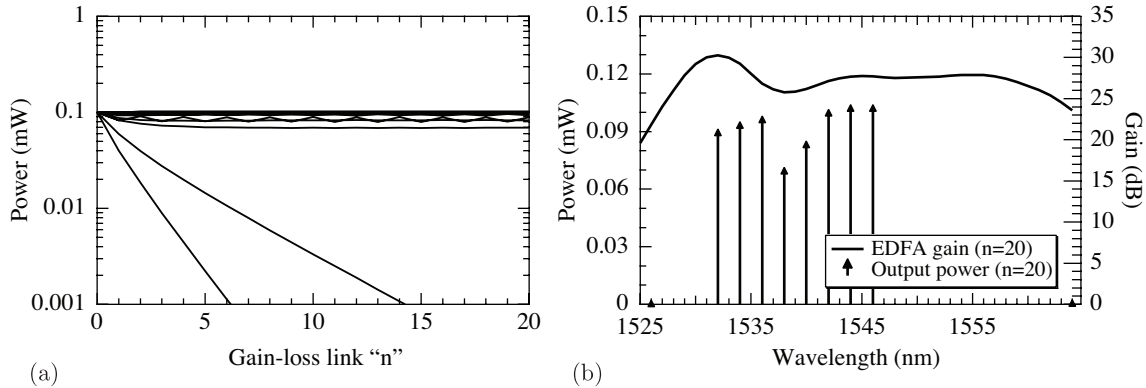


Figure 3.7: Evolution of WDM signals with too much gain variation.

System parameters shown in Table 3.2. (a) Power evolution through 20 gain-loss links after launching with equal levels. Signals at $\lambda = 1526$ and 1564 are attenuated with each link since their gains are below the minimum threshold. Signal at $\lambda = 1532$ nm shows oscillatory behavior when its gain rises above 29.9 dB. (b) Power and gain spectra at $n = 20^{\text{th}}$ link.

scale. Intensity fluctuations in a CI-modulated communication system are unwanted and may be the result of a number of phenomena. Intensity-noise sources include the shot noise of the optical source, in addition to processes dependent upon the modulation scheme. For instance, a phase-modulated signal's instantaneous frequency varies with $d\Phi/dt$. Due to fiber dispersion, the different frequencies present will travel at different speeds. Each phase-encoded bit will therefore acquire some amplitude modulation as the faster-moving photons overlap the slower photons in front. The result of this PM-AM conversion is intensity modulation centered at the fundamental frequency of the data-encoded signal [75, 76].

Dispersion management is required to mitigate the signal deterioration this effect causes [77–81], but the fact that intensity variations will always exist requires that we examine the performance of the NALM chain with their presence explicitly included. To include a time-dependent input power, the nonlinear Kerr phase shifts experienced in a NALM must be modified from the original expressions in (2.3). For a NALM with a 3×3 coupler:

$$\phi^{ccw}(t) = \gamma \frac{P(t)}{3} \ell_{eff} + 2\gamma G \frac{\langle P(t) \rangle}{3} \ell_{eff}, \quad (3.5a)$$

$$\phi^{cw}(t) = \gamma G \frac{P(t)}{3} \ell_{eff} + 2\gamma \frac{\langle P(t) \rangle}{3} \ell_{eff}, \quad (3.5b)$$

where $\langle P(t) \rangle$ represents the signal power time-averaged across $t \pm \tau_{loop}$, where τ_{loop} is the Sagnac loop's transit time. As a photon propagates through the NALM loop, it interacts through counter-propagating XPM with all the photons that both lead and lag behind it within $t = \pm \tau_{loop}$.

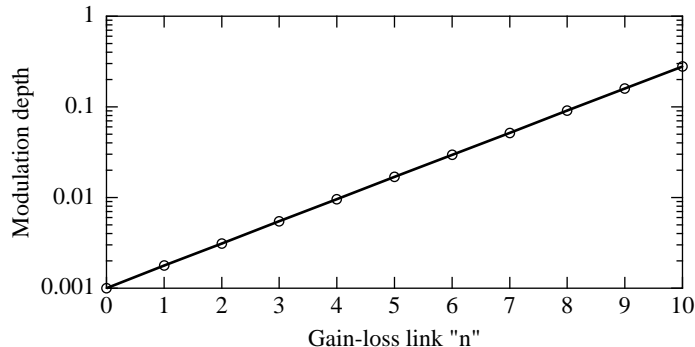


Figure 3.8: Growth of initially small amplitude modulation in NALM chain.

The NALM attenuation’s dependence on instantaneous power causes amplitude noise to grow with each amplification. Simulation is of signal at $\lambda = 1550$ nm from Fig. 3.6 in its steady-state condition when launched with 0.1% modulation depth.

Therefore, all counter-propagating XPM phase shifts scale with the average power. On the other hand, the SPM phase shifts are proportional to the instantaneous power $P(t)$. The resulting nonlinear phase difference is now

$$\Delta\phi^{nl}(t) = \frac{\gamma}{3}[2\langle P(t) \rangle - P(t)](G - 1)\ell_{eff}. \quad (3.6)$$

Let’s now consider the implications of (3.6) on a signal with a small amplitude modulation: $P(t) = P_0[1 + a_m \cos(2\pi f_m t)]$, where the modulation depth a_m is much smaller than 1. Recall that a positive $\Delta\phi^{nl}$ will cause the NALM to reduce the output power of a signal. For a CI signal, $\Delta\phi^{nl}$ is proportional to the power, therefore signals with more power receive more attenuation—the central concept of the gain-equalization system. In contrast, Eq. (3.6) states that portions of the modulated signal with larger instantaneous power ($P(t) > \langle P \rangle$) have a decreased $\Delta\phi^{nl}(t)$ compared to the lower power portions. If the signal’s “peaks” are attenuated less than the “valleys”, then the signal will exit the NALM with a larger modulation depth than it entered.

With each gain-loss link, the signal’s modulation depth will grow ever faster because the gain difference between peaks and valleys enlarges. This allows initially small modulations to quickly become a problem. If we define the modulation depth $\delta_m = (P_{max} - P_{min})/(2\langle P \rangle)$, we can simulate the change in δ_m as a signal propagates through a NALM chain. We arbitrarily choose the signal at $\lambda = 1550$ nm as modeled in Fig. 3.6. In its steady-state condition ($G = 27.16$ dB, $P = 0.1$ mW), the evolution of δ_m is shown in Fig. 3.8 for an initial $\delta_m = 0.1\%$. The modulation depth grows exponentially with each amplification, increasing by approximately one order of magnitude after every four gain-loss links.

It is obviously of critical importance to address this nonlinear amplitude instability issue.

Ideally, the NALM switching should respond only to the average power of a WDM channel. If this were the case, the NALM would not have the ability to affect amplitude modulation in any way. This is precisely the behavior we achieve with the *folded* NALM, presented in the following chapter.

Chapter 4

NOLM with folded nonlinear loop

As discussed in Sect. 3.3, the NOLM chain presented suffers from a nonlinear amplitude instability due to the dependence of self- and cross-phase modulation upon instantaneous and average power, respectively. This is inherently linked to the fact that the two signals in the Sagnac interferometer are traveling in opposite directions.

In this chapter, we discuss an alternative configuration in which the Sagnac loop is “folded”, so that the two signals *co*-propagate through the long optical fiber where nonlinear phase shifts are accrued. In Sect. 4.2, we show that folding the nonlinear loop improves the amplitude stability of the NOLM chain. But first, we present the folded NOLM and the application for which it was initially conceived—acoustic desensitization.

4.1 Folded loop and acoustic desensitization

4.1.1 Acoustic pickup in Sagnac interferometers

In free-space interferometry, the optical beams travel through air or vacuum and experience relatively minor phase perturbations before interfering at the output coupler. There are two key differences with fiber interferometers, though. First, the guided optical mode and low attenuation of single-mode fibers allow interferometers to easily be built with multi-km-long optical paths. Second, the optical path resides within a solid fiber in which significant phase perturbations are possible as a result of temperature changes, mechanical forces, and fiber motion.

The primary benefit of fiber Sagnac interferometers over other types, such as Mach-Zehnder interferometers, is their resistance to the fringe drift normally associated with these types of perturbations. Because it is a common-path interferometer, slowly varying perturbations (those that change on a time-scale much longer than the loop transit time) affect both signals equally since they travel in the same fiber. For this reason, the output of a Sagnac interferometer

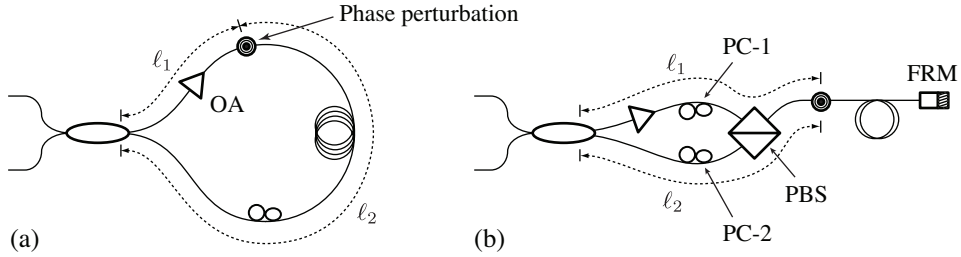


Figure 4.1: Effect of phase perturbations on folded Sagnac interferometer.

(a) In a conventional NALM, a time-varying phase perturbation will affect counter-propagating beams differently, thus inducing amplitude noise at the output. (b) In a folded NALM, the two beams *co-propagate* in the long coil and a phase perturbation causes no phase difference between them. A polarizing beam splitter (PBS) and Faraday-rotator mirror (FRM) direct the two beams down appropriate fiber arms after double-passing the long fiber coil.

doesn't drift with slow temperature changes. However, when the perturbation varies on time-scales similar to and shorter than the transit time, they can begin to generate a phase difference between interfering signals. For example, consider the NALM in Fig. 4.1(a) that is subjected to a phase perturbation located at a distance ℓ_1 and ℓ_2 from the coupler in the clockwise and counter-clockwise directions, respectively. For a phase perturbation $\phi_p \cos(2\pi f_p t)$, the phase difference of the two interfering signals is

$$\Delta\phi(t) = 2\phi_p \sin\left(\frac{2\pi f_p \Delta T}{2}\right) \sin\left(2\pi f_p \left(t + \frac{\Delta T}{2}\right)\right), \quad (4.1)$$

where ΔT is the propagation time through a length of fiber equal to $\ell_1 - \ell_2$, i.e., the difference between the times two simultaneously incident photons reach the perturbation after traveling in opposite directions around the loop [82].

From (4.1), it is evident that the phase responsivity of a Sagnac interferometer is zero when the perturbation occurs at the loop center ($\Delta T = 0$). This is because any perturbation at this location imparts the same phase shift on both signals, even when this perturbation varies in time. Elsewhere in the loop, time-varying phase shifts will induce a phase difference that will cause amplitude noise at the interferometer output. This makes fiber Sagnac interferometers with long fiber loops susceptible to pickup of amplitude noise at acoustic frequencies due to the vibration of the host fiber.

To minimize acoustic pickup, we use a folded-loop configuration in which the two interfering beams *co-propagate* in the long nonlinear fiber coil (see Fig. 4.1(b)). This is achieved by adjusting the SOPs of the two beams with polarization controllers PC-1 and PC-2 such that they exit the same port of a polarizing beam splitter (PBS), but in orthogonal states. The two signals now

co-propagate along the long fiber coil until they reach a Faraday-rotator mirror (FRM). Because the FRM reflects an input signal into its orthogonal state, any polarization rotation that occurred in the first pass of the fiber coil is exactly undone in the second pass. Thus, the signals reach the PBS the second time in SOPs orthogonal to those with which they first passed, no matter the birefringence of the fiber coil [83]. Each signal is then routed by the PBS into the opposite arm from which it entered. Since both the cw and ccw beams traverse both arms and the fiber coil twice (once in each of two orthogonal states), the common-path nature of the Sagnac interferometer is maintained.¹

The majority of the fiber that makes up the Sagnac interferometer is located in the folded section of the interferometer, since the two arms between the Sagnac coupler and PBS may be as short as possible while still including the polarization controllers and OA. In the folded section, the phase difference between interfering signals is still given by (4.1), but now ΔT is the difference in transit time of the two arms. By choosing $\ell_1 = \ell_2$, the sensitivity to phase perturbations occurring in the fiber coil becomes zero. Of course, there are limits to how closely matched the arm lengths can be in practice; these constraints will be addressed in Sect. 4.2.2.

The dramatic reduction in acoustic pickup in folded loops has been studied thoroughly with fiber-Sagnac sensor arrays by Vakoc, et al. [82,84]. Additionally, similar configurations have been used in NOLMs that are operated with pulsed signals in Refs. [6,8]. Our use of the folded loop mirror with CI signals modifies the nonlinear effects experienced by the two signals in subtle but significant ways, as presented in Chapter 6, but this configuration still acts to automatically balance the powers of the WDM channels. The primary benefit of using a folded loop in the NOLM-based gain equalizer is its beneficial effect upon the nonlinear amplitude stability, which will be discussed in Sect. 4.2. Additionally, the effective nonlinear interaction length of the NOLM is nearly doubled in the folded configuration since the beams pass twice through the same fiber, thus reducing both the size and cost of the device.² Readers who wish to learn more about the reduction of acoustic pickup are directed to Refs. [6,8,82,84].

4.1.2 Bias phase in folded NOLM

With the exception of the fact that the optical path is twice as long for a given physical fiber length, a folded Sagnac interferometers operates similarly to a conventional one. One significant difference, though, is the effect of the folded configuration on the bias phase ϕ_{bias} . The cw and ccw signals are co-polarized in Arms 1 and 2 and therefore accumulate the same phase through these two arms. Each signal also reflects once and passes once through the PBS, so no difference in phase is generated. The only portion left to explore is the folded loop and FRM.

¹With a *folded* loop mirror, the designations “cw” and “ccw” refer to the direction of the interfering signals while they propagate in the unfolded portion of the interferometer between the input coupler and PBS.

²The effective interaction length would be *exactly* doubled if the fiber and FRM were lossless, which is impossible.

Using an analysis similar to [83], we can determine the phase difference experienced by the two beams after transmission through the folded loop. To simplify the analysis, unlike in [83], we choose a reference frame with fixed axes for both propagation directions to simplify the analysis. The Jones matrix for the Faraday rotator is a composite of two rotations and a mirror reflection:³

$$[\text{FRM}] = \begin{bmatrix} \sqrt{2}/2 & -\sqrt{2}/2 \\ \sqrt{2}/2 & \sqrt{2}/2 \end{bmatrix} \begin{bmatrix} 1 & 0 \\ 0 & 1 \end{bmatrix} \begin{bmatrix} \sqrt{2}/2 & -\sqrt{2}/2 \\ \sqrt{2}/2 & \sqrt{2}/2 \end{bmatrix} = \begin{bmatrix} 0 & -1 \\ 1 & 0 \end{bmatrix} \quad (4.2)$$

In [83], it has been shown that any arbitrary phase retardation may precede an FRM and the above result is unchanged. This simply implies that each signal exiting a folded loop is polarized orthogonally to the polarization it had when it entered the loop, regardless of fiber birefringence.

In the folded NALM, the two interfering signals enter the folded loop in orthogonal linear polarizations. Without loss of generality, we choose the cw and ccw signals to be x - and y -polarized, respectively. Upon returning to the PBS, the cw and ccw signals have been transformed into

$$[\text{FRM}] \begin{bmatrix} 1 \\ 0 \end{bmatrix} = \begin{bmatrix} 0 \\ 1 \end{bmatrix} \quad (4.3)$$

and

$$[\text{FRM}] \begin{bmatrix} 0 \\ 1 \end{bmatrix} = \begin{bmatrix} -1 \\ 0 \end{bmatrix}, \quad (4.4)$$

respectively. The orthogonal signals have swapped polarizations, but they also underwent a sign change. In fact, it can be shown that any pair of elliptically polarized, orthogonal signals will acquire a π phase difference upon reflecting from an FRM.

This π phase shift must be included in ϕ_{bias} . As was mentioned in Chapter 3, the effect of this additional phase shift on a NALM with a 3×3 coupler is to shift the three ports' biases to 0 and $\pm\pi/3$. If a 2×2 coupler is used, the two output ports simply swap roles.

4.1.3 Nonlinear phase difference

Folding the NALM fiber coil complicates the analysis of the nonlinear phase shifts in several ways. The cw and ccw signals now co-propagate in the long fiber loop after entering in orthogonal, linear SOPs along \hat{x} and \hat{y} , respectively. Since the fiber coil is non-PM, the polarization states are not maintained during propagation. At a position z in the fiber loop, the initially \hat{x} - and \hat{y} -polarized beams have SOPs aligned along new axes $\hat{u}(z)$ and $\hat{v}(z)$, respectively (see Fig. 4.2). These axes define the SOPs of the cw and ccw beam throughout the folded loop with $\hat{u}(0) = \hat{x}$ and $\hat{v}(0) = \hat{y}$, where $z = 0$ is the beginning of the folded portion at the output of the PBS. The \hat{u} - \hat{v} basis is randomly evolving along the fiber length and the orthogonality condition $\hat{u}(z) \cdot \hat{v}^*(z) = 0$ is

³For a review of Jones calculus see [85], or any of a number of introductory optics texts.

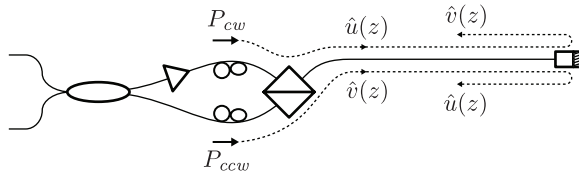


Figure 4.2: Polarization states in folded NALM.

In a folded loop with non-PM fiber, the cw and ccw beams exit the PBS in orthogonal, linearly polarized states. The SOPs rotate during propagation in the non-PM fiber and the FRM reflects them into their orthogonal states. Throughout the folded loop, the cw and ccw beams remain orthogonal, though the local SOP at any point in the fiber [other than at the PBS] will be an unknown elliptical SOP $\hat{u}(z)$ or $\hat{v}(z)$.

Table 4.1: Nonlinear coefficients for linear and randomly varying SOPs.

	SPM	XPM $_{\perp}$	XPM $_{\parallel}^{\rightleftharpoons}$	XPM $_{\perp}^{\rightleftharpoons}$
linear	γ	$\frac{2}{3}\gamma$	2γ	$\frac{2}{3}\gamma$
random	$\frac{8}{9}\gamma$	$\frac{8}{9}\gamma$	$\frac{16}{9}\gamma$	$\frac{8}{9}\gamma$

maintained for all z . Therefore, the cw and ccw beams interact via orthogonal, co-propagating XPM. It is widely understood that the SPM effect in a long non-PM fiber has a nonlinearity of $\frac{8}{9}\gamma$, where γ is the fiber nonlinearity for linear SOPs. It turns out that the nonlinear coefficient for XPM between orthogonal, co-propagating signals with identical wavelengths is identically $\frac{8}{9}\gamma$ [64–66].

Additionally, the signals are counter-propagating with the two beams that have reflected off the FRM. The co-polarized and orthogonal, counter-propagating XPM from these two beams must be considered. In a randomly birefringent fiber, co-polarized XPM has nonlinearity $\frac{16}{9}\gamma$, just as presented for the non-folded NALM [67]. The interaction between counter-propagating fields has been detailed by Clausen, et al., in Ref. [86]. For the specific case when the fields' polarizations remain orthogonal, it has been shown that the nonlinearity is $\frac{8}{9}\gamma$.⁴ The nonlinear coefficients for these various cases in a randomly birefringent (non-PM) fiber are summarized in Table 4.1 along with the values for linearly polarized signals (PM fiber) for comparison.

Noting that upon reflection, the \hat{u} - and \hat{v} -polarized signals swap SOPs, we can now write the

⁴The usual orthogonality condition $\hat{u}^+ \cdot \hat{u}^{-*} = 0$ is not well-defined for counter-propagating waves. Therefore, fields are defined as “orthogonal” if their Stokes vectors are anti-parallel on the Poincaré sphere. This is addressed in Chapter 6.

nonlinear phase shifts of the forward-propagating cw and ccw signals

$$\phi_+^{ccw}(t) = \frac{8}{9}\gamma P_+^{ccw} \ell_{eff} + \frac{8}{9}\gamma P_+^{cw} \ell_{eff} + \frac{16}{9}\gamma P_-^{cw} \ell_{eff} + \frac{8}{9}\gamma P_-^{ccw} \ell_{eff}, \quad (4.5a)$$

$$\phi_+^{cw}(t) = \frac{8}{9}\gamma P_+^{cw} \ell_{eff} + \frac{8}{9}\gamma P_+^{ccw} \ell_{eff} + \frac{16}{9}\gamma P_-^{ccw} \ell_{eff} + \frac{8}{9}\gamma P_-^{cw} \ell_{eff}, \quad (4.5b)$$

where the \pm superscripts denote propagation direction and are present solely to help identify which signals are responsible for each term. From the inherent symmetry of the system, the phase shifts acquired after reflecting off the FRM are identical. We may therefore conclude that the nonlinear phase difference after the folded loop is

$$\Delta\phi^{nl} = \frac{8}{9}\gamma(P^{cw} - P^{ccw})\ell'_{eff}, \quad (4.6)$$

where ℓ'_{eff} is the effective nonlinear length of the entire folded loop, i.e., calculated using a length that is twice as long as the actual fiber coil because it is double-passed. Other than the increase in nonlinear interaction length, the result is identical to $\Delta\phi^{nl}$ for the unfolded NALM in (2.4) and (2.5).

4.1.4 Measurement of nonlinear phase difference

In this section we present experimental verification of the nonlinear phase difference in a folded NOLM (4.6). The experiment schematic is shown in Fig. 4.3. A 1559-nm distributed-feedback laser diode (DFB) was amplified by an EDFA, resulting in a power of ~ 100 mW entering the 3×3 coupler. The signal had no data encoded upon it and therefore had a narrow linewidth. To suppress the stimulated Brillouin scattering (SBS) that accompanies the transmission of narrow-linewidth signals through long lengths of fiber, the current supplied to the DFB had a 1% modulation at 25 kHz. This low-frequency current dither served to frequency modulate the laser output with an amplitude larger than the SBS bandwidth linewidth (typically < 100 MHz in SMF) [87, 88].

To provide experimental flexibility, variable optical attenuators (VOAs) were used in the two arms of the NOLM to generate a power difference in the folded loop. Their presence allowed us to easily adjust the power imbalance—and thus the nonlinear phase shift—while maintaining a constant input power. If instead the EDFA had been placed in one of the arms to make a NALM, adjusting the amount of power imbalance would require changing the EDFA pump power. This would cause changes in the amplified spontaneous emission (ASE) spectrum in addition to changes in output SOP, which would require adjusting the PCs between measurements. With VOAs in the arms, (4.6) becomes

$$\Delta\phi^{nl} = \frac{8}{9}\gamma \frac{P_{in}}{3}(L_1 - L_2)\ell'_{eff}, \quad (4.7)$$

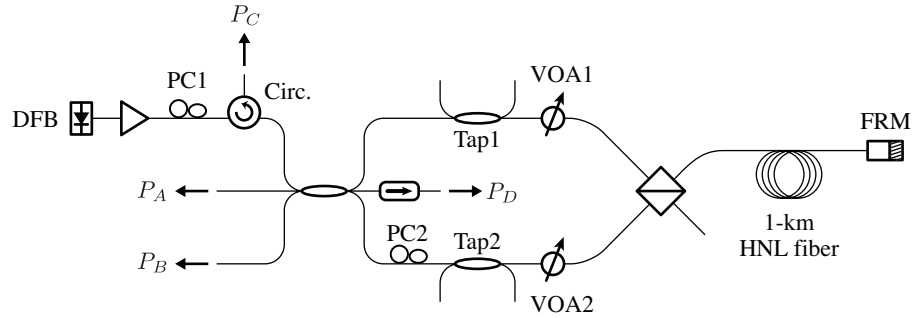


Figure 4.3: Schematic of experiment measuring folded-NOLM phase shifts.

Output power is measured at P_A , P_B , and P_C as a function of power asymmetry ($L_1 - L_2$) by adjusting VOA losses. Input power is measured at P_D , where an optical isolator is used to prevent back-reflections from the cleaved fiber end from reaching output ports. One-percent tap couplers provide locations to monitor power. Results shown in Fig. 4.4.

where P_{in} is the power entering the Sagnac coupler and $L_m = L_m^{il} \times L_m^{VOA}$ is the total transmissivity of arm m including insertion loss of all components (L^{il}) in addition to the adjustable loss of the VOA (L_m^{VOA}). We will often refer to losses in decibels, though the reader should note that when used in (4.7), L_m must have linear units, i.e. $L = 1$ represents complete transparency and $L = 0$ total opacity. One percent tap couplers (Tap1 and Tap2) were used to monitor the power circulating in each direction and aid in adjusting the VOAs.

Two polarization controllers adjusted the input SOP such that the signal from each arm fully entered the folded loop. First, VOA2 was set to maximum attenuation ($L_2^{VOA} = 0$) and PC1 was adjusted such that a minimum power was achieved at the fourth, unused PBS port. The VOA settings were then reversed ($L_1^{VOA} = 0$, $L_2^{VOA} = 1$) and PC2 was used to adjust the birefringence of arm 2 by minimizing the power at the fourth PBS port. Once the PCs were set, they did not need adjustment during the measurements.

The folded loop was made of a 1-km highly nonlinear dispersion-shifted fiber (HNL-DSF) supplied by Sumitomo Electric Industries, LTD. Its specified zero-dispersion wavelength was $\lambda_0 = 1556$ nm and its nonlinearity $\gamma \approx 10$ (W·km) $^{-1}$. This is approximately ten times more nonlinearity than Corning SMF-28 fiber. Fiber attenuation was 0.43 dB/km, resulting in $\ell'_{eff} = 1.78$ km.

The NOLM output power was measured at three locations (P_A , P_B , and P_C), which represent the three output ports with $\phi_{bias} = \frac{\pi}{3}$, $-\frac{\pi}{3}$, and π , respectively. The insertion loss of the circulator and the isolators used on ports A and B to prevent reflections (not shown in the schematic) were accounted for, thus reported power levels represent the power in each port immediately after exiting the coupler.

The NOLM asymmetry parameter ($L_1 - L_2$) was modified by adjusting the VOA attenuations

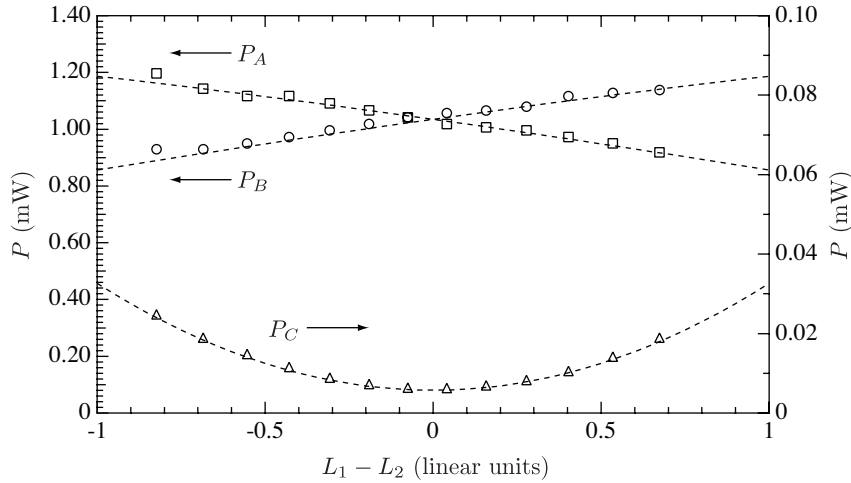


Figure 4.4: NOLM power output vs. loss asymmetry.

P_A , P_B , and P_C represent output ports with $\phi_{bias} = \frac{\pi}{3}$, $-\frac{\pi}{3}$, and π , respectively. Note change in scale for P_C . $L_1 \times L_2 = 0.25$ (-6 dB) for all measurements. Data fit (dashed lines) give fiber nonlinearity $\gamma = 9.5$ ($\text{W}\cdot\text{km})^{-1}$.

while keeping the total NOLM loss $L_1 L_2$ constant. Since $\Delta\phi^{nl}$ is proportional to $(L_1 - L_2)$ in (4.7), this variable was used to effectively scale the nonlinearity of the system. The results are shown in Fig. 4.4. In all measurements, the round-trip loss was made constant by keeping $L_1^{VOA} \times L_2^{VOA} = 0.25$ (-6 dB). When $L_1 - L_2 = 0$ (both VOAs at -3 dB) there is no power imbalance in the folded loop. Ports A and B then have nearly identical output powers while port C is nearly completely dark (note the different scale used for P_C). As $L_1 - L_2$ is changed, the measured output powers follow the raised cosine dependence predicted by (2.5). This result clearly indicates that the nonlinear response of a folded NOLM is the same as the traditional non-folded variety, but with an increased effective nonlinear interaction length.

The three output powers are fit (dashed lines) with $\gamma = 9.5$ ($\text{W}\cdot\text{km})^{-1}$. This is very close to the expected value; the slightly reduced fitted value is likely due to the insertion loss of the FRM. There is also some uncertainty in the actual nonlinearity specified by the manufacturer. The output power at the π -biased port C *should* be zero at the minimum ($L_1 - L_2 = 0$). Clearly, the observed output deviates from this behavior by several μW . This small deviation is likely due to a combination of three sources, each of which result in light returning from the folded loop to the Sagnac coupler through the wrong arm:

1. The finite extinction ratio of the PBS,
2. The SOP rotation induced by the FRM is not precisely 90° , and

3. ASE and signals at wavelengths that deviate from the operating wavelength of the FRM (~ 1550 nm).

These effects will be revisited in Chapter 7 as they relate to the noise performance of the NALM chain. The random phase and SOP of this misrouted light will cause it to be split evenly between the three output ports when averaged over time, i.e., when monitored with a slow power meter. This light is not observed at ports A and B since it is a small fraction of the total output at these ports. To better match the data, the P_C fit was elevated by $5.8 \mu\text{W}$.

The very close fit seen in Fig. 4.4 implies that our analysis of the nonlinear phase difference in a folded NOLM (Eqs. 4.5 and 4.6) is correct. It must be noted that no effort was made to equalize the arm lengths ℓ_1 and ℓ_2 . In subsequent measurements, the mismatch $\ell_1 - \ell_2$ was determined to be approximately 50 cm. As will be discussed in Sect. 4.2.1, this is small enough to prevent unwanted acoustic pickup, but large enough to affect the amplitude stability of the NOLM.

4.2 Amplitude stability in folded NOLMs

A fortuitous result of folding the fiber loop for acoustic desensitization purposes in a NOLM is its effect upon amplitude stability. As presented in Sect. 3.3, the conventional NOLM suffers from a nonlinear amplitude instability that causes intensity modulations to be magnified with each passage through a NOLM. The negative impact upon a gain-equalizing NOLM chain is obvious.

The terms in the Kerr phase shifts (4.5) originate from SPM, XPM_\perp , $\text{XPM}_\parallel^{\leftarrow}$, and $\text{XPM}_\perp^{\leftarrow}$, from left to right. Because of the identical magnitude of the SPM and XPM_\perp terms, $\Delta\phi_+^{nl}$ has no dependence upon the forward-propagating power P_+ . The interaction with P_- is averaged across the entire fiber length, therefore $\Delta\phi^{nl}$ in (4.6) is a function only of the average power $\langle P \rangle$. This above analysis assumes that the cw and ccw signal co-propagate in the folded loop with no time delay imparted between them from the two arms leading to the PBS. In this case, the folded NOLM's effects scale only with average power; therefore, intensity modulations are unaffected by the nonlinear action of the loop mirror. When the arms have different lengths, this assumption breaks down, and the validity of this conclusion must be re-assessed. In this section, we consider the NOLM's response to instantaneous power fluctuations in this more practical case when the arm lengths are unequal.

4.2.1 Arm-length mismatch

When the cw and ccw beams traverse unequal distances ℓ_1 and ℓ_2 , respectively, in the two fiber arms leading to the PBS, a net time delay τ will exist between them in the folded loop. When a time dependent input power $P_{in}(t)$ enters the NOLM, the co-propagating Kerr phase shift terms

in (4.5) are modified through the introduction of this time delay:

$$\phi_+^{ccw}(t) = \frac{8}{9}\gamma P_+^{ccw}(t)\ell'_{eff} + \frac{8}{9}\gamma P_+^{cw}(t+\tau)\ell'_{eff} + \frac{16}{9}\gamma \langle P_-^{cw} \rangle \ell'_{eff} + \frac{8}{9}\gamma \langle P_-^{ccw} \rangle \ell'_{eff}, \quad (4.8a)$$

$$\phi_+^{cw}(t) = \frac{8}{9}\gamma P_+^{cw}(t)\ell'_{eff} + \frac{8}{9}\gamma P_+^{ccw}(t-\tau)\ell'_{eff} + \frac{16}{9}\gamma \langle P_-^{ccw} \rangle \ell'_{eff} + \frac{8}{9}\gamma \langle P_-^{cw} \rangle \ell'_{eff}, \quad (4.8b)$$

where we have explicitly set the counter-propagating phase shifts to be proportional to the average power. An arm-length difference changes the spatial overlap of the signals in the folded loop, thus the XPM_{\perp} terms are the only ones affected. By rearranging the terms in (4.8) the nonlinear phase difference can be written as

$$\Delta\phi^{nl}(t) = \frac{8}{9}\gamma\ell'_{eff} \left\{ [P_+^{ccw}(t) - P_+^{cw}(t)] + P_+^{cw}(t+\tau) - P_+^{ccw}(t-\tau) + [\langle P^{cw} \rangle - \langle P^{ccw} \rangle] \right\}, \quad (4.9)$$

which is equivalent to (4.6) in the limit $\tau \rightarrow 0$, as expected. When τ is non-zero, the resulting time-dependent nonlinear phase difference will cause time-dependant switching at the Sagnac output, which results in an output signal with a temporal profile that differs from the input. Thus, as in the situation with the non-folded NOLM in Sect. 3.3, nonlinear amplitude instability may arise when the folded NOLM has an arm-length mismatch.

Let's assume an input signal has a small amplitude modulation $a_m \ll 1$ at frequency f_m , i.e., $P(t) = P_0[1 + a_m \cos(2\pi f_m t)]$. We would like to simulate the NOLM-induced change in the waveform resulting from an arm-length mismatch. Due to the nonlinearity of the NOLM transfer function and $\Delta\phi^{nl}(t)$, the sinusoidally modulated input signal will exit as a periodic, but non-sinusoidal output. The waveform evolution is most easily analyzed by ignoring its shape and instead focusing on just the changes in modulation depth, defined as $\delta_m = (P_{max} - P_{min})/(2\langle P \rangle)$. The sinusoidal input signal has modulation depth $\delta_m = a_m$. An increase of δ_m after transmission through a NOLM represents an increase in the difference between the waveform's maximum and minimum powers.

Using the same simulation parameters as in Fig. 3.8 and Table 3.2, we can calculate the change in δ_m with frequency for a single NALM with either a folded or non-folded loop. To keep the simulations comparable, the same value is used for ℓ_{eff} and ℓ'_{eff} for the non-folded and folded NALMs, respectively; the folded NALM would therefore only require a fiber coil of approximately half the physical length of the non-folded. The results are shown in Fig. 4.5. The AM response (dashed line) is frequency independent when a conventional non-folded loop is used, as expected. When folded, however, the NOLM has a strong periodic frequency dependence, with zero AM response when $f_m = n/\tau$ ($n = 0, 1, 2, \dots$). At these frequencies, the time-dependent terms in (4.9) cancel out because the cw and ccw waveforms perfectly overlap each other.

Although the folded NOLM magnifies input AM more than the non-folded at some frequencies,

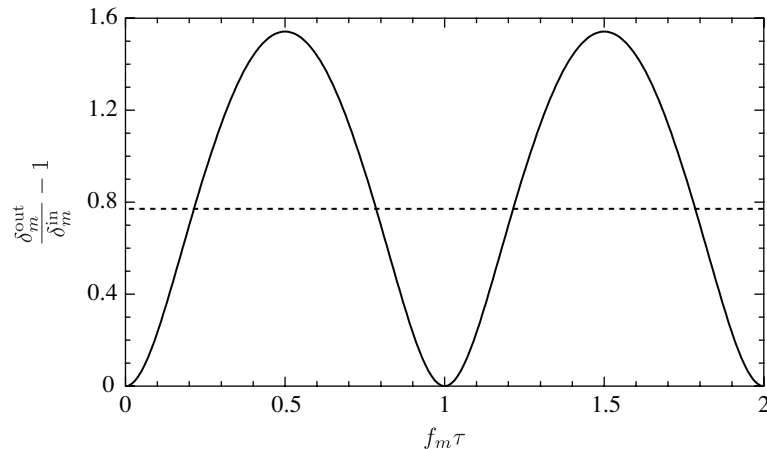


Figure 4.5: AM response of folded NALM

Simulation of change in modulation depth δ_m vs. frequency for folded NOLM with same parameters as used in Fig. 3.8. Zero AM response occurs at multiples of $1/\tau$, where $\tau = \frac{n}{c} |\ell_1 - \ell_2|$ is the time delay caused by an arm-length difference. The constant AM response of an unfolded NOLM is shown for reference (dashed line).

the important conclusion to draw from Fig. 4.5 is that very small response near DC may be extended to high frequencies by reducing τ . The receiver in a communication system needs to have a bandwidth approximately equal to the bit rate R_b . If $\tau \ll 1/R_b$, the first peak in Fig. 4.5 will be extended to $f \gg R_b$. The NOLM can therefore be designed to have a minimal effect on intensity noise in the detected frequency range by reducing τ toward 0. The limitations of this design criterion are discussed in Sect. 4.2.2.

It should be noted that the reduced AM response at frequencies $f_m = n/\tau$ when $n > 0$ only exist for the case of a repeating signal. When $n \geq 1$, the cw waveform overlaps in the folded loop with a section of the ccw waveform that is n periods ahead of it in time. For sinusoidal [or other regularly repeating] waveforms, the two waveforms then have identical overlapping shapes, causing the cancellation of the time-dependent terms in (4.9). But when the amplitude modulation is caused by PM-AM conversion, the AM waveform will be correlated to the data encoded on the signal, which is typically a random sequence of bits at $f_m = R_b$. Therefore, time-shifting the cw and ccw signals by one or more periods and then overlapping them results in non-identical waveforms, and in a $\Delta\phi^{nl}(t)$ that varies from bit to bit and no longer scales only with average power. For this reason, we expect that the zero AM responsivity occurring at $n = 1, 2, 3, \dots$ will not exist when the input signal's modulation is generated by an actual data stream. This is only important in an academic sense, since reducing τ to 0 will push these effects to frequencies far outside the detector bandwidth anyway, even for a random sequence of AM

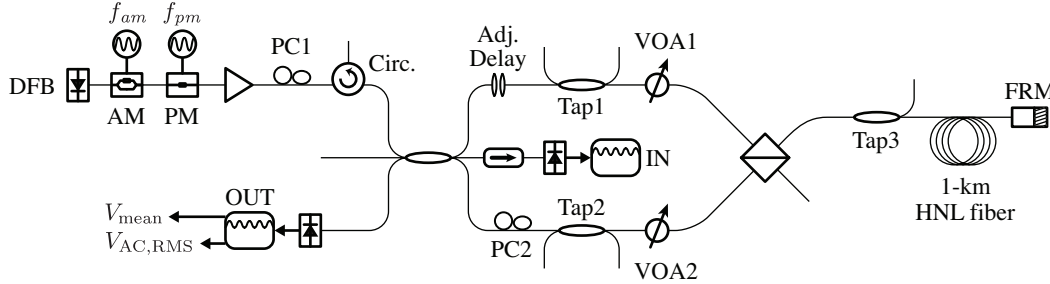


Figure 4.6: Schematic of experiment measuring nonlinear AM responsivity of NOLM

DFB laser source with external amplitude modulator (AM) is phase modulated at $f_{pm} = 125$ MHz for SBS suppression. VOAs generate power difference in folded loop. 1-GHz photodiodes and oscilloscope measure input and output amplitude modulations. Results shown in Fig. 4.7.

pulses. The important conclusion of this analysis is that our proposed folded-loop NOLM can operate with near-zero impact on the signals' intensity modulation even for random pulses; i.e., $\Delta\phi^{nl}$ will be independent of time and only a function of the average signal power, provided the time delay τ , or equivalently the length difference $\ell_1 - \ell_2$, is made small enough. The question of how small is "small enough" will be discussed in Sect. 4.2.2.

The AM response of the folded NOLM has been explored experimentally using the experiment setup shown in Fig. 4.6. Most components are the same as shown in Fig. 4.3, with some additions. The 1559-nm DFB source is externally modulated with a LiNbO₃ amplitude modulator at frequency f_{am} between zero and 300 MHz in order to measure the AM response of the folded NOLM over this frequency range. The signal is then phase modulated at $f_{pm} = 125$ MHz in order to broaden the linewidth to suppress SBS. Following EDFA amplification, the input signal is monitored at the third right-hand port of the 3×3 coupler with a 1-GHz photodiode and oscilloscope. The NOLM output is monitored with the same electronics as the input. The mean and AC-RMS voltages of both input and output waveforms are recorded for various values of f_{am} . These voltages are used to compare the difference between input and output modulation depths.

The upper arm of the folded NOLM (arm 1) contains a pair of microlenses on translational stages that can be used for fine-tuning the arm length. This adjustable delay may be tuned several centimeters with little insertion loss. For this experiment, balanced arm lengths were not required and this delay was not tuned. The arm-length difference was measured by launching rectangular pulses and measuring the timing difference between the two arms at the PBS output, resulting in $\tau = 3.85 \pm 0.03$ ns. The VOAs were set at $L_1 = 0$ dB and $L_2 = -6$ dB, producing signal powers of 15.1 and 3.8 mW for the cw and ccw directions, respectively, measured as they enter the HNL fiber loop with Tap3 (1% tap coupler).

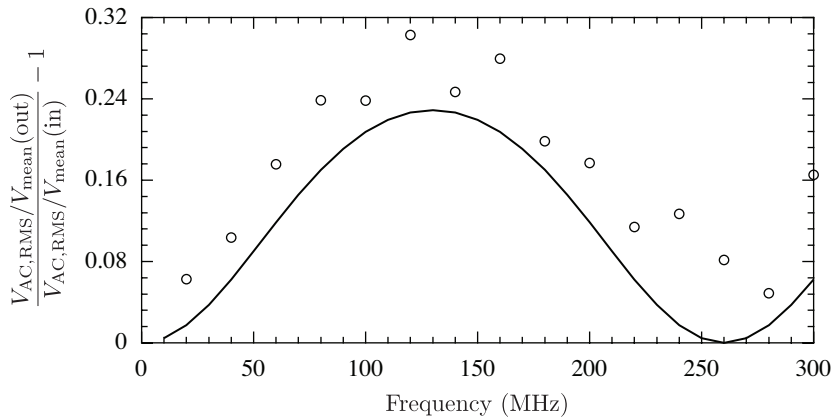


Figure 4.7: Experiment: AM response of NOLM

Data shows increase in modulation due to NOLM setup shown in Fig. 4.6. Arm mismatch $\tau = 3.85$ ns results in minimum nonlinear AM response at zero and 260 MHz. Solid curve shows theoretical expectation using fiber nonlinearity $\gamma = 9.5$ (W km) $^{-1}$.

The results are shown in Fig. 4.7 along with a theoretical prediction using the model described in relation to Fig. 4.5 with $\gamma = 9.5$ (W km) $^{-1}$ and $\ell'_{eff} = 1.78$ km. Figure 4.7 shows that the expected AM-response magnitude and trend, with minima at DC and $f_{am} = \frac{1}{\tau} \approx 260$ MHz, is supported by the data. The data in Fig. 4.7 appears shifted above the theoretical response uniformly across the frequency range measured. This is likely due to a combination of the measurement process and noise properties of the design. Since we are simply using the AC component of the detected voltage as our metric, any intensity noise imparted on the signal by the NOLM will appear as an increase in AM response, even if it is at other frequencies. The most likely source of intensity noise from the NOLM is the PBS-FRM combination. At $\lambda = 1559$ nm, we measured an extinction ratio for the folded loop of 21.8 dB by inserting a beam block in the adjustable delay and measuring the difference in power returning from the folded loop to Tap1 and Tap2 (see Fig. 4.6). Ideally, Tap2 should be dark, since no light is entering the folded loop from Arm 1. This small amount (0.7%) returning through the wrong NOLM arm will cause additional intensity noise at the NOLM output. This effect is studied in more detail in Sect. 7.3.1.

4.2.2 Engineering constraints

In the previous section, we showed that a NOLM with folded loop becomes insensitive to input amplitude modulation when the arm lengths are perfectly balanced. We must now consider the constraint this puts on engineering a NOLM-based gain equalizing system.

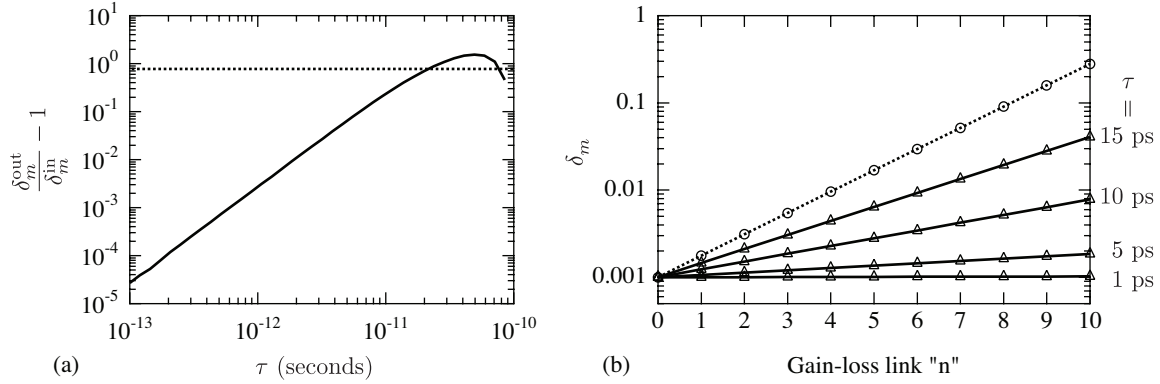


Figure 4.8: Amplitude stability of folded NALM vs. arm mismatch

A chain identical to Fig.'s 3.6 and 3.8 with folded NALMs is considered. Input signal has 10 GHz AM and $\delta_m = 0.1\%$. (a) Effect of single folded NALM on δ_m . (b) Evolution of δ_m across multiple gain-loss links for different values of τ . (a,b) Dashed curve shows effect of non-folded NALM.

We have seen that by reducing the arm time difference τ , we can widen the AM-insensitive frequency band to encompass the region from DC to $f \approx R_b$. For example, let's numerically explore a communication system modulated at $R_b = 10$ GHz and a NOLM chain identical to the one shown in Figs. 3.6 and 3.8, except with folded NALMs replacing the conventional NALMs. If we launch a signal with modulation depth $\delta_m = 0.1\%$, the NALM will increase δ_m at 10 GHz by a factor that depends upon τ , as shown in Fig. 4.8(a). Maximum AM responsivity occurs at $\tau = 50$ ps and is reduced by nearly 30 dB by reducing τ to 1 ps. The constant AM responsivity of a non-folded NALM is also shown (dashed line).

If we monitor the evolution of an initially small modulation as a signal propagates through multiple gain-loss links, we can see the dramatic improvement achieved by using a folded NALM and reducing the arm-length difference (Fig. 4.8(b)). After 10 links, the NALM chain with $\tau = 1$ ps has nearly 25 dB less modulation than the non-folded-NALM chain.

To more accurately simulate the performance of a folded-NOLM chain, the laser source intensity-noise spectrum must be considered and, more importantly, the amount of PM-AM conversion from fiber dispersion must be determined. The maximum allowable arm-length mismatch will then depend on the tolerable intensity noise level at the receiver. The nonlinear AM response of the folded NOLM at a given frequency may always be reduced by decreasing τ , but this will become increasingly difficult to engineer. A delay $\tau = 1$ ps corresponds to an arm-length mismatch of approximately 0.2 mm. We achieve this level of precision in the laboratory by measuring the time delay of the two arms with short pulses, adding fiber to the shorter arm to bring it within cm's of the longer arm's length, and using an adjustable delay to fine-tune the length

of one arm.

In a laboratory setting, it is not difficult to attain this level of length control by including an adjustable bulk-optic delay stage within the otherwise all-fiber experiment. In a commercial device, this type of construction will add complication and cost, but it should be practical. Practical techniques for accomplishing this arm-length matching or alternative means for suppressing the AM response remain as future work.

Chapter 5

Electrostriction in folded NOLMs

In Chapter 4, we described how the nonlinear switching performed by a folded NOLM should scale *only* with a signal’s average power, assuming any amplitude modulations have a temporal period T much greater than τ , the time delay from arm-length mismatch. We begin this chapter by providing experimental evidence in Sect. 5.1 that contradicts the above statement. We then proceed to provide in Sects. 5.2–5.3 theoretical evidence that the observed phenomena are due to electrostriction and provide an experimental “smoking gun”: irrefutable evidence that electrostriction is indeed the cause. In generating this evidence, we are the first to demonstrate the stimulation of guided acoustic waves using electrostriction in optical fibers. Finally, the impact upon the NOLM-based gain-equalization system is discussed in Sect. 5.4.

5.1 Observation of unexpected nonlinear effects

The experiments presented in this section are to serve as the motivation for exploring the effects of electrostriction in the folded NOLM. We begin by measuring the nonlinear switching with an experiment identical to that presented in Fig. 4.4 using the setup shown in Fig. 5.1. This experiment incorporates three principle changes from Fig. 5.1: 1) The DFB source is phase modulated at frequency $f_{pm} = 100$ MHz for SBS suppression; 2) the amplitude modulator is driven by a pulse generator, creating rectangular pulses in order to be able to vary the duty cycle (DC) (chopping the source into short pulses increases the peak output power from the EDFA); and 3) the arm mismatch delay is now $\tau \approx 1$ ns ($\Delta\ell \approx 20$ cm).

Rectangular pulses were launched with a period $T_{pulse} = 190$ ns and a duty cycle of either 100% (CI) or 10%. The total VOA loss was set at $L_1L_2 = 0.25$ (-6 dB) for all measurements. Figure 5.2 shows the output power P_A measured vs. asymmetry parameter ($L_1 - L_2$) for the two input signals with average power $\langle P_{cw} \rangle = \langle P_{ccw} \rangle = 24$ mW entering the HNL fiber when the two VOAs are set to full transparency. Unexpectedly, a dramatic change in the nonlinear response is

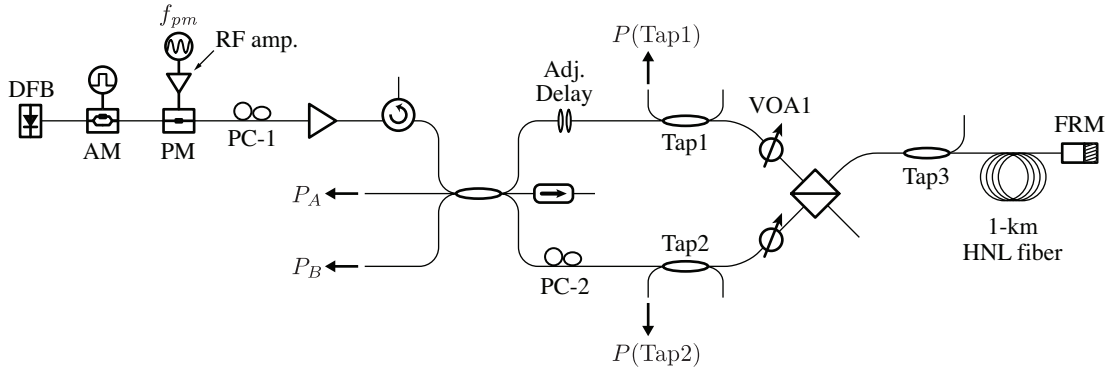


Figure 5.1: Schematic of experimental setup.

Using an amplitude modulator (AM) and pulse generator, variable-duty-cycle rectangular pulses are launched into the NOLM. Output P_A is measured vs. asymmetry parameter ($L_1 - L_2$) in Fig. 5.2. In Fig. 5.3(a), the ratio $P(\text{Tap1})/P(\text{Tap2})$ is measured vs. peak pulse power. In the absence of any nonlinear polarization rotation in the folded loop, this quantity should be invariant.

evident: the switching is greatly reduced for the 10%-DC pulses, whose peak power is 10 times larger than in the CI case. This result was unexpected because $\Delta\phi^{nl}$ should only scale with average power, as discussed in Chapter 4. This provided the first clue that our understanding of the folded NOLM was not complete.

In searching for the cause of this unexpected result, we found that the PBS did not always return the cw and ccw signals to the appropriate NOLM arms after returning from the FRM. The PBS splitting ratio $P(\text{Tap1})/P(\text{Tap2})$ should be constant for any NOLM input power.¹ We measured these powers when $L_1 = -6$ dB and $L_2 = 0$ dB with a total average power entering the HNL fiber $\langle P \rangle = 23.4$ mW (i.e., 4.7 mW and 18.7 mW from the cw and ccw directions, respectively). The duty cycle of the input pulses ($T_{pulse} = 190$ ns) was varied, resulting in a range of peak pulse powers P_{peak} . The results (Fig. 5.3(a)) show that the PBS splitting ratio was *not* constant with respect to P_{peak} . This result implies that the cw and ccw beams were experiencing a nonlinear polarization rotation in the folded loop that scaled with P_{peak} (as opposed to $\langle P \rangle$).

A nonlinear polarization rotation from the Kerr interaction of two co-propagating, orthogonal beams in non-PM fiber is not expected from the theory [64–66].² To rule out counter-propagating

¹ $P(\text{Tap1})/P(\text{Tap2}) = 1$ if all components are ideal. In reality, the tap couplers Tap1 and Tap2 have different splitting ratios, therefore $P(\text{Tap1})/P(\text{Tap2}) \neq 1$ under normal circumstances. Additionally, the insertion loss of any components between the tap couplers and the 3×3 coupler (e.g., the adjustable delay) will cause $P(\text{Tap1})/P(\text{Tap2})$ to deviate further from unity. When we measure the PBS splitting ratio we are only looking for relative changes, therefore the decibel scale may be arbitrarily shifted up or down.

²Counter-propagating interactions are ruled out because the effect scales with P_{peak} . See Sect. 4.1.3 for a summary of the phase shifts between orthogonal signals in a non-PM fiber. Chapter 6 explores the nonlinear interactions in a folded non-PM fiber more fully.

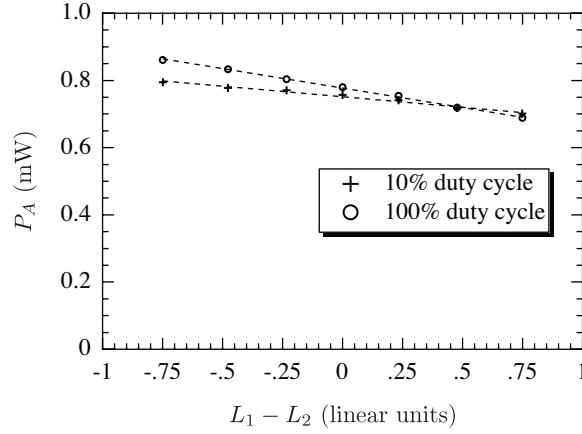


Figure 5.2: NOLM output vs. power asymmetry for CI and 10%-DC pulses.

The NOLM switching is shown for rectangular pulses with period $T_{pulse} = 190$ ns and $\langle P_{cw} \rangle = \langle P_{ccw} \rangle = 24$ mW entering the HNL fiber when VOAs are set to full transparency. The 10%-DC pulses, which have $10\times$ the peak power of the CI signal, exhibit reduced switching magnitude.

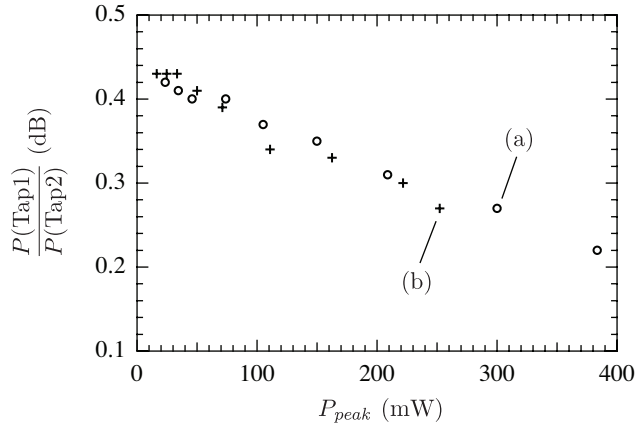


Figure 5.3: Peak-power dependence of PBS splitting ratio.

PBS splitting ratio $P(\text{Tap1})/P(\text{Tap2})$ is measured vs. P_{peak} for (a) folded NOLM shown in Fig. 5.1 and (b) NOLM with unidirectional loop shown in Fig. 5.4. The change in PBS splitting ratio indicates a nonlinear polarization rotation is occurring.

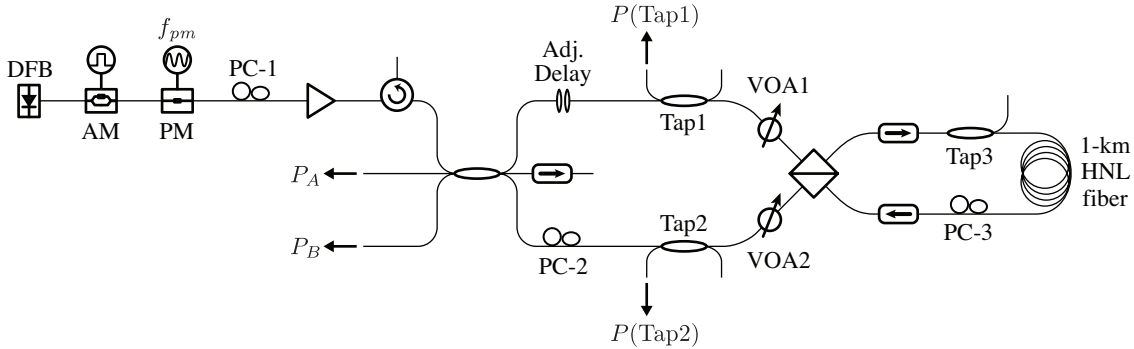


Figure 5.4: Schematic of NOLM with unidirectional fiber loop.

The NOLM in Fig. 5.1 is reconfigured such that the cw and ccw beams never counter-propagate. The FRM is removed and PC-3 is set such that the beams exit the appropriate PBS ports after traveling through the unidirectional loop. Isolators prevent any counter-propagating power.

nonlinear effects such as a Kerr-induced SOP rotation or SBS, we rearranged the NOLM folded loop into a unidirectional configuration, as shown in Fig. 5.4. The FRM has been removed and the far end of the fiber coil is attached to the fourth PBS port. Two isolators remove any counter-propagating beams and a new polarization controller PC-3 is used to adjust the SOP such that the cw and ccw beams return through the correct NOLM arms. In this unidirectional configuration, the cw and ccw beams travel different total optical paths since they are orthogonal in the HNL fiber loop.³ The output of the NOLM with unidirectional loop will therefore exhibit reduced stability since the common-path nature of the Sagnac interferometer has been removed. This is not of concern for the current experiment, since we are only examining the nonlinear polarization evolution in the unidirectional loop by measuring the ratio $P(\text{Tap1})/P(\text{Tap2})$. The results are shown in Fig. 5.3(b). The same P_{peak} -dependent PBS splitting can be seen in this unidirectional loop (the reduced HNL-fiber input power compared to the folded loop is due to the added insertion loss off the isolator). Interestingly, the magnitude of the effect does not appear to be reduced from the fact light is traversing the HNL fiber only once.

The experiments shown in this section have demonstrated that the NOLM output has a dependence upon peak pulse power for pulses that are much longer than the arm mismatch. Additionally, it appeared that the effect was primarily due to a nonlinear polarization rotation occurring in the folded loop. This causes a portion of the cw and ccw beams to return to the Sagnac coupler through the wrong arm, thereby disrupting the expected interference.

Through the course of experimentation, we empirically determined that these effects were

³In the folded loop, the signals double-pass the fiber coil after an FRM reflection, therefore traveling equal optical paths.

intimately linked to the arm mismatch $\Delta\ell$ and source phase modulation. We will not spend any more time showing the experimental results that led to our discovery that electrostriction was to blame; instead, we proceed straight to a description of the processes involved. With the newly gained understanding of the effect, we will then discuss why electrostriction will not be of concern in a practical NOLM-based gain-equalization system with high-modulation-frequency signals.

5.2 Electrostriction in folded NOLM

Electrostriction is a nonlinear process occurring in dielectric materials. It manifests itself as a deformation of a material that is subjected to an electric-field gradient. In essence, an electric dipole will experience a net force

$$\mathbf{F} = \frac{1}{2}\alpha\nabla(E^2), \quad (5.1)$$

where α is the molecular polarizability and E is the field [89]. Therefore, individual molecules of a dielectric material are always pulled toward regions of increasing field strength, independent of field sign.

5.2.1 Electrostriction in optical fibers

The mode propagating along an optical fiber has a field maximum on the central axis. The force exerted by electrostriction upon the silica fiber (5.1) is therefore always directed toward the center. This compression induces an increase in material density, along with a corresponding increase in refractive index. Electrostriction therefore contributes a Kerr-like nonlinear refractive index n_2 to an optical fiber with a response time on the order of 1 ns, which is related to the time required for the acoustic wave generated by the field to travel across the fiber core [90–94].

The most well-known electrostrictive process in optical fibers occurs during stimulated Brillouin scattering (SBS) [95]. When a signal and a counter-propagating “Stokes” signal have the right frequency separation ν_A , the spatial beating of the two fields electrostrictively generates a longitudinal acoustic wave guided by the fiber core. This acoustic wave (frequency ν_A) has just the correct period, speed, and phasing to reflect the forward- into the backward-propagating signal with the correct Doppler shift. Thus, SBS is usually an undesired effect that causes the depletion of a signal through nonlinear generation of a reflected Stokes wave.

Whereas SBS generates acoustic waves that travel along the fiber axis, other effects exist that involve transversely propagating acoustic waves. For instance, when a short pulse travels down an optical fiber, its presence generates a momentary material compression at its instantaneous position along the fiber. An acoustic pressure wave will be generated at that position; it travels away from the core and reflects from the cladding surface. After $t \approx 20$ ns—the time it takes to acoustic wave to travel from the core to the cladding, where it is reflected, and back to the

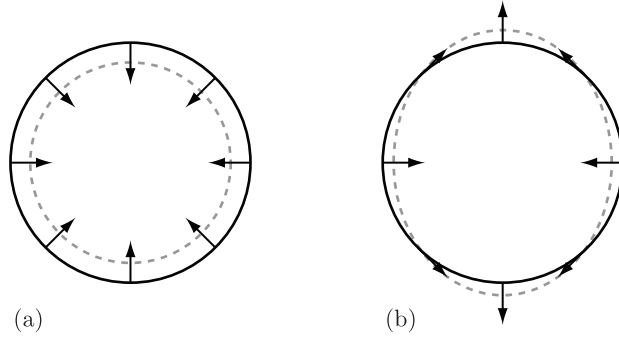


Figure 5.5: Electrostrictive forces and fiber deformations.

Arrows indicate direction of force. Dashed lines are exaggerated representations of fiber deformation. (a) Uniform compression resulting from \mathbf{f}_R . (b) Cross-sectional deformation induced by \mathbf{f}_{TR} when signal is polarized horizontally.

core—the acoustic pulse passes back through the core, where its presence can perturb a second optical pulse traveling ~ 20 ns behind the first pulse, causing the phase of this second pulse to be modulated and hence timing jitter after long propagation distances. This “long-range” interaction of neighboring pulses and its impact on soliton transmission systems has been studied by multiple researchers [92, 96–102]. It is these *transverse* acoustic waves that we shall utilize in Sect. 5.3 to demonstrate the existence of electrostriction-induced nonlinear effects in the folded NOLM.⁴

For an optical mode with transverse field distribution $F(r)$ and principle polarization axis aligned with x or y , Jaouën and du Mouza give the electrostrictional force

$$\mathbf{f} = \begin{pmatrix} f_r \\ f_\phi \end{pmatrix} = -\frac{\epsilon_r^2}{\rho} F \frac{dF}{dr} \begin{pmatrix} (p_{44} + 2p_{12})(I_x + I_y) + p_{44}(I_x - I_y) \cos 2\phi \\ -p_{44}(I_x - I_y) \sin 2\phi \end{pmatrix}, \quad (5.2)$$

where r and ϕ are the conventional cylindrical coordinates, ϵ_r is the relative dielectric permittivity, ρ is the material density, I_x and I_y are the intensities of the two linear SOPs, and $p_{12} = 0.27$ and $p_{44} = -0.0745$ are the strain-optic coefficients for fused silica [99, 100]. From (5.2), one can see that a radially compressive force \mathbf{f}_R exists proportional to the total power $I = I_x + I_y$. In addition, a non-azimuthally symmetric force is also present, which scales with the degree of linear polarization ($I_x - I_y$). Since this force manifests itself as a combination of torsional and radial forces, we shall denote it \mathbf{f}_{TR} . Unlike \mathbf{f}_R , which uniformly constricts the fiber, \mathbf{f}_{TR} deforms the circular fiber cross-section when $I_x \neq I_y$. A representation of the material deformations from these two forces is shown in Fig. 5.5.

⁴Note that we use the term “transverse” for acoustic waves that travel across the fiber, perpendicular to the fiber’s axis. We do *not* use the term to signify an oscillation transverse to the propagation direction, as is often the case in the study of vibrations and waves.

The polarization-dependent deformations associated with \mathbf{f}_{TR} are maximum for linear polarizations and zero for circular polarizations. Additionally, because of the photo-elastic effect, the deformed fiber will have an electrostriction-induced birefringence $B_s = |n_x - n_y|$ from the presence of \mathbf{f}_{TR} . In [103], Dement'ev et al. studied this effect with Gaussian beams in isotropic solids and determined that $B_s = 3.25 \times 10^{-19} E_0^2$ for a linearly polarized beam, where the E-field at the beam center E_0 has units of $\frac{V}{m}$. We may use this on-axis value as an estimate of the birefringence of an optical-fiber mode by using an intensity $I = P/A_{eff}$, where P is the mode's power and A_{eff} its effective area. After the necessary conversions, we are left with

$$\frac{B_s}{P_0} = 1.23 \times 10^{-8} \frac{1}{\text{mW}} \quad (5.3)$$

for a fiber with $A_{eff} = 20 \mu\text{m}^2$, a value common with available HNL fibers, including the one used in our experiments [61].

The intrinsic birefringence B_p of a non-PM fiber originates from randomly distributed perturbations to the fiber's geometry or internal strain and typically have beat lengths $L_b = \lambda/B$ in the range $10 \text{ cm} < L_b < 2 \text{ m}$ ($10^{-7} < B_p < 10^{-5}$) [53]. Therefore, for optical powers as small as several mW, the electrostriction-induced B_s can be similar in magnitude to the intrinsic birefringence of a typical SMF when the signal is linearly polarized. Electrostriction consequently has a sizable effect on the birefringence of non-PM fibers even at relatively low optical powers. For a circularly polarized signal, $B_s = 0$.

5.2.2 Electrostriction-induced polarization dynamics

We must now introduce the effects of electrostriction-induced birefringence changes occurring within the folded loop. As described in Sect. 4.1.2, the FRM returns light to the PBS in the orthogonal state regardless of the birefringence profile of the fiber. In essence, the polarization rotations occurring on the trip toward the FRM are precisely unwound on the return trip because the signal is traveling in the same medium. If a polarization controller is placed somewhere between the FRM and PBS, it may be adjusted to any possible position and the transmission of the folded loop will be unchanged (see Fig. 5.6(a)).

This behavior breaks down, however, if the birefringence experienced by the field at location z changes before the field returns to z after reflecting from the FRM (see Fig. 5.6(b)). When this occurs, the field's SOP upon returning to the PBS will no longer be in the correct state and it will be incorrectly routed by the PBS. Since we are working with fiber loops approximately 1 km in length, birefringence dynamics occurring on a time scale of $\sim 10 \mu\text{s}$ or less ($\sim 100+$ kHz) can cause changes in the PBS splitting ratio.

To understand how electrostriction can cause a dynamic birefringence to exist, we must consider the interaction between the phase modulation and NOLM arm mismatch. The signal,



Figure 5.6: Effect of dynamic birefringence on folded loop.

(a) For any static setting of a polarization controller (PC) in a folded loop, the FRM guarantees that the SOP returning to the PBS is orthogonal to the input. (b) If the birefringence of the fiber (represented by a PC) is time-varying, the SOP rotation induced on the backward-propagating wave is no longer equivalent to that experienced by the forward-propagating. Thus the power ratio of the PBS output ports changes.

with phase modulation $\phi_{pm} \cos(\omega_{pm}t)$, is split by the Sagnac coupler and recombined in the folded loop by the PBS (see Fig. 5.1). At any given location in the fiber, the time delay $\tau = (L_1 - L_2)/v$ from the arm mismatch will cause the cw and ccw signals to have a phase difference $\phi_0 + \Delta\phi(t)$, where

$$\Delta\phi(t) = \phi_{pm} \sin\left(\frac{\omega_{pm}\tau}{2}\right) \cos(\omega_{pm}t) \quad (5.4)$$

and ϕ_0 is the DC phase difference. Since the two signals are combined in orthogonal SOPs by the PBS, the oscillating $\Delta\phi$ will cause a time-varying polarization state. For instance, at a location in the folded fiber where the cw and ccw signals are aligned with the x - and y -axes, respectively, the net SOP of the two combined signals may be $\pm 45^\circ$, right-, left-circular, or any elliptical state with principle axes along $\pm 45^\circ$, depending upon the instantaneous value of $\Delta\phi$. This may be visualized on the Poincaré sphere (see Fig. 5.7(a)) by noting the two points A and B that represent the cw and ccw signals' SOPs, then drawing a great circle that is equidistant to both points (thick grey line, circle $S_1 = 0$). The net SOP (point C) may lie anywhere on this great circle, at an angular elevation given by

$$\theta(t) = \theta_0 + \Delta\phi(t), \quad (5.5)$$

where θ_0 depends upon the average phase difference ϕ_0 between the cw and ccw signals. Thus, the net SOP oscillates about θ_0 along the great circle with an angular magnitude $\phi_{pm} \sin(\omega_{pm}\tau/2)$.

Since B_s is a function of the SOP in the fiber (maximum for linear SOPs, zero for circular), an SOP modulation will cause a dynamic B_s to exist. It can be easily shown that $B_s \propto \sqrt{S_1^2 + S_2^2}$, since this denotes the degree of linear polarization. The specifics of the SOP modulation are complicated by the random evolution of both the polarization and phase difference ϕ_0 along the fiber; we will briefly discuss the salient concepts. First, we again consider a location in the folded fiber where the cw and ccw beams are aligned with the x and y axes as in Fig. 5.7(a) and the net

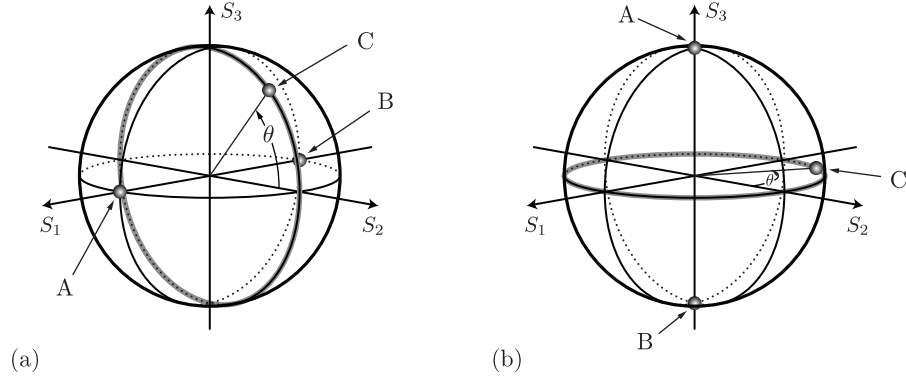


Figure 5.7: Combined polarization states in folded loop.

The SOPs of the cw and ccw signals are represented on the Poincaré sphere by points A and B. The net combined polarization state C from the sum of the two signals must lie on the great circle (thick, grey line) that is equidistant from A and B. The position of C along the circle depends upon the phase difference of the cw and ccw signals. (a) At a location in the fiber where A and B are x - and y -polarized, the net SOP lies along $S_1 = 0$ with a position defined by θ . (b) When A and B are circular states, the net combined SOP is a linear state with variable orientation. For a more detailed description of the Poincaré sphere, see Eqs. 6.10 and Fig. 6.5.

SOP exists on the circle $S_1 = 0$; thus $B_s \propto S_2$. This situation may occur at many positions along the length of the non-PM fiber, each with a different value of ϕ_0 (discussed in Sect. 6.2.2) and, therefore, θ_0 . The birefringence is thus $B_s(t) \propto \cos(\theta_0 + \Delta\phi(t))$, which, after inserting (5.4), can be Fourier expanded into the Bessel series [104]

$$B_s(t) \propto \sum_{n=0}^{\infty} \cos\left(\theta_0 + \frac{n\pi}{2}\right) J_n\left(\phi_{pm} \sin\left(\frac{\omega_{pm}\tau}{2}\right)\right) \cos(n\omega_{pm}t). \quad (5.6)$$

The implication from (5.6) is that a phase modulation at ω_{pm} generates modulations of B_s at $n\omega_{pm}$, where $n = 0, 1, 2, \dots$. Eq. (5.6) is valid at any location in the fiber where the cw and ccw signals are linearly polarized. The orientation of B_s will depend upon the direction of the two linear SOPs.

Now consider a location in the fiber where the cw and ccw signals are right- and left-circularly polarized, labeled A and B in Fig. 5.7(b). The SOP of the combined signal lies on the great circle $S_3 = 0$. In this scenario, the magnitude of $B_s \propto \sqrt{S_1^2 + S_2^2}$ is not affected by a modulation $\theta(t)$, only the orientation of the birefringence axes is. An expression similar to (5.6) could be derived for $B_s(t)$ in this case. It would show that a phase-modulated signal will induce modulations in the birefringence orientation at the harmonics $n\omega_{pm}$. To generalize further, when the SOPs A and B are any orthogonal elliptical states, a combination of the magnitude and orientation of

B_s will be modulated at the frequencies $n\omega_{pm}$. In general, this time-varying birefringence will tend to depolarize the optical mode when observed on a time-scale longer than the modulation period.

We will not attempt to further quantify the birefringence dynamics in the folded loop and their impact on the SOPs returning to the PBS. To properly accomplish this, one must consider the random evolution of both the SOP in the fiber and the phase difference ϕ_0 . The effect of dynamic birefringence upon the SOP rotations of the forward- and backward-propagating signals must then be analyzed, which likely requires a numerical analysis. Such analysis would be complex and time consuming, but it would not shed new light on the physics of the problem.

With the understanding that an electrostriction-induced dynamic birefringence exists that can affect the the PBS splitting ratio, we can postulate that electrostriction is capable of the phenomena presented in Sect. 5.1. In Sect. 5.3, we present irrefutable proof that changes in the PBS splitting ratio can indeed be attributed to electrostriction.

5.3 Stimulated vibrational modes of optical fiber

5.3.1 Thermally induced vibrational modes

The fused silica composing an optical fiber, like any elastic material, supports vibrational waves. Due to the fiber's finite extent (in two dimensions), the interference of waves reflecting off the cladding surface cause resonant vibrational modes to exist at specific frequencies — similar to the standing-wave patterns seen on the surface of water in a glass that has been jostled.

Neglecting any external sources, the vibrational modes are populated from the thermal vibrations of the silica molecules. The interaction of an optical mode with these thermally excited acoustic modes was first demonstrated by Shelby et al. and termed *guided acoustic-wave Brillouin scattering* (GAWBS) [105, 106]. The modes involved are classified as radial (R_{0m}) and torsional-radial (TR_{2m}) due to their respective symmetries. The symmetric dilational R_{0m} modes involve material displacements in only the radial direction, independent of azimuthal angle ϕ . In contrast, the TR_{2m} modes' radial and azimuthal displacements vary sinusoidally with 2ϕ and can be visualized as a deformation of the circular cross-section into an oblong shape, similar to Fig. 5.5(b). The subscripts $m = 1, 2, 3, \dots$ determine the number of nodes in the mode's radial direction. Via the photo-elastic effect, the strains associated with the vibrational fiber modes can perturb the optical signal. The R_{0m} modes apply a uniform phase modulation to an optical mode, while the TR_{2m} modes introduce a birefringence that tends to depolarize the mode.

As such, GAWBS represents a source of thermal noise source in fiber transmission, and this effect has been studied by several researchers [105–108]. The typical experimental procedure involved using heterodyne detection of an optical signal to measure the frequency shifts imparted by the R_{0m} modes with a spectrum analyzer. For the depolarized scattering from TR_{2m} modes, a

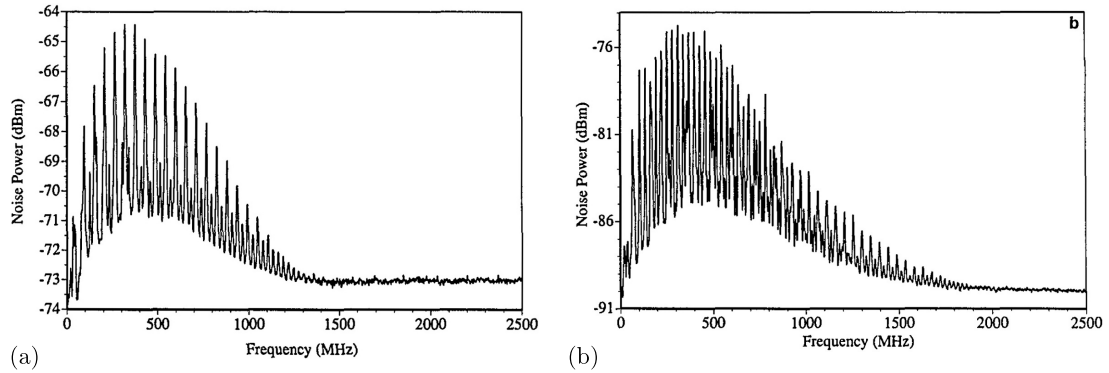


Figure 5.8: GAWBS spectra for 125- μm -diameter fiber.

Figures reproduced from [108]. Detected noise power induced by thermally excited (a) R_{0m} modes and (b) TR_{2m} modes. Spectra show the quantized frequencies of resonant vibrational modes. Poor overlap with the optical mode at frequencies above ~ 1 GHz provide a frequency limit above which GAWBS has no effect on noise.

polarizer is used to measure the frequency dependence of the polarization changes. Figures 5.8(a) and (b) show GAWBS spectra for a fiber with a 125- μm diameter reproduced from Ref. [108]. The specific resonant frequencies f_{0m} and f_{2m} of the R_{0m} and TR_{2m} modes, respectively, may be calculated from the material properties and diameter. The minimum frequencies for both mode symmetries—corresponding to the R_{01} and TR_{21} modes—in a 125- μm -diameter SMF are ~ 20 MHz, which is consistent with the lowest frequency peaks in Figs. 5.8(a) and (b). As m is increased, the radial nodes move toward the fiber axis until the optical mode will begin to sample both positive and negative regions of the vibrational phase perturbation [108]. Because of this reduced overlap between the vibrational and optical modes, the detected noise power declines above ~ 1 GHz. A detailed analytic derivation of the vibrational fields and frequencies can be found in [106]. The predicted resonant frequencies agree well with experimental observations.

5.3.2 Electrostrictive stimulation of vibrational modes

The astute reader has already recognized that the electrostrictive forces (5.2) have the correct symmetries to stimulate R_{0m} and TR_{2m} vibrational modes. In the folded NOLM, we are concerned with the change in SOP caused by electrostriction, and therefore we can ignore the R_{0m} modes as they do not generate a birefringence. The TR-inducing force \mathbf{f}_{TR} is aligned with the principal axis of the SOP and scales with the degree of linear polarization $\sqrt{S_1^2 + S_2^2}$. As discussed in Sect. 5.2.2, these values oscillate at $n\omega_{pm}$ ($n = 1, 2, 3, \dots$) when the source is phase modulated at ω_{pm} and an arm mismatch τ exists. Therefore, we should be able to electrostrictively

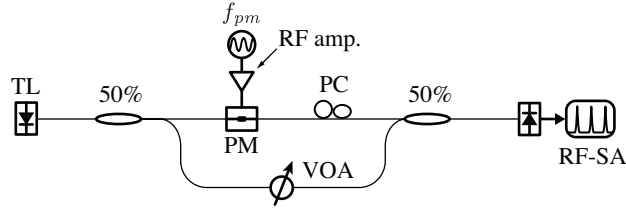


Figure 5.9: Schematic of setup used to calibrate phase modulator.

A fiber Mach-Zehnder interferometer is constructed from two 50% couplers. Light is input from a tunable laser (TL). One arm contains the phase modulator (PM) and a PC to adjust the SOP. Second arm has VOA that can be used to match power in both arms. An RF spectrum analyzer (RF-SA) was used to detect the frequency components of the interferometer output.

pump a specific TR_{2m} mode when $nf_{pm} = f_{2m}$. When this condition is met, the electrostriction-induced material strains should be resonantly enhanced, just as the height reached by a child on a schoolyard swing is maximized when she pumps her legs in phase with the resonant frequency. Demonstrating this resonant behavior with our polarization-rotation measurements will serve as strong evidence that electrostriction is indeed the cause.

The phase modulator and its driving electronics in Fig. 5.1 were calibrated using a Mach-Zehnder fiber interferometer as shown in Fig. 5.9. Light from an external-cavity tunable laser (TL) set to $\lambda = 1559$ nm was split by a 50% fused coupler. The upper arm of the interferometer included the electro-optic phase modulator (PM) and a polarization controller (PC) to make the interfering signals' SOPs identical. The lower arm contained a VOA that allowed us to set the transmitted power from each arm to be equal. A second 50% coupler combined the two signals. The detected power was monitored with an RF spectrum analyzer (RF-SA). It can easily be shown that the detected power at the first and second harmonic of f_{pm} are

$$P(f_{pm}) \propto J_1(\phi_{pm}) \sin \phi_b, \quad (5.7a)$$

$$P(2f_{pm}) \propto J_2(\phi_{pm}) \cos \phi_b, \quad (5.7b)$$

where ϕ_b is the bias phase of the interferometer. Since no effort was made to maintain a constant arm-length difference in the presence of environmental perturbations, ϕ_b drifted continually. This drift allowed the output to occasionally (for a few seconds) reach the maximum values of $P(f_{pm})$ and $P(2f_{pm})$, which were stored with the RF-SA. The maximum value of each corresponds to the sine and cosine terms to equal one. The ratio $P(f_{pm})/P(2f_{pm}) = J_1(\phi_{pm})/J_2(\phi_{pm})$ could then be used to determine ϕ_{pm} as a function of the applied voltage.

Due to a lack of RF electronics capable of monitoring the voltage at the PM input, we settled for a calibration of ϕ_{pm} vs. voltage applied to the RF amplifier by the function generator V_{fg} .

The saturation of the RF amplifier varied considerably in the frequency range of interest (0–1 GHz). With $V_{fg} = 100$ mV, the PM response was sampled between 0 and 1 GHz and was found to lie within $\phi_{pm} = 1.39 \pm 0.3$ rad. This value was used for all subsequent measurements. While this is not a very precise calibration, it is sufficient for our goal of demonstrating the specific resonant frequencies.

The PM was returned to the experimental setup shown in Fig. 5.1, which we used to measure the PBS splitting ratio $P(\text{Tap1})/P(\text{Tap2})$ at multiple phase modulation frequencies f_{pm} . The AM was operated with a pulse generator to create rectangular pulses with 7% duty-cycle, thus giving a ~ 14 -fold increase in peak power after the EDFA compared to a CI input. The VOAs were adjusted such that $L_1 = -5.6$ dB and $L_2 = 0$ dB. Using Tap3, the average power entering the HNL fiber was measured to be $\langle P \rangle = 21$ mW, thus $P_{peak} = 300$ mW. The tap-coupler output powers were measured using the analog outputs of two power meters with a computerized data-acquisition system. The ratio was stored every 1 MHz from 20 to 990 MHz, limited by the function generator.

Figure 5.10(a) shows the PBS splitting ratio when the arm-mismatch delay was $\tau = 1.5$ ns. The thick grey line indicates the PBS splitting with 14-ns-long pulses, while the thin black line corresponds to 100-ns pulses. Both cases had identical duty cycles and peak powers. Both imply an SOP rotation in the folded loop that varies with frequency, but the shorter pulses do not exhibit the resonant enhancement from the TR_{2m} modes. This is because (1) the pulse length is shorter than the time it takes for the acoustic energy to propagate from the fiber core to the cladding and back (~ 20 ns) and (2) the acoustic modes have a damping time of approximately 100 ns due to absorption at the cladding-jacket interface [102, 108]. Hence the vibration of any induced TR_{2m} modes has dissipated before the following pulse passes, 190 ns later. When the pulse length is increased to 100 ns, several acoustic wave round trips occur within a single pulse. At the resonant frequencies f_{2m} , the vibrational displacements are resonantly enhanced by the oscillating SOP through electrostriction. The resulting large-magnitude TR_{2m} modes cause a dynamic birefringence through the photo-elastic effect, which in turn causes the signal returning to the PBS to have a rotated SOP.

Figures 5.10(b) and (c) correspond to the same 100-ns pulses, but with arm-mismatch delays $\tau = 1.05$ and 2.6 ns, respectively. The three plots (a–c) demonstrate that no electrostriction-induced dynamic birefringence is generated when $f_{pm} = n/\tau$ ($n = 1, 2, 3, \dots$), e.g., frequencies identified by “ \uparrow ” in Fig. 5.10. At these frequencies, $\Delta\phi(t) = 0$ in (5.4) due to the sinusoidal frequency response. The spectra demonstrate that the envelope of the effect depends upon τ , but the resonant frequencies f_{2m} are constant. The different arm mismatches were achieved by adding fiber patchcords between the 3×3 coupler and adjustable delay (see Fig. 5.1). Because this changed the insertion loss of arm 1, the initial value of $P(\text{Tap1})/P(\text{Tap2})$ was different for each of the three spectrum measurements. We have arbitrarily shifted the results (in decibels)

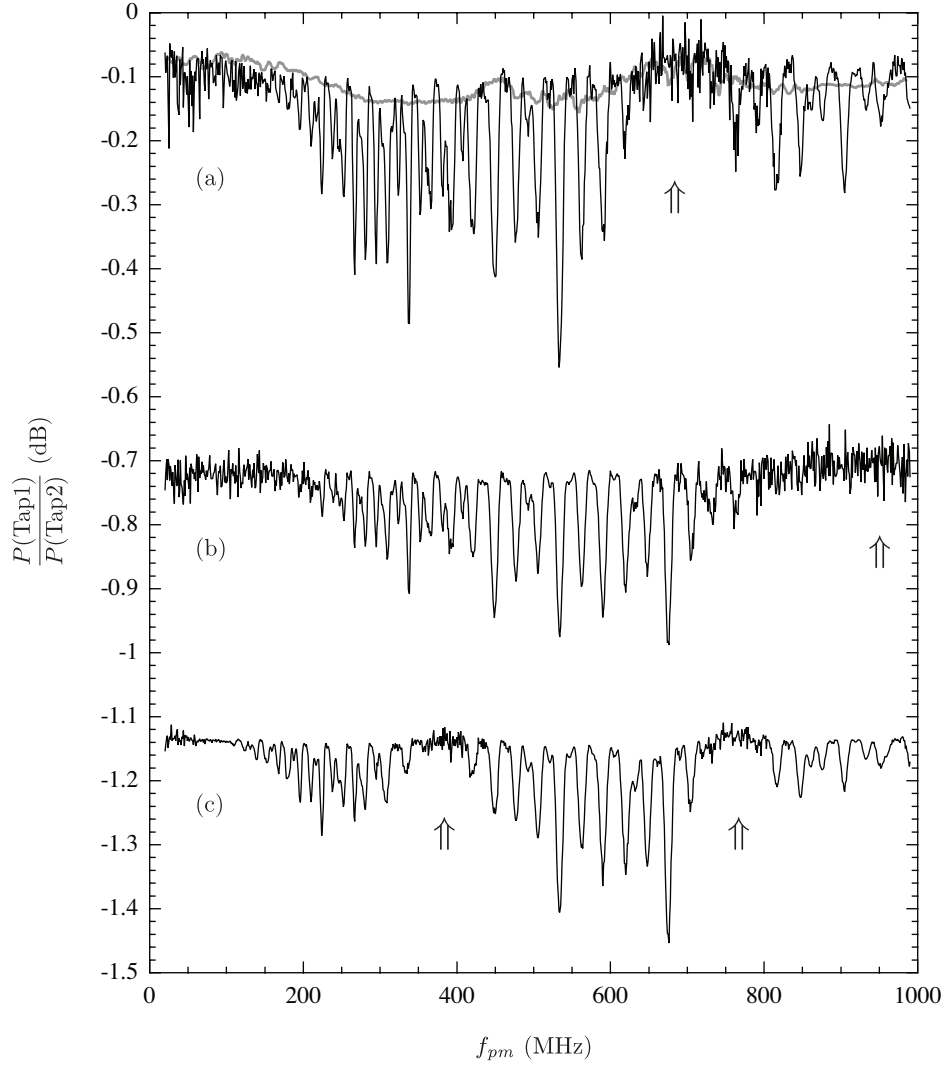


Figure 5.10: PBS splitting ratio vs. PM frequency.

Data acquired with setup shown in Fig. 5.1. Pulses with period $T = 190$ ns and 7% duty cycle were launched. Peak power entering loop $P_{peak} = 300$ mW. (a) Arm-mismatch delay $\tau = 1.5$ ns; $L_1 = -5.6$ dB and $L_2 = 0$ dB. 14-ns pulses (thick grey line) have small change in PBS splitting from electrostriction-induced SOP rotation. 100-ns pulses (black line) are long enough to experience resonant enhancement. (b) $\tau = 1.05$ ns; $L_1 = -5.1$ dB and $L_2 = 0$ dB. (c) $\tau = 2.6$ ns; $L_1 = -4.7$ dB and $L_2 = 0$ dB. Note that while envelope of effect scales with τ , the specific resonant frequencies are constant. Frequencies with zero electrostrictive response are denoted with “ \uparrow ”. Plots have been arbitrarily shifted so they do not overlap.

Table 5.1: Comparison of resonant frequencies from 1st and 2nd harmonics of f_{pm} .

The resonance frequencies from Fig. 5.10(c) between 448 and 704 MHz (1st and 3rd columns) are compared to the resonances between 224 and 352 MHz (2nd and 4th columns) in Fig. 5.10(a). The smaller of each frequency pair corresponds to the stimulation of a TR_{2m} mode at $f_{2m} = 2f_{pm}$. Data was acquired at 1-MHz intervals.

$f_{pm} = f_{2m}$ (MHz)	$f_{pm} = f_{2m}/2$ (MHz)	$f_{pm} = f_{2m}$ (MHz)	$f_{pm} = f_{2m}/2$ (MHz)
448	224	590	295
477	238	620	310
506	253	648	324
534	267	676	338
563	281	704	352

since we are only concerned with the relative change in PBS splitting ratio.

From Fig. 5.10, it also *appears* as if the density of TR_{2m} modes increases at $f \lesssim 500$ MHz. In reality, this is an artifact of the SOP modulation at harmonics of f_{pm} . Even though we are limited to frequencies below 990 MHz, we know from [105–108] that the acoustic modes have poor overlap with the optical mode above ~ 1 GHz, as discussed in Sect. 5.3.1. Thus, when $f_{pm} \lesssim 500$ MHz, we can stimulate TR_{2m} modes with $f_{2m} = f_{pm}$ and $2f_{pm}$. Likewise, at $f_{pm} \lesssim 333$ MHz, we can stimulate TR_{2m} modes with $f_{2m} = f_{pm}$, $2f_{pm}$, and $3f_{pm}$, and so forth. Ignoring the envelope created by the sine term in (5.6), the birefringence induced by the n^{th} harmonic goes as $J_n(\phi_{pm})$. For our modest phase modulation magnitude $\phi_{pm} \approx 1.39$ rad, the influence of the third harmonic is only 8% that of the first, and even less for all higher harmonics. We therefore only expect to see resonances from the first and second harmonic of f_{pm} . Since the region $f_{pm} \gtrsim 500$ MHz should only contain resonances with $f_{2m} = f_{pm}$, we can record the frequencies f_{2m} from Fig. 5.10(c) between 448–704 MHz. These can be compared with the lower frequency range 224–352 MHz that is clearly visible in Fig. 5.10(a). As seen in Table 5.1, each higher-frequency resonance corresponds precisely to another generated by the second harmonic of f_{pm} , agreeing well with our theory.

The sign of the change in PBS splitting depends upon the power imbalance from $(L_1 - L_2)$. Any photons routed incorrectly by the PBS due to a polarization rotation will see the same VOA twice before being detected at one of the tap couplers (see Fig. 5.1). The electrostriction-induced SOP rotation therefore causes $P(\text{Tap1})/P(\text{Tap2})$ to decrease when $L_1 < L_2$, i.e., when VOA1 attenuates more than VOA2. This effect is shown in Fig. 5.11(a) when $(L_1 - L_2) = \pm 0.66$, $L_1 L_2 = 0.34$ (-4.66 dB), and $\tau = 2.6$ ns with the same optical pulses used for Fig. 5.10(c).

Finally, Fig. 5.11(b) shows the power dependence of the electrostriction-induced effects. We

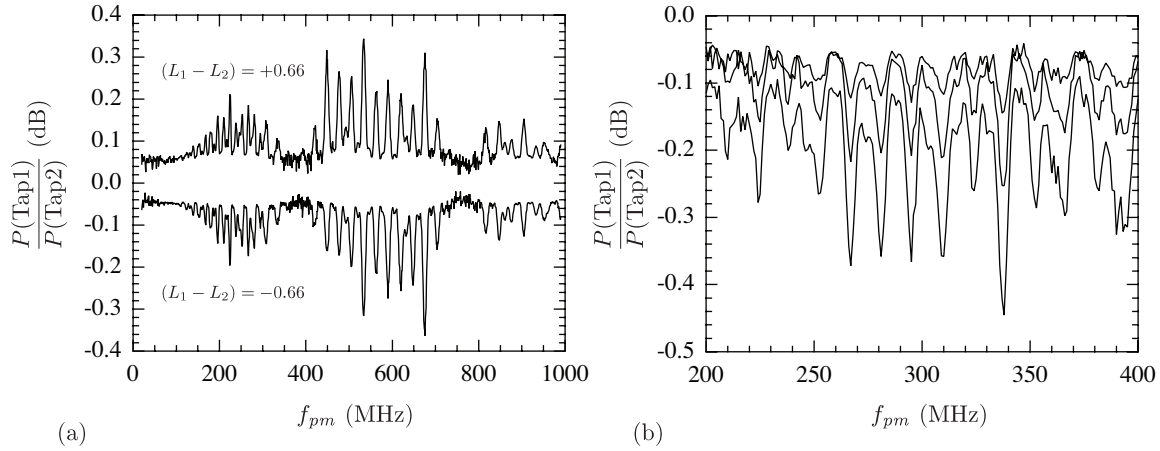


Figure 5.11: Acoustic resonances versus changes in power magnitude and symmetry.

(a) When VOA roles are reversed, the electrostriction-induced dynamic birefringence causes the change in PBS splitting ratio to change signs; $L_1 L_2 = -4.66$ dB; $\tau = 2.6$ ns. (b) Resonances become weaker as pulse power is decreased. From lowest trace up, $P_{peak} = 300, 150, \text{ and } 75$ mW; $\tau = 1.5$ ns.

used the same parameters as Fig. 5.10(a) and an additional VOA at the NOLM input to scale the input power. Since the induced birefringence (5.3) scales with power, the effect on the PBS splitting ratio decreases as we reduce P_{peak} from the previous value of 300 mW to 150 mW and 75 mW.

In this section, we demonstrated that we are able to stimulate TR_{2m} acoustic modes through electrostriction. This required using pulses longer than the acoustic round-trip time (~ 20 ns). We have not attempted a complete analysis of the effect, as it is not central to our goal of developing an operational NOLM gain equalizer. The presence of specific acoustic-mode resonances has strengthened our hypothesis that electrostriction was the cause of the observations shown in Sect. 5.1. To the best of our knowledge, this is the first time TR_{2m} resonances have been excited and observed using electrostriction. The setup used a phase-modulated source and folded NOLM with mismatched arm lengths to generate a modulated SOP in the folded loop. Through electrostriction, this modulation caused acoustic vibrations to build up and resonate in the fiber when at the proper frequency. The resulting material strains caused a dynamic birefringence, disrupting the SOP returning to the PBS. The setup proves to be a relatively simple method of exploring the acoustic resonances in optical fiber and may be easily constructed by other researchers who wish to conduct further investigations.

5.4 System impact

The experimental observations in Sect. 5.1 raised questions regarding the ability of the folded NOLM to operate as a gain equalizer. First, an instantaneous-power-dependent change in the NOLM-switching magnitude was observed with pulses much longer than the arm-mismatch delay τ (Fig. 5.2). This result was contrary to the expected behavior of the folded NOLM (Sect. 4.2), and it could have implications for the NOLM amplitude stability. We determined that this change in behavior was a result of the signals not entirely exiting the folded loop in the correct directions. When the cw and ccw signals return from the FRM, the PBS should route them to the Sagnac coupler via the opposite arm through which each entered. However, Fig. 5.3 demonstrated a power-dependent change in the PBS splitting ratio, implying a nonlinear polarization rotation was present in the folded loop. This is of concern because any photons routed through the wrong arm by the PBS will beat with the signal at the output, thereby introducing intensity noise. This noise source will be discussed in more detail in Chapter 7.

The power-dependent polarization changes in the folded loop could not be explained with the Kerr effect. We were able to demonstrate that electrostriction was to blame by pumping the resonant vibrational modes of the fiber, which greatly increased the magnitude of the measured polarization changes. The induced dynamic birefringence in the folded fiber loop is directly related to the source modulation and NOLM arm-length mismatch. The combination of $\phi_{pm}(t)$ and $L_1 - L_2 \neq 0$ allows the orientation of the local E-field in the folded fiber to oscillate in time at f_{pm} , which in turn introduces a dynamic birefringence through electrostriction and the photo-elastic effect. Electrostriction is a relatively slow interaction compared to the Kerr effect. The frequency response has been analyzed by Buckland and Boyd in [90]. We can calculate the frequency response of the electrostriction-induced index change in an optical fiber using the expression given in [90] for $H(\Omega)$. Using material parameters for fused silica given in [90], the result for two different fibers is shown in Fig. 5.12(a) after being normalized to $H(0) = 1$. The different frequency responses for the SMF-28 and HNL-DSF fibers result from their different mode-field diameter $d_{smf} = 10.4 \mu\text{m}$ and $d_{hnl} = 4 \mu\text{m}$, respectively [61, 109]. Since it takes longer for the acoustic wave to propagate across a larger optical mode, the SMF-28 fiber has the slower frequency response.

Importantly, the main conclusion of this study is that in a real communication system, the effects of electrostriction will be negligible for two reasons. First, above ~ 1 GHz, the electrostriction-induced index change declines as $1/f^2$. When the NOLM is utilized in a communication system modulated at the bit rate R_b , the signal encompasses a band of frequencies in the vicinity of $f = R_b$ (the extent of the signal's bandwidth and its exact central frequency depends upon the modulation scheme [71]). As seen in Fig. 5.12(a), a 25-dB decrease of the electrostrictive nonlinearity occurs at $f = 10$ GHz when a HNL-DSF is used in the NOLM. Further reductions in electrostrictive response are predicted as bit rates are increased—deployed systems

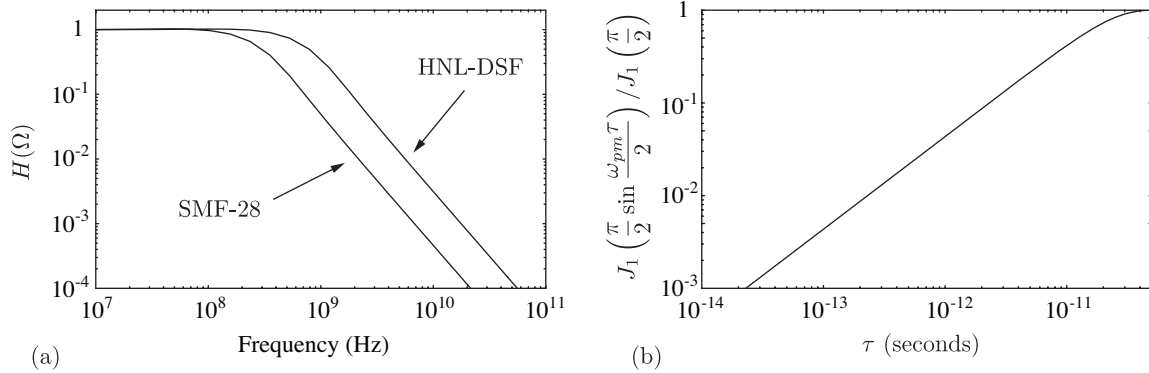


Figure 5.12: Magnitude of electrostrictive effects.

(a) Calculated frequency response H of electrostriction in Corning SMF-28 fiber and HNL-DSF with mode-field diameters $10.4 \mu\text{m}$ and $4 \mu\text{m}$, respectively. Due to the slow response of electrostriction, the effect decreases quickly above ~ 1 GHz. (b) Electrostriction-induced dynamic birefringence in folded loop scales with arm-length mismatch. For $\phi_{pm} = \pi/2$ at $f_{pm} = 10$ GHz, birefringence modulation is maximum at $\tau = 5$ ns and declines as τ is reduced.

are beginning to appear with bit rates of up to 100 Gb/s. Second, the birefringence modulation at ω_{pm} in the folded loop (5.6) scales with $J_1(\phi_{pm} \sin(\omega_{pm}\tau/2))$. Therefore, the arm-length matching required for nonlinear amplitude stability (Sect. 4.2) also serves to reduce the effects of electrostriction. The reduction in electrostriction-induced dynamic birefringence at $f_{pm} = 10$ GHz when $\phi_{pm} = \pi/2$ is shown in Fig. 5.12(b) versus arm-length-mismatch delay τ . A 14-dB reduction is realized when τ is reduced to 1 ps.

Because the effects of electrostriction are reduced dramatically at the frequencies used for long-haul telecom applications and at the allowable amount of arm mismatch (as dictated by the amplitude instabilities presented in Sect. 4.2), we do not expect electrostriction to be of concern in the NOLM-based gain-equalization system. Using the above estimates, the effects observed in our prototype would be reduced by nearly 40 dB at a frequency of 10 GHz, and an even greater reduction when R_b is increased and τ decreased.

One might also ask whether the nonlinear change in refractive index from electrostriction would add to the nonlinear phase difference $\Delta\phi^{nl}$. Electrostriction *does* contribute to the intensity-dependent refractive index [90], but the index change will be identical for both the cw and ccw beams. Therefore, electrostriction will not induce a phase *difference* in the folded NOLM.

Chapter 6

Nonlinear response of folded NOLMs: Effects of balanced arm lengths

Chapters 4 and 5 introduced three reasons why the two arms in a folded NOLM need to have balanced lengths; namely to reduce nonlinear amplitude instability, electrostriction-induced intensity noise, and acoustic pickup. These effects each occur at frequencies below $f \approx R_b$, 1 GHz, and 100 kHz, respectively. Since modern communication systems typically have $R_b \gg 1$ GHz, the arm-mismatch tolerance is predominantly determined by the nonlinear amplitude stability (Sect. 4.2).

Minimizing arm-length mismatch is purely an exercise in optical engineering. While seeking this simple objective in the laboratory, we found that the system's behavior changes dramatically when the mismatch approaches zero. Specifically, the nonlinear phase difference $\Delta\phi^{nl}$ that provides the switching needed for automatic gain equalization disappears. In Sect. 6.1 we present these unexpected experimental results along with observations that provide clues that the cause is related to the phase modulation of the input signal. To model this presumed effect, we introduce a new theory in Sect. 6.2 specifically formulated to determine the third-order nonlinear interactions in a *folded* Sagnac loop. The revised theory predicts that $\Delta\phi^{nl}$ indeed vanishes in a folded NOLM with balanced arm lengths, confirming our earlier experimental results. Fortunately, we are able to introduce a simple solution (Sect. 6.3) that allows the successful demonstration of the balanced folded NOLM in Sect. 6.4.

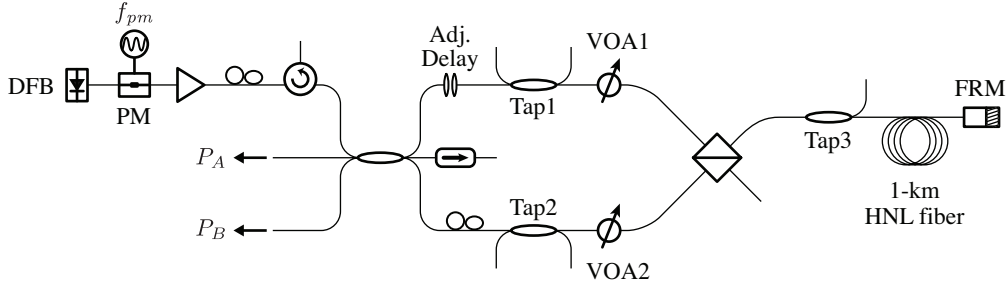


Figure 6.1: Schematic of experiment measuring $\Delta\phi^{nl}$ vs. arm mismatch.

Arm-length mismatch $\Delta\ell$ is altered by adding or removing fiber from the upper arm (Arm 1). Length difference is measured using a pulsed input and measuring the time difference at the PBS. $\Delta\phi^{nl}$ is calculated using the output power P_A as the power balance is changed with the VOAs.

6.1 Unexpected observations in folded NOLM with balanced arms

The nonlinear Kerr phase shifts presented in Sect. 4.1.3 provide no mechanism for $\Delta\phi^{nl}$ to depend upon arm mismatch $\Delta\ell = (\ell_1 - \ell_2)$ with a CI signal. Using this known nonlinear-optical theory, in the presence of a CI signal, we expected the nonlinear response of the folded NOLM (see Fig. 4.4) to be unchanged by reducing $\Delta\ell$, as required and as we did in the laboratory to minimize the NOLM's AM response. However, quite the opposite was observed.

We measured the nonlinear response of a folded NOLM using the experiment setup shown in Fig. 6.1. The 1559-nm DFB signal was phase modulated at 125 MHz for SBS suppression. The length of Arm 1 was modified by adding or removing lengths of fiber, with fine tuning possible with adjustable delay optics. VOAs provided the necessary power imbalance in the folded loop. As with the experiment shown in Fig. 4.4, the total loss provided by the VOAs was held constant at $L_1 \times L_2 = 0.25$ (-6 dB) while the difference $(L_1 - L_2)$ was varied. Since $\Delta\phi^{nl}$ is proportional to the power imbalance, by doing so we are effectively scaling $\Delta\phi^{nl}$ and keeping the total NOLM insertion loss constant. The power entering the HNL fiber loop from each arm was 17.5 mW when the VOA loss was set to zero dB.

We expected the result of this experiment to be similar to that shown in Fig. 4.4. In that experiment, the powers exiting the 3×3 coupler's ports were measured vs. $L_1 - L_2$. In the current experiment, we again measure the output power and then convert these power measurements to values of $\Delta\phi^{nl}$ using the transfer function (2.2) with the nonlinear phase difference (4.7) for a NOLM with VOAs. Therefore, we should find a linear relationship between $\Delta\phi^{nl}$ and $L_1 - L_2$ as in (4.7).

The output power at the $\pi/3$ -biased port (P_B) was measured with an optical power meter

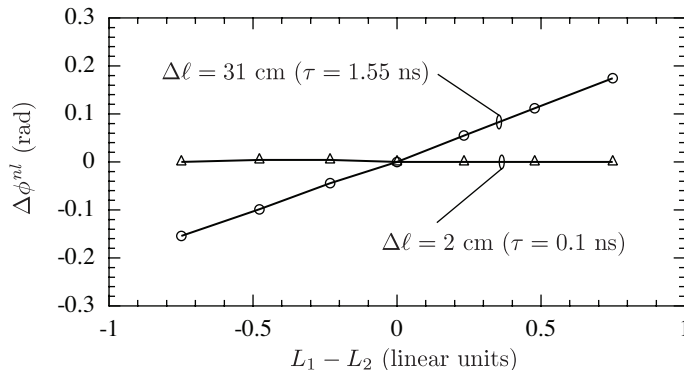


Figure 6.2: Nonlinear phase difference in folded NOLM vs. arm mismatch.

When NOLM arm lengths are nearly matched, $\Delta\phi^{nl} \rightarrow 0$. $L_1 \times L_2 = 0.25$ (-6 dB) for all measurements. Experiment schematic shown in Fig. 6.1.

and is used to determine $\Delta\phi^{nl}$. The results are shown in Fig. 6.2 for two values of the length mismatch $\Delta\ell$. When $\Delta\ell = 31$ cm, $\Delta\phi^{nl}$ has the expected linear response to $L_1 - L_2$. However, $\Delta\phi^{nl}$ virtually disappears when $\Delta\ell$ is reduced to 2 cm! The results when $\Delta\ell = 2$ cm were not affected by changing f_{pm} , nor by removing the phase modulation altogether and instead dithering the DFB current to suppress SBS (see Sect. 4.1.4).

An important point must be stressed at the outcome of this experiment: As $\Delta\ell$ is reduced to zero, a condition we *must* fulfill to eliminate the amplitude instability issues, the nonlinear phase difference that is indispensable for the gain equalization system to work also goes to zero. This behavior is not explained by existing theory. Understanding the origin of this loss of $\Delta\phi^{nl}$ is needed to complete the gain equalization research, a task we undertook with further measurements and a revised model.

It was empirically determined that, in addition to $\Delta\ell$, this interesting nonlinear behavior also depended upon the frequency of the phase modulation used for SBS suppression. Operating at the right-most datapoint in Fig. 6.2 with $\Delta\ell = 31$ cm ($L_1 = 1$, $L_2 = 0.25$), the output of the NOLM was measured for f_{pm} varying from 40 to 600 MHz (we could not operate below $f_{pm} \approx 40$ MHz due to SBS). The power at the $\pm\pi/3$ -biased ports (P_A and P_B) was monitored with optical power meters. The uncalibrated analog outputs of the meters were fed into a computer-controlled data acquisition system, where their ratio was saved. From the ratio of the two outputs, we could determine the change in the net phase difference independent of absolute power level and without requiring photodiode calibration. Since the meters were uncalibrated, the ratio itself was meaningless before normalizing it to the ratio of output powers when no nonlinearity was present. To do this, the ratio was recorded across the f_{pm} spectrum and then repeated for an input power reduced by 30 dB. This second “zero-power” spectrum represents

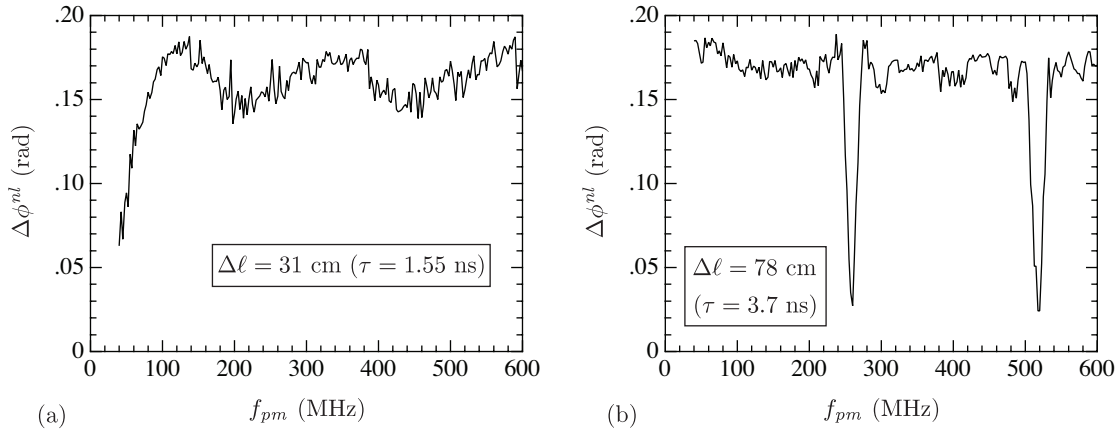


Figure 6.3: Nonlinear phase difference in folded NOLM vs./ phase modulation.

Using same parameters as Fig. 6.2 with $L_1 - L_2 = 0.75$. (a) $\Delta\phi^{nl}$ is reduced to nearly zero at $f_{pm} = 0$ when arm lengths are nearly matched ($\Delta\ell = 31$ cm). (b) Increasing $\Delta\ell$ to 78 cm allows us to observe higher-order $\Delta\phi^{nl}$ minima at multiples of $f_{pm} = 1/\tau$. In both plots, $f_{pm} < 40$ MHz is not shown because SBS precluded the measurement.

the ratio of port powers in the absence of any nonlinear effects. At each frequency data point, it was divided from the full-power data resulting in a value that equalled 1 when $\Delta\phi^{nl} = 0$, and therefore when no Sagnac switching was present. Any change in this normalized ratio represents a switching of power from one port to the other. Finally, $\Delta\phi^{nl}$ was calculated at each data point using the NOLM transfer function (2.2).

Figure 6.3(a) shows the results when $\Delta\ell = 31$ cm. $\Delta\phi^{nl}$ remains above 0.15 rad until f_{pm} is reduced below ≈ 100 MHz. As f_{pm} approaches zero, the nonlinear phase difference decreases dramatically. This result, which is not explained by existing theory, shows that the phase modulation of the input signal is also related to the disappearance of $\Delta\phi^{nl}$. In fact, we can demonstrate that the dependence of $\Delta\phi^{nl}$ on the phase modulation frequency f_{pm} and the mismatch $\Delta\ell$ are inter-related. In Fig. 6.3(b), $\Delta\ell$ is increased to 78 cm and we observe that $\Delta\phi^{nl}$ drops to zero at all integer multiples of $f_{pm} = 1/\tau$. It is assumed that a zero also exists at $f_{pm} = 0$, but it cannot be seen in our available frequency range.

From the empirical evidence of Figs. 6.2 and 6.3 (in addition to several experiments not presented) it became apparent that (1) $\Delta\phi^{nl}$ goes to zero at $f_{pm} = 0$, (2) a near-zero $\Delta\phi^{nl}$ exists in a finite range of frequencies above $f_{pm} = 0$, and (3) this frequency range increases as $\Delta\ell$ is reduced toward zero. This behavior is incompatible with the arm-matching requirement for amplitude stability discussed in Sect. 4.2, which requires that $\tau \ll 1/R_b$. When this requirement is achieved, $\Delta\phi^{nl}$ will be reduced to nearly zero across the frequency range of the communication

signal (zero to $\sim R_b$). If $\Delta\phi^{nl} = 0$, no gain equalization is possible. To summarize, the equal arm lengths required for amplitude stability cause the nonlinearity responsible for gain equalization to disappear.

To make headway towards understanding the physics behind these observations, we developed a detailed theory of the third-order nonlinear effects in a NOLM with a folded non-PM fiber, described in the following section. This analysis shows that a four-wave mixing process involving the four fields in the folded loop (forward- and backward-propagating cw and ccw fields) exactly counteracts the four Kerr phase shifts described in (4.5), but this effect is phase matched only under specific arm-mismatch and signal-modulation conditions. The resulting theory agrees with the observations shown in Figs. 6.2 and 6.3 and also allows us to introduce an elegant solution (Sect. 6.3) that allows the folded NOLM to operate with balanced arm lengths.

6.2 Nonlinear phase shifts in folded NOLMs, revisited

In Sect. 4.1.3 we listed the nonlinear phase shifts that co- and counter-propagating signals generate as a function of their relative SOPs. These phase shifts were used to determine the nonlinear phase difference $\Delta\phi^{nl}$ experienced in the folded loop. This analysis did not take into account the fact that the four fields (forward- and backward-propagating cw and ccw signals) in the folded loop were not independent. We now recognize that the backward-propagating fields have reflected from a Faraday rotator mirror (FRM) and therefore have a specific phase relationship to the forward-propagating fields.

To begin, we expand upon the methods of Clausen, et al. [86]. The analysis is very general in nature in Sects. 6.2.1–6.2.3, describing the interactions between four signals (2 SOPs \times 2 propagation directions) at each wavelength where a WDM channel resides. In Sect. 6.2.4, we introduce the FRM and the inherent relationship between the four signals is discussed—since all four signals originate from the same source, additional constraints are introduced that alter the resulting nonlinear phase shifts.

6.2.1 Expectation value method

In a linearly birefringent optical fiber, as applies to the fiber in our folded loop, the local fiber eigenstates are linearly polarized along two orthogonal axes $\hat{\mathbf{x}}$ and $\hat{\mathbf{y}}$ whose orientation in the

laboratory frame will vary along the fiber length.¹ We denote the slowly varying complex amplitudes of the x - and y -polarized electric fields as U^\pm and V^\pm , respectively, where \pm signifies the propagation direction. The total electric field at a given time t and location z along the fiber is thus

$$\begin{aligned} \mathbf{E}(z, t) = & \sum_{i=1}^N \left[U_i^+(z, t) e^{i(k_i z - \omega_i t)} \hat{\mathbf{x}} + U_i^{+*}(z, t) e^{-i(k_i z - \omega_i t)} \hat{\mathbf{x}} + \right. \\ & V_i^+(z, t) e^{i(l_i z - \omega_i t)} \hat{\mathbf{y}} + V_i^{+*}(z, t) e^{-i(l_i z - \omega_i t)} \hat{\mathbf{y}} + \\ & U_i^-(z, t) e^{i(-k_i z - \omega_i t)} \hat{\mathbf{x}} + U_i^{-*}(z, t) e^{-i(-k_i z - \omega_i t)} \hat{\mathbf{x}} + \\ & \left. V_i^-(z, t) e^{i(-l_i z - \omega_i t)} \hat{\mathbf{y}} + V_i^{-*}(z, t) e^{-i(-l_i z - \omega_i t)} \hat{\mathbf{y}} \right], \end{aligned} \quad (6.1)$$

where k and l are the propagation constants for the two linear eigenstates, ω_i is the optical radial frequency, and subscripts identify which of the N wavelength-division multiplexed (WDM) channels is represented.

The third-order nonlinear variation is given by the nonlinear Schrödinger equation: [110]

$$\frac{\partial \mathbf{E}}{\partial z} = i \frac{\chi}{3} (\mathbf{E} \cdot \mathbf{E}) \mathbf{E}, \quad (6.2)$$

where χ is the Kerr coefficient. Equation 6.1 is inserted into 6.2 and all rapidly oscillating terms are removed. If we assume sufficient dispersion to eliminate phase-matching between separate

¹The reader should not mistakenly equate a linearly birefringent fiber with a PM fiber. In this context, a linearly birefringent fiber is one whose local birefringence is predominantly linear in nature; i.e., the local eigenstates at any point in the fiber are orthogonal, linear SOPs. This accurately describes most common fibers because a slight core ellipticity provides a [small] linear birefringence. The birefringence axes are not fixed in these non-PM fibers, therefore both the magnitude and orientation of the linear birefringence rotates along the length of the fiber. Additionally, the birefringence magnitude is too weak to maintain a linear SOP when the fiber is bent or perturbed. This is precisely why a signal's polarization evolves randomly during propagation.

WDM channels, we are left with

$$\begin{aligned}
\frac{\partial}{\partial z} U_i^+ &= i\gamma \left(|U_i^+|^2 + \frac{2}{3} |V_i^+|^2 \right) U_i^+ + \gamma \frac{1}{3} U_i^{+*} V_i^+ V_i^+ e^{2i(l_i - k_i)z} \\
&\quad + i\gamma \sum_{j=1, j \neq i}^N \left[\left(2|U_j^+|^2 + \frac{2}{3} |V_j^+|^2 \right) U_i^+ \right. \\
&\quad \quad \left. + \frac{2}{3} V_j^{+*} U_j^+ V_i^+ e^{i(l_i - l_j + k_j - k_i)z} + \frac{2}{3} U_j^{+*} V_j^+ V_i^+ e^{i(l_i + l_j - k_j - k_i)z} \right] \\
&\quad + i\gamma \sum_{j=1}^N \left[\left(2|U_j^-|^2 + \frac{2}{3} |V_j^-|^2 \right) U_i^+ \right. \\
&\quad \quad \left. + \frac{2}{3} V_j^{-*} U_j^- V_i^+ e^{i(l_j + l_i - k_j - k_i)z} + \frac{2}{3} U_j^{-*} V_j^- V_i^+ e^{i(k_j - k_i + l_i - l_j)z} \right], \quad (6.3)
\end{aligned}$$

where $\gamma = \frac{2\pi n_2}{\lambda A_{\text{eff}}}$ is the fiber nonlinearity, n_2 is the nonlinear index of refraction and A_{eff} is the effective area. Similar expressions exist for $\partial U_i^- / \partial z$ and $\partial V_i^\pm / \partial z$. If the birefringence is large enough that $e^{i(l_i - k_i)z}$ oscillates rapidly over the fiber length, (6.3) may be simplified:

$$\begin{aligned}
\frac{\partial}{\partial z} U_i^+ &= i\gamma \left(|U_i^+|^2 + \frac{2}{3} |V_i^+|^2 \right) U_i^+ + i\gamma \left(2|U_i^-|^2 + \frac{2}{3} |V_i^-|^2 \right) U_i^+ + i\gamma \frac{2}{3} U_i^{-*} V_i^- V_i^+ \\
&\quad + i\gamma \sum_{j=1, j \neq i}^N \left(2|U_j^+|^2 + \frac{2}{3} |V_j^+|^2 + 2|U_j^-|^2 + \frac{2}{3} |V_j^-|^2 \right) U_i^+. \quad (6.4)
\end{aligned}$$

The first line on the right-hand side of this expression represents the effect on the x -polarized component of channel i due to self-phase modulation (first term), cross-phase modulation from the copropagating y -polarized field (second term), and cross-phase modulation from the counter-propagating channel i (last three terms). The following line represents the effects of cross-phase modulation of channel i due to the presence of all other channels j . A similar equation for V_i^+ is obtained by replacing U with V and l with k , and vice versa.

By representing the complex field amplitude at the i^{th} channel's wavelength as a vector $\mathbf{A}_i^\pm = [U_i^\pm, V_i^\pm]^T$, we can recast the nonlinear Schrödinger equation (6.4) and the complementary equation for $\frac{\partial V_i^+}{\partial z}$ in a matrix form:

$$\frac{\partial}{\partial z} \mathbf{A}_i^+ = i \left[\bar{n}_{i \rightarrow i}^+ (\mathbf{A}_i^+) + \bar{n}_{i \rightarrow i}^- (\mathbf{A}_i^-) + \sum_{j=1, j \neq i}^N \left(\bar{n}_{j \rightarrow i}^+ (\mathbf{A}_j^+) + \bar{n}_{j \rightarrow i}^- (\mathbf{A}_j^-) \right) \right] \mathbf{A}_i^+. \quad (6.5)$$

The matrix $\bar{n}_{i \rightarrow i}^+$ represents SPM and co-propagating orthogonal-SOP XPM of channel i and the matrix $\bar{n}_{i \rightarrow i}^-$ represents the XPM from the fields of the counter-propagating channel i . The cross-phase modulations induced by the forward- and backward-propagating fields from other

channels are represented by $\bar{n}_{j \rightarrow i}^+$ and $\bar{n}_{j \rightarrow i}^-$, respectively. These matrices are given by

$$\bar{n}_{i \rightarrow i}^+(\mathbf{A}_i^+) = \gamma \begin{bmatrix} |U_i^+|^2 + \frac{2}{3}|V_i^+|^2 & 0 \\ 0 & |V_i^+|^2 + \frac{2}{3}|U_i^+|^2 \end{bmatrix}, \quad (6.6a)$$

$$\bar{n}_{i \rightarrow i}^-(\mathbf{A}_i^-) = \gamma \begin{bmatrix} 2|U_i^-|^2 + \frac{2}{3}|V_i^-|^2 & \frac{2}{3}U_i^{-*}V_i^- \\ \frac{2}{3}V_i^{-*}U_i^- & 2|V_i^-|^2 + \frac{2}{3}|U_i^-|^2 \end{bmatrix}, \quad (6.6b)$$

$$\bar{n}_{j \rightarrow i}^+(\mathbf{A}_j^+) = \gamma \begin{bmatrix} 2|U_j^+|^2 + \frac{2}{3}|V_j^+|^2 & 0 \\ 0 & 2|V_j^+|^2 + \frac{2}{3}|U_j^+|^2 \end{bmatrix}, \quad (6.6c)$$

$$\bar{n}_{j \rightarrow i}^-(\mathbf{A}_j^-) = \gamma \begin{bmatrix} 2|U_j^-|^2 + \frac{2}{3}|V_j^-|^2 & 0 \\ 0 & 2|V_j^-|^2 + \frac{2}{3}|U_j^-|^2 \end{bmatrix}. \quad (6.6d)$$

We shall now separate the electric field into orthogonal states that, after propagation in the fiber coil, are separated by a PBS. Before examining a folded loop with an FRM, we first consider a length of non-PM fiber in which the four signals are combined and separated by a PBS at each end (Fig. 6.4). In this configuration, the field $\mathbf{B}_i^+ = [P_i^+, Q_i^+]^T$ enters through one port of PBS-1 and exits entirely through a single port of PBS-2. During its propagation, the SOP of \mathbf{B}_i^+ randomly evolves, but a polarization controller (see Fig. 6.4) is set such that the SOP is aligned correctly at PBS-2. Likewise, the field $\mathbf{C}_i^+ = [R_i^+, S_i^+]^T$ enters the opposite PBS-1 port; it is therefore orthogonal to \mathbf{B}_i^+ and will exit in an SOP orthogonal to that of \mathbf{B}_i^+ , i.e., at the second port of PBS-2. The field which follows the reverse path of \mathbf{B}_i^+ , injected at the top right port of PBS-2, is denoted $\mathbf{B}_i^- = [P_i^-, Q_i^-]^T$, likewise for $\mathbf{C}_i^- = [R_i^-, S_i^-]^T$, injected at the bottom right port of PBS-2. Just as with \mathbf{A}_i , the components P , Q , R , and S are defined in the basis of the fiber's local linear birefringence, whose orientation varies randomly along the fiber. The polarizations \mathbf{B}_i and \mathbf{C}_i are essentially *global* eigenstates of the system. For a given fiber, \mathbf{B}_i (or \mathbf{C}_i) is a specific elliptical SOP at each location in the fiber. Any photon at λ_i co-polarized with \mathbf{B}_i at any spot in the fiber will always exit an upper PBS port, whether it is traveling to the right or left.

At all points in the fiber, the total electric field is $\sum_i (\mathbf{A}_i^+ + \mathbf{A}_i^-)$, where

$$\mathbf{A}_i^\pm = \mathbf{B}_i^\pm + \mathbf{C}_i^\pm. \quad (6.7)$$

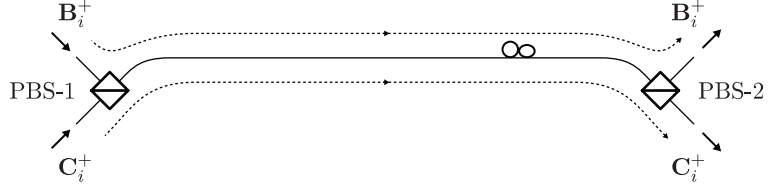


Figure 6.4: Bidirectional fiber with input/output polarizers.

A long fiber coil with a PBS at each end has a PC set such that photons entering the upper (lower) port of PBS-1 always exit the upper (lower) port of PBS-2, and vice-versa. The orthogonal states \mathbf{B}_i and \mathbf{C}_i (whose SOPs vary along the non-PM fiber coil) represent *global* eigenstates of the system.

Inserting (6.7) into (6.5) results in the nonlinear variation

$$\frac{\partial}{\partial z} (\mathbf{B}_i^+ + \mathbf{C}_i^+) = i \left[\bar{n}_{i \rightarrow i}^+ (\mathbf{B}_i^+, \mathbf{C}_i^+) + \bar{n}_{i \rightarrow i}^- (\mathbf{B}_i^-, \mathbf{C}_i^-) + \sum_{j=1, j \neq i}^N \left(\bar{n}_{j \rightarrow i}^+ (\mathbf{B}_j^+, \mathbf{C}_j^+) + \bar{n}_{j \rightarrow i}^- (\mathbf{B}_j^-, \mathbf{C}_j^-) \right) \right] (\mathbf{B}_i^+ + \mathbf{C}_i^+), \quad (6.8)$$

where the matrices $\bar{n}_{i,j \rightarrow i}^\pm$ may be determined by setting $U_i^\pm = P_i^\pm + R_i^\pm$ and $V_i^\pm = Q_i^\pm + S_i^\pm$ in Eqs. (6.6). We wish to find a solution of this nonlinear propagation equation of the form $\mathbf{B}_i^+(z) = \mathbf{B}_i^+(0) e^{iz\Phi_{\mathbf{B}^+}}$, where $\Phi_{\mathbf{B}^+}$ is the nonlinear phase shift per unit length experienced by \mathbf{B}_i^+ in the case of propagation through a long fiber with randomly varying birefringence. This solution is substituted into the left-hand side of (6.8) and both sides are multiplied by the conjugate transpose $\mathbf{B}_i^{+\dagger}$. After using the orthogonality requirement $\mathbf{B}_i^{+\dagger} \mathbf{C}_i^+ = 0$, we arrive at

$$\Phi_{\mathbf{B}^+} = \left\langle \frac{\mathbf{B}_i^{+\dagger} \bar{n} (\mathbf{B}_i^+ + \mathbf{C}_i^+)}{\mathbf{B}_i^{+\dagger} \mathbf{B}_i^+} \right\rangle, \quad (6.9)$$

where \bar{n} is the sum of all matrices in (6.8) and the brackets indicate averaging over all polarization states during propagation through a long fiber. A similar expression may be written for \mathbf{C}_i^+ after substituting the appropriate fields.

To facilitate averaging over all polarizations in (6.9), we use the Stokes parameters:

$$S_0(\mathbf{A}_i^\pm) = |U_i^\pm|^2 + |V_i^\pm|^2 = |\mathbf{A}_i^\pm|^2, \quad (6.10a)$$

$$S_1(\mathbf{A}_i^\pm) = |U_i^\pm|^2 - |V_i^\pm|^2, \quad (6.10b)$$

$$S_2(\mathbf{A}_i^\pm) = 2 \operatorname{Re} [U_i^{\pm*} V_i^\pm] = U_i^{\pm*} V_i^\pm + U_i^\pm V_i^{\pm*}, \quad (6.10c)$$

$$S_3(\mathbf{A}_i^\pm) = 2 \operatorname{Im} [U_i^{\pm*} V_i^\pm] = -i (U_i^{\pm*} V_i^\pm - U_i^\pm V_i^{\pm*}). \quad (6.10d)$$

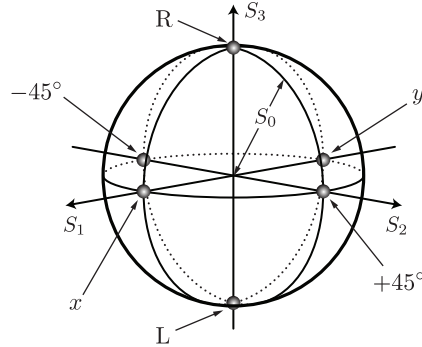


Figure 6.5: The Poincaré sphere.

Axes S_1 , S_2 , and S_3 designate degrees of linearity and circularity of SOP. Linear polarizations reside on the equator. Right- and left-circular states are the poles. The remaining surface area encompasses all elliptical states and the interior volume represents partially polarized signals.

With radius S_0 , the Poincaré sphere signifies all possible polarizations using the parameters $S_1 \rightarrow S_3$ as its three axes (Fig. 6.5). A point on the equator represents a linear polarization, the poles represent right- and left-circular polarizations, and elliptical states make up the remainder of the sphere's surface. Any point in the interior volume ($S_1^2 + S_2^2 + S_3^2 < S_0^2$) represents a partially polarized signal, with the center being a completely unpolarized signal. Orthogonally polarized co-propagating signals are diametrically opposed on the Poincaré sphere. Introducing the Stokes parameters allows us to visualize and quantify the integration implicit in the SOP averaging of (6.9) using spherical coordinates.

We are using the physical construct shown in Fig. 6.4 to clearly demonstrate the most general case of what happens when orthogonally polarized fields interact in a long fiber and are subsequently separated with polarizers. In a folded NOLM, PBS-2 is replaced by an FRM, which becomes the “source” of \mathbf{B}_i^- and \mathbf{C}_i^- since they are the reflections of \mathbf{C}_i^+ and \mathbf{B}_i^+ , respectively (note the change in SOP induced by the FRM). We begin in Sects. 6.2.2 and 6.2.3 by assuming the above four fields are generated by four distinct sources, as in Fig. 6.4. In Sect. 6.2.4 we show that the FRM introduces additional constraints on the analysis, which results in a different nonlinear behavior. By beginning with an analysis of the system shown in Fig. 6.4, we can elucidate how the FRM affects the system's performance.

In the following sections, the nonlinear phase difference in the folded NOLM will be calculated by observing that the fields \mathbf{B}_i^+ and \mathbf{C}_i^+ in Fig. 6.4 represent the cw and ccw beams, respectively, as they travel away from the PBS in the folded fiber loop. The total nonlinear phase shift $\Phi_{\mathbf{B}^+}$ in (6.9) may be rewritten as the sum of its constituent phase shifts, each from different SPM and XPM sources:

$$\Phi_{\mathbf{B}^+} = \Phi_{\mathbf{B}^+,i \rightarrow i}^+ + \Phi_{\mathbf{B}^+,i \rightarrow i}^- + \Phi_{\mathbf{B}^+,j \rightarrow i}^+ + \Phi_{\mathbf{B}^+,j \rightarrow i}^-, \quad (6.11)$$

where the four terms on the right-hand side are formed by replacing \bar{n} with the matrices in (6.6a), (6.6b), (6.6c), and (6.6d), respectively. From left to right, these four terms represent the nonlinear phase shifts experienced by \mathbf{B}_i^+ due to (1) the forward-propagating power of the i^{th} WDM channel (see Sect. 6.2.2), (2) the backward-propagating power of the i^{th} WDM channel (see Sect. 6.2.3), and (3) the forward- and (4) backward-propagating power of all other WDM channels (see Sect. 6.2.6). A similar expression exists for $\Phi_{\mathbf{C}^+}$.

The nonlinear phase difference $\Delta\phi^{nl}$, which is utilized for gain equalization, is determined by subtracting the total phase shifts experienced by the cw and ccw beams and multiplying by the effective nonlinear interaction length of the fiber coil:

$$\Delta\phi^{nl} = (\Phi_{\mathbf{B}^+} - \Phi_{\mathbf{C}^+}) \ell'_{eff}, \quad (6.12)$$

where we have assumed that equal phase shifts are accrued by the cw and ccw beams on the return trip from the FRM to the PBS and ℓ'_{eff} accounts for the total interaction length of the double-passed fiber coil.

6.2.2 SPM and orthogonal, co-propagating XPM

To determine the nonlinear phase shift of \mathbf{B}_i^+ as a function of both its own power and the power of \mathbf{C}_i^+ in a randomly birefringent fiber, we must solve (6.9) with \bar{n} replaced by $\bar{n}_{i \rightarrow i}^+(\mathbf{B}_i^+, \mathbf{C}_i^+)$:

$$\begin{aligned} \Phi_{\mathbf{B}^+, i \rightarrow i}^+ = \frac{\gamma}{|\mathbf{B}_i^+|^2} \left\langle & |P_i^+|^4 + \frac{4}{3}|P_i^+|^2|Q_i^+|^2 + |Q_i^+|^4 + \frac{4}{3}|P_i^+|^2|R_i^+|^2 + \frac{2}{3}|P_i^+|^2|S_i^+|^2 \right. \\ & \left. + \frac{4}{3}|Q_i^+|^2|S_i^+|^2 + \frac{2}{3}|Q_i^+|^2|R_i^+|^2 + \xi(\mathbf{B}_i^+, \mathbf{C}_i^+) \right\rangle. \quad (6.13) \end{aligned}$$

After simplifying by using the orthogonality condition $\mathbf{B}_i^+ \cdot \mathbf{C}_i^{+*} = 0$, it can be shown that the last term is

$$\begin{aligned} \xi(\mathbf{B}_i^+, \mathbf{C}_i^+) = \frac{1}{3} \left(|P_i^+|^2 - |Q_i^+|^2 \right) (P_i^+ R_i^{+*} + P_i^{+*} R_i^+) + \frac{2}{3} P_i^{+*2} R_i^{+2} \\ + \frac{1}{3} P_i^{+*} R_i^+ \left(|P_i^+|^2 - |Q_i^+|^2 + |R_i^+|^2 - |S_i^+|^2 \right). \quad (6.14) \end{aligned}$$

Equation (6.13) may be simplified using the Stokes parameters for \mathbf{B}_i^+ and \mathbf{C}_i^+ , which are defined as in (6.10) but with U and V replaced with either P and Q or R and S , respectively. Because of the signals' orthogonality, we make use of the fact that $\frac{s_1(\mathbf{B}_i^+)}{s_0(\mathbf{B}_i^+)} = -\frac{s_1(\mathbf{C}_i^+)}{s_0(\mathbf{C}_i^+)}$ and after

straightforward, fairly extensive algebra, we arrive at

$$\Phi_{\mathbf{B}^+, i \rightarrow i}^+ = \gamma \left[S_0(\mathbf{B}_i^+) \left\langle \frac{5}{6} + \frac{1}{6} \frac{S_1(\mathbf{B}_i^+)^2}{S_0(\mathbf{B}_i^+)^2} \right\rangle + S_0(\mathbf{C}_i^+) \left\langle 1 - \frac{1}{3} \frac{S_1(\mathbf{B}_i^+)^2}{S_0(\mathbf{B}_i^+)^2} \right\rangle + \langle \xi(\mathbf{B}_i^+, \mathbf{C}_i^+) \rangle \right]. \quad (6.15)$$

In spherical polar coordinates, $\frac{S_1}{S_0} = \sin \psi$, where ψ is an elevation angle measured from the S_2 - S_3 plane.² Letting the signal evolve through all possible SOPs is equivalent to replacing the angle brackets with the integral $\int_{-\pi/2}^{\pi/2} 2\pi \cos \psi d\psi$, resulting in

$$\Phi_{\mathbf{B}^+, i \rightarrow i}^+ = \frac{8}{9} \gamma \left(|\mathbf{B}_i^+|^2 + |\mathbf{C}_i^+|^2 \right) + \gamma \langle \xi(\mathbf{B}_i^+, \mathbf{C}_i^+) \rangle, \quad (6.16)$$

where $|\mathbf{B}_i^+|^2$ is the optical power of \mathbf{B}_i^+ .

There are several approaches for evaluating the $\langle \xi \rangle$ term. While perhaps not the most elegant mathematically, the approach we use is simple and effective and will also be a useful starting point for analysis in later sections. We begin by reducing the fields to their simplest components by defining

$$\mathbf{B}_i^+ \equiv \begin{pmatrix} P_i^+ \\ Q_i^+ \end{pmatrix} \equiv e^{i\alpha} \begin{pmatrix} |P_i^+| e^{-i\theta} \\ |Q_i^+| e^{+i\theta} \end{pmatrix}, \quad (6.17a)$$

$$\mathbf{C}_i^+ \equiv \begin{pmatrix} R_i^+ \\ S_i^+ \end{pmatrix} \equiv e^{i\beta} \begin{pmatrix} |R_i^+| e^{-i\phi} \\ |S_i^+| e^{+i\phi} \end{pmatrix}, \quad (6.17b)$$

where the fields $(1, 0)^T$ and $(0, 1)^T$ represent the local eigenstates of the linearly birefringent fiber. By restricting θ and ϕ to both be between zero and π , the optical phase is contained only in the exponential factors that precede the Jones vector on the right-hand side of (6.17). Additionally, since the two signals are orthogonal, we require $(\theta - \phi) = \pm\pi/2$.

Though not used until Sect. 6.2.3, we also write the counter-propagating states as

$$\mathbf{B}_i^- \equiv \begin{pmatrix} P_i^- \\ Q_i^- \end{pmatrix} \equiv e^{i\delta} \begin{pmatrix} |P_i^-| e^{+i\theta} \\ |Q_i^-| e^{-i\theta} \end{pmatrix}, \quad (6.18a)$$

$$\mathbf{C}_i^- \equiv \begin{pmatrix} R_i^- \\ S_i^- \end{pmatrix} \equiv e^{i\epsilon} \begin{pmatrix} |R_i^-| e^{+i\phi} \\ |S_i^-| e^{-i\phi} \end{pmatrix}, \quad (6.18b)$$

where the sign changes of θ and ϕ are required to maintain the co-polarized nature of the counter-propagating fields.

²Note that, unlike typical convention, to simplify the integration we are defining the ‘‘north pole’’ of our spherical coordinates to be the point $S_1 = S_0$.

Let's now examine one of the terms in (6.14). Using (6.17), it can be shown that

$$\left\langle \frac{2}{3} P_i^{+*2} R_i^{+2} \right\rangle = \left\langle -\frac{2}{3} |P_i^+|^2 |R_i^+|^2 e^{i2(\beta-\alpha)} \right\rangle, \quad (6.19)$$

where the negative sign on the right-hand side is a result of the orthogonality condition $(\theta - \phi) = \pm\pi/2$. Equation (6.19) can be shown to equal zero when one considers the physical meaning of the SOP averaging implied by the brackets $\langle \cdot \rangle$. While propagating down a long fiber with an intrinsic linear birefringence that varies randomly along its length, the SOP of an input signal will randomly walk around the Poincaré sphere. Two orthogonally polarized signals will accumulate different phase shifts since they follow different optical paths. The phase difference $(\beta - \alpha)$ will, therefore, randomly vary along the fiber length even though the two signals are propagating down the same fiber. Thus, the exponential term in (6.19) will average to zero.

The random nature of $(\beta - \alpha)$ can be visualized by considering that at a certain location in the fiber, the two signals \mathbf{B}_i^+ and \mathbf{C}_i^+ may coincide with the local polarization eigenstates. Since the degree of linear birefringence is random (in addition to its orientation), \mathbf{B}_i^+ and \mathbf{C}_i^+ will exit this section of fiber with a random phase difference. A similar description is utilized by the authors of [66] when considering a non-PM fiber to be composed of many concatenated short lengths of birefringent fiber whose relative orientations are random.

The rest of the terms in ξ can be shown to have similar exponential factors and will therefore average to zero in the same manner as above. Thus, $\xi = 0$ and (6.16) reduces to

$$\Phi_{\mathbf{B}^+, i \rightarrow i}^+ = \frac{8}{9} \gamma \left(|\mathbf{B}_i^+|^2 + |\mathbf{C}_i^+|^2 \right). \quad (6.20)$$

This result is identical to the SPM magnitude in non-PM fiber that is commonly quoted in the literature [64–66]. From the symmetry of the system, one can substitute \mathbf{B}_i^+ for \mathbf{C}_i^+ (and vice versa) to find the nonlinear phase shift induced upon \mathbf{C}_i^+ :

$$\Phi_{\mathbf{C}^+, i \rightarrow i}^+ = \Phi_{\mathbf{B}^+, i \rightarrow i}^+. \quad (6.21)$$

Equation 6.21 states that the nonlinear phase shifts imposed upon \mathbf{B}_i^+ and \mathbf{C}_i^+ from forward-propagating optical fields (i.e., SPM and co-propagating orthogonal-SOP XPM) are equal, even when a power imbalance $|\mathbf{B}_i^+|^2 \neq |\mathbf{C}_i^+|^2$ exists. Therefore, these terms cannot provide a nonlinear phase difference $\Delta\phi^{nl}$ between the cw and ccw signals, which implies that the nonlinear transfer function of the folded NOLM with balanced arms has no dependence on instantaneous power. The only source of $\Delta\phi^{nl}$ lies in the interactions between counter-propagating signals, which is explored in the next section.

6.2.3 Counter-propagating XPM

To determine the nonlinear phase shift of \mathbf{B}_i^+ as a function of the counter-propagating signals \mathbf{B}_i^- and \mathbf{C}_i^- in a non-PM fiber, we must solve (6.9) with \bar{n} replaced by $\bar{n}_{i \rightarrow i}^-(\mathbf{B}_i^-, \mathbf{C}_i^-)$. The overall approach is similar to that used in Sect. 6.2.2. After regrouping the resulting terms, we are left with

$$\Phi_{\mathbf{B}^+, i \rightarrow i}^- = \frac{\gamma}{|\mathbf{B}_i^+|^2} \langle A_1(\mathbf{B}_i^+, \mathbf{B}_i^-) + A_2(\mathbf{B}_i^+, \mathbf{C}_i^-) + \zeta(\mathbf{B}_i^+, \mathbf{C}_i^+, \mathbf{B}_i^-, \mathbf{C}_i^-) \rangle, \quad (6.22)$$

where

$$\begin{aligned} A_1(\mathbf{B}_i^+, \mathbf{B}_i^-) &= 2|P_i^+|^2|P_i^-|^2 + \frac{2}{3}|P_i^+|^2|Q_i^-|^2 + \frac{2}{3}|Q_i^+|^2|P_i^-|^2 + 2|Q_i^+|^2|Q_i^-|^2 \\ &\quad + \frac{2}{3}P_i^-*P_i^+*Q_i^+Q_i^- + \frac{2}{3}P_i^-P_i^+Q_i^{+*}Q_i^{-*}, \end{aligned} \quad (6.23)$$

$$\begin{aligned} A_2(\mathbf{B}_i^+, \mathbf{C}_i^-) &= 2|P_i^+|^2|R_i^-|^2 + \frac{2}{3}|P_i^+|^2|S_i^-|^2 + \frac{2}{3}|Q_i^+|^2|R_i^-|^2 + 2|Q_i^+|^2|S_i^-|^2 \\ &\quad + \frac{2}{3}R_i^-*P_i^+*Q_i^+S_i^- + \frac{2}{3}R_i^-P_i^+Q_i^{+*}S_i^{-*}, \end{aligned} \quad (6.24)$$

and the many terms contained in ζ are listed in Appendix B.

Equation (6.23) may be simplified using the Stokes parameters for \mathbf{B}_i^\pm , which are defined as in (6.10) but with U^\pm and V^\pm replaced with P^\pm and Q^\pm , respectively. It can be shown after some algebra that

$$\begin{aligned} \frac{\gamma}{|\mathbf{B}_i^+|^2} \langle A_1 \rangle &= \frac{\gamma}{S_0(\mathbf{B}_i^+)} \left\langle \frac{4}{3}S_0(\mathbf{B}_i^+)S_0(\mathbf{B}_i^-) + \frac{2}{3}S_1(\mathbf{B}_i^+)S_1(\mathbf{B}_i^-) \right. \\ &\quad \left. + \frac{1}{3}S_2(\mathbf{B}_i^+)S_2(\mathbf{B}_i^-) - \frac{1}{3}S_3(\mathbf{B}_i^+)S_3(\mathbf{B}_i^-) \right\rangle. \end{aligned} \quad (6.25)$$

To recast (6.25) in spherical coordinates, we can write $\frac{S_1(\mathbf{B}_i^+)}{S_0(\mathbf{B}_i^+)} = \frac{S_1(\mathbf{B}_i^-)}{S_0(\mathbf{B}_i^-)} = \sin \psi$, $\frac{S_2(\mathbf{B}_i^+)}{S_0(\mathbf{B}_i^+)} = \frac{S_2(\mathbf{B}_i^-)}{S_0(\mathbf{B}_i^-)} = \cos \psi \cdot \cos \theta$, and $\frac{S_3(\mathbf{B}_i^+)}{S_0(\mathbf{B}_i^+)} = -\frac{S_3(\mathbf{B}_i^-)}{S_0(\mathbf{B}_i^-)} = \cos \psi \cdot \sin \theta$, where ψ is an elevation angle from the S_2 - S_3 plane and θ is an azimuthal angle around S_1 . Notice the sign change present for S_3 . This is necessary because copolarized, counter-propagating signals have S_3 parameters of opposite sign. After equating the SOP averaging to an integral across the surface of the Poincaré sphere, (6.25) becomes

$$\begin{aligned} \frac{\gamma}{|\mathbf{B}_i^+|^2} \langle A_1 \rangle &= \gamma \frac{|\mathbf{B}_i^-|^2}{4\pi} \int_0^{2\pi} \int_{-\pi/2}^{\pi/2} \left(\frac{5}{3} + \frac{1}{3} \sin^2 \psi \right) \cos \psi \, d\psi \, d\theta \\ &= \frac{16}{9} \gamma |\mathbf{B}_i^-|^2. \end{aligned} \quad (6.26)$$

The Kerr phase shift induced by \mathbf{C}_i^- is easily inferred by comparing (6.23) and (6.24) and realizing that one can simply make the substitution $\mathbf{B}_i^- \rightarrow \mathbf{C}_i^-$ in (6.25). Since the signals remain orthogonally polarized, we may use the relations $\frac{S_1(\mathbf{B}_i^+)}{S_0(\mathbf{B}_i^+)} = -\frac{S_1(\mathbf{C}_i^-)}{S_0(\mathbf{C}_i^-)} = \sin \psi$, $\frac{S_2(\mathbf{B}_i^+)}{S_0(\mathbf{B}_i^+)} = \cos \psi \cdot \cos \theta$, and $\frac{S_3(\mathbf{B}_i^+)}{S_0(\mathbf{B}_i^+)} = \frac{S_3(\mathbf{C}_i^-)}{S_0(\mathbf{C}_i^-)} = \cos \psi \cdot \sin \theta$. Finally, we arrive at

$$\begin{aligned} \frac{\gamma}{|\mathbf{B}_i^+|^2} \langle A_2 \rangle &= \gamma \frac{|\mathbf{C}_i^-|^2}{4\pi} \int_0^{2\pi} \int_{-\pi/2}^{\pi/2} \left(1 - \frac{1}{3} \sin^2 \psi\right) \cos \psi \, d\psi \, d\theta \\ &= \frac{8}{9} \gamma |\mathbf{C}_i^-|^2. \end{aligned} \quad (6.27)$$

If the terms of ζ (see Appendix B) are expanded using the field components (6.17) and (6.18), it can be shown that every term has one of the following exponential factors: $e^{i(\alpha-\beta)}$, $e^{i(\delta-\epsilon)}$, $e^{i(\alpha-\beta-\delta+\epsilon)}$, or $e^{i(\alpha-\beta+\delta-\epsilon)}$. Just as in Sect. 6.2.2, the quantities $(\alpha-\beta)$ and $(\delta-\epsilon)$ are randomly varying during propagation in a non-PM fiber. Additionally, in the setup shown in Fig. 6.4 where the four signals originate from different sources, there is no fixed relationship between the four phases α , β , δ , and ϵ and any combination of these phases will vary randomly along the fiber.³ Therefore, the exponential factors will cause ζ to average to zero during propagation. We are left with

$$\Phi_{\mathbf{B}^+, i \rightarrow i}^- = \frac{16}{9} \gamma |\mathbf{B}_i^-|^2 + \frac{8}{9} \gamma |\mathbf{C}_i^-|^2, \quad (6.28)$$

which is identical to the values introduced in Table 4.1 for counter-propagating XPM in a non-PM fiber. A similar expression for $\Phi_{\mathbf{C}^+, i \rightarrow i}^-$ may be obtained by swapping \mathbf{B}_i^- and \mathbf{C}_i^- .

Before examining the specific case of a folded NOLM with balanced arm lengths (Sect. 6.2.4), let's first summarize the current results. If we neglect the phase shifts from other WDM channels (i.e., the last term on the right-hand side of Eq. 6.11), the nonlinear phase shifts acting on \mathbf{B}_i^+ are

$$\Phi_{\mathbf{B}^+, i \rightarrow i}^\pm = \frac{8}{9} \gamma |\mathbf{B}_i^+|^2 + \frac{8}{9} \gamma |\mathbf{C}_i^+|^2 + \frac{16}{9} \gamma |\mathbf{B}_i^-|^2 + \frac{8}{9} \gamma |\mathbf{C}_i^-|^2, \quad (6.29)$$

where the four nonlinear terms are from (6.20) and (6.28). The corresponding expression for the orthogonal field is

$$\Phi_{\mathbf{C}^+, i \rightarrow i}^\pm = \frac{8}{9} \gamma |\mathbf{C}_i^+|^2 + \frac{8}{9} \gamma |\mathbf{B}_i^+|^2 + \frac{16}{9} \gamma |\mathbf{C}_i^-|^2 + \frac{8}{9} \gamma |\mathbf{B}_i^-|^2. \quad (6.30)$$

The four terms on the right-hand sides of (6.29) and (6.30) represent the nonlinear phase shifts

³This statement can be violated if the four sources have coherence lengths exceeding the fiber length. In this case, the quantity $(\alpha-\beta+\delta-\epsilon)$ may have a fixed value during one round trip. Of course, when the phase of any source changes, whether from the finite coherence time or a perturbation after the source, the value will change and the exponential terms will again average to zero over time scales longer than the coherence time. In this publication, we are interested only in the special case that uses an FRM to generate the backward-propagating fields (Sect. 6.2.4). In this situation, it will be shown that the source coherence does *not* need to be maintained along the entire fiber coil for $(\alpha-\beta+\delta-\epsilon)$ to have a fixed value. However, we will discuss the relationship between the source coherence length and the arm mismatch $\Delta\ell$ in a fiber coil that is terminated with an FRM.

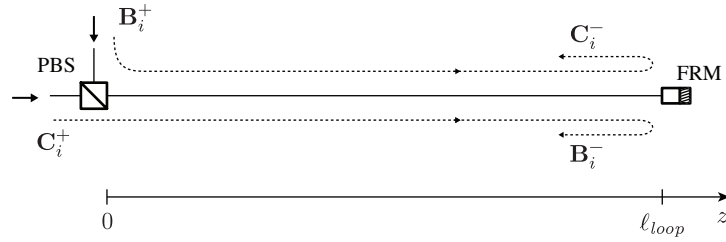


Figure 6.6: Folded fiber loop.

Signals are combined by a PBS in orthogonal SOPs. After propagating down a non-PM fiber, an FRM reflects the two signals into their orthogonal states causing them to exit the opposite PBS ports from which they entered.

from SPM, co-propagating orthogonal-SOP XPM, counter-propagating same-SOP XPM, and counter-propagating orthogonal-SOP XPM, respectively. We will discuss the effects of other WDM channels in Sect. 6.2.6.

In a NOLM, it is the nonlinear phase difference that is of importance. Subtracting (6.30) from (6.29) clearly shows that $\Delta\phi^{nl}$ (6.12) is only a function of the counter-propagating power:

$$\Delta\phi^{nl} = \frac{8}{9}\gamma \langle |\mathbf{B}_i^-|^2 - |\mathbf{C}_i^-|^2 \rangle \ell'_{eff}, \quad (6.31)$$

where the angle brackets denote that the effect scales with average power, as discussed in Sect. 4.2. It is the difference between the $\frac{8}{9}$ and $\frac{16}{9}$ factors in the counter-propagating XPM phase shifts (6.28) that generates a non-zero $\Delta\phi^{nl}$ and allows for gain equalization. The reader should recall that this result assumes no interactions between WDM channels i and j . These interactions are discussed in Sect. 6.2.6.

The phase shifts calculated up to this point have been previously published (as discussed in Chapter 4), though perhaps not available in their entirety in any *single* reference since most authors were not concerned with both the co- and counter-propagating Kerr phase shifts from both the co- and orthogonally polarized states simultaneously. The advancement to this theory that we are presenting in this dissertation begins with the next section, where we introduce additional requirements dictated by the presence of the FRM and the matched arm lengths.

6.2.4 Folded loop with balanced arms

We now extend the analysis of Sect. 6.2.3 to the special case of the folded loop, in which a Faraday-rotator mirror is the source of the backward-propagating fields. The folded configuration is shown in Fig. 6.6. The signals \mathbf{B}_i^+ and \mathbf{C}_i^+ originate from the cw and ccw beams, respectively.

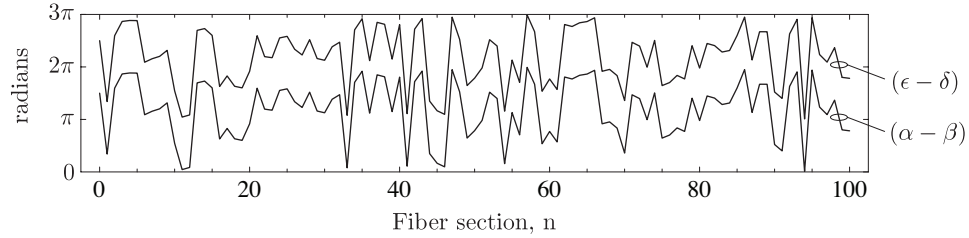


Figure 6.7: Numerical simulation of 100 concatenated fiber sections.

Equation (6.32) is graphically demonstrated by simulating sections of fiber separated by random rotations around the Poincaré sphere. After $n = 100$, the fiber is terminated by an FRM. The evolutions of $(\alpha - \beta)$ and $(\epsilon - \delta)$ are identical with a π phase shift induced by the FRM.

As described in Chapter 4, after double-passing the fiber loop, each signal exits the opposite PBS port from which it entered.

Let's consider the phases of the two signals as they enter the folded fiber loop ($z = 0$) as defined in (6.17). The signals originate from the same source, but travel through different NOLM arms. Let's assume $\ell_1 = \ell_2 \pm \mathcal{O}(\lambda)$, i.e., the arm lengths are nearly identical but not controlled at a wavelength scale. When they are combined by the PBS, the two signals will therefore have an unknown phase difference $(\alpha - \beta) = K(0)$. As they travel down the folded fiber, the phase difference follows a random evolution $K(z)$ until the FRM is reached, where $(\alpha - \beta) = K(\ell_{loop})$.

As discussed in Sect. 4.1.2, the FRM maintains the phase difference between the two signals, with the addition of a π phase shift. Minding the change in SOP, and assuming no time-dependent variation in birefringence, upon reflection the phases of the backward-propagating signals (6.18) therefore satisfy $(\epsilon - \delta)|_{z=\ell_{loop}} = K(\ell_{loop}) \pm \pi$. Additionally, the presence of an arbitrary birefringence profile preceding the FRM has no effect on its performance [83]. This has an important consequence on the relative phases of the four signals in a folded loop: it implies that $(\epsilon - \delta) = K(z) \pm \pi$ throughout the fiber. Therefore,

$$\alpha - \beta + \delta - \epsilon = \pm\pi \quad \text{for} \quad 0 \leq z \leq \ell_{loop} \quad (6.32)$$

in a folded fiber loop. This is presented graphically in Fig. 6.7 using a numerical simulation of 100 concatenated sections of fiber separated by random SOP rotations, similar to the analysis presented in [66]. Between each fiber section, a random polarization rotation is defined along with the corresponding rotation in the reverse direction. We simulate the transmission of two orthogonal signals in the forward direction, followed by the reverse after they reflect off an FRM, and record the values of α , β , δ , and ϵ in each fiber section. The phase difference $(\alpha - \beta)$ varies randomly along the fiber, while $(\epsilon - \delta)$ follows the same evolution in the reverse direction with

an additional π phase shift.⁴ This simulation clearly shows that the phase differences $(\alpha - \beta)$ and $(\delta - \epsilon)$ are separated by π at all locations in the fiber and, therefore, (6.32) is satisfied.

Using Eqs. 6.17 and 6.18, the last six terms of (B.1) in Appendix B,

$$\begin{aligned} \zeta_1 = & 2P_i^{-*}P_i^{+*}R_i^-R_i^+ + \frac{2}{3}Q_i^{-*}Q_i^{+*}R_i^-R_i^+ + \frac{2}{3}P_i^{+*}Q_i^{-*}R_i^+S_i^- \\ & + \frac{2}{3}P_i^{-*}Q_i^{+*}R_i^-S_i^+ + \frac{2}{3}P_i^{-*}P_i^{+*}S_i^-S_i^+ + 2Q_i^{-*}Q_i^{+*}S_i^-S_i^+, \end{aligned} \quad (6.33)$$

are expanded into

$$\begin{aligned} \zeta_1 = & \left(2|P_i^-||P_i^+||R_i^-||R_i^+| + \frac{2}{3}|Q_i^-||Q_i^+||R_i^-||R_i^+| \right. \\ & + \frac{2}{3}|P_i^+||Q_i^-||R_i^+||S_i^-|e^{2i(\theta-\phi)} + \frac{2}{3}|P_i^-||Q_i^+||R_i^-||S_i^+|e^{2i(\phi-\theta)} \\ & \left. + \frac{2}{3}|P_i^-||P_i^+||S_i^-||S_i^+| + 2|Q_i^-||Q_i^+||S_i^-||S_i^+| \right) e^{-i(\alpha-\beta+\delta-\epsilon)}, \end{aligned} \quad (6.34)$$

The orthogonality condition $\mathbf{B}_i^{\pm*} \cdot \mathbf{C}_i^{\pm} = 0$ gives us $2(\theta - \phi) = \pm\pi$ and $|Q_i^{\pm}||S_i^{\pm}| = |P_i^{\pm}||R_i^{\pm}|$, which along with (6.32) allows us to write

$$\zeta_1 = -\frac{8}{3}|P_i^+||P_i^-||R_i^+||R_i^-| - \frac{2}{3}|Q_i^+||Q_i^-||R_i^+||R_i^-| - \frac{2}{3}|P_i^+||P_i^-||S_i^+||S_i^-|. \quad (6.35)$$

To recast (6.35) in spherical coordinates, we utilize two identities derived from (6.10), $|U| = \sqrt{(S_0 + S_1)/2}$ and $|V| = \sqrt{(S_0 - S_1)/2}$, in addition to the polarization relationships

$$\frac{S_1(\mathbf{B}_i^+)}{S_0(\mathbf{B}_i^+)} = \frac{S_1(\mathbf{B}_i^-)}{S_0(\mathbf{B}_i^-)} = -\frac{S_1(\mathbf{C}_i^+)}{S_0(\mathbf{C}_i^+)} = -\frac{S_1(\mathbf{C}_i^-)}{S_0(\mathbf{C}_i^-)} = \sin \psi. \quad (6.36)$$

After much algebra, it can be shown that

$$\zeta_1 = \left(\frac{1}{3} \sin^2 \psi - 1 \right) |\mathbf{B}_i^+||\mathbf{B}_i^-||\mathbf{C}_i^+||\mathbf{C}_i^-|. \quad (6.37)$$

Since the modes \mathbf{B}_i^- and \mathbf{C}_i^- are the Faraday reflections of \mathbf{C}_i^+ and \mathbf{B}_i^+ , respectively, we can set $|\mathbf{C}_i^{\pm}| = |\mathbf{B}_i^{\mp}|$.⁵ After making these substitutions and comparing (6.37) with the integrand of (6.27), the inclusion of ζ_1 in (6.22) results in

$$\Phi_{\mathbf{B}^+, i \rightarrow i}^- = \frac{16}{9}\gamma |\mathbf{B}_i^-|^2 + \frac{8}{9}\gamma |\mathbf{C}_i^-|^2 - \frac{8}{9}\gamma |\mathbf{B}_i^+|^2, \quad (6.38)$$

⁴Since the computer model calculates the phase differences modulo 2π , we have taken the liberty of shifting the $(\epsilon - \delta)$ values by 2π when necessary to make the plots clearer.

⁵This neglects fiber and FRM attenuation, which may be accounted for with the folded-loop effective length parameter ℓ'_{eff} .

where the first two terms on the right-hand side are from (6.28) and the third one from (6.37).

While each of the four nonlinear phase shifts in (6.20) and (6.28) are the result of interactions between \mathbf{B}_i^+ and either itself or one of the other three fields, it is obvious from (6.37) that ζ_1 describes a four-wave mixing process between all four fields. Because of the particular phase-matching relationships in a loop that is folded with an FRM, the net result presents itself as another Kerr nonlinear phase shift. Combining (6.20) and (6.38), we find that the total nonlinear phase shift induced by WDM channel i onto itself in a folded NOLM with balanced arm lengths is

$$\Phi_{\mathbf{B}^+,i \rightarrow i} = \Phi_{\mathbf{B}^+,i \rightarrow i}^+ + \Phi_{\mathbf{B}^+,i \rightarrow i}^- = \frac{8}{9}\gamma \left(|\mathbf{B}_i^+|^2 + |\mathbf{C}_i^+|^2 + |\mathbf{B}_i^-|^2 + |\mathbf{C}_i^-|^2 \right) \quad (6.39)$$

The important consequence of this equation is that *if there is phase matching*, the “fifth” nonlinear phase shift (from ζ_1) exactly removes the imbalance between the counter-propagating XPM terms, leaving all four terms with the same magnitude. By swapping $\mathbf{B} \leftrightarrow \mathbf{C}$ in (6.39), a similar equation may be obtained for \mathbf{C}_i^+ . Without an imbalance in the magnitudes of the nonlinear phase shifts, the phase difference between the cw and ccw signals is $\Delta\phi^{nl} = (\Phi_{\mathbf{B}^+,i \rightarrow i} - \Phi_{\mathbf{C}^+,i \rightarrow i}) \ell'_{eff} = 0$.⁶

In Fig. 6.2, we experimentally demonstrated that the nonlinear phase difference $\Delta\phi^{nl}$ disappears when the folded NOLM has arms with nearly identical lengths ($\Delta\ell = 2$ cm in this example). As predicted by the model described in this chapter, this is caused by the phase matching of the four fields in the folded loop at each wavelength (cw and ccw signals, both forward- and backward-propagating), which allows the “fifth” nonlinear phase shift to be formed by the four-wave mixing terms ζ_1 . This phenomenon can only be modeled by considering the nonlinear interactions when all four fields are simultaneously present in the folded loop, and when their sources and phases are considered (i.e., all four fields originate from the same laser source and two are FRM reflections).

Figure 6.2 also showed a folded NOLM with a larger arm length mismatch ($\Delta\ell = 31$ cm) in which $\Delta\phi^{nl} \neq 0$. In the next section, we introduce both a non-zero arm length mismatch $\Delta\ell$ and the input signal’s phase modulation to our model in order to predict this result.

6.2.5 Folded loop with unbalanced arms

Let’s consider the specific case of a signal that is sinusoidally phase-modulated at f_{pm} with amplitude ϕ_0 , as is applicable in our experiment (see Fig. 6.1).⁷ Because of the arm length mismatch $\Delta\ell$, this modulation results in a time-varying phase difference between cw and ccw

⁶It has been assumed that the same phase shifts occur to the cw and ccw signals during their reverse path in the folded loop; the total nonlinear interaction length is accounted for in ℓ'_{eff} .

⁷As a reminder, this modulation was applied in order to suppress SBS.

signals upon entering the folded loop

$$\Delta\phi(t) = 2\phi_0 \sin(\pi f_{pm}\tau) \sin(2\pi f_{pm}t), \quad (6.40)$$

where $\tau = \Delta\ell/v$ is the time delay between the NOLM arms. $\Delta\phi(t)$ will cause the phase differences $(\alpha - \beta)$ and $(\epsilon - \delta)$ to vary in time, and therefore also along z . When a pair of photons enter the PBS from arms 1 and 2, they interact with each other and with the backward-propagating fields throughout the length of the folded fiber. When the parameter $(\alpha - \beta + \delta - \epsilon)$ oscillates with a large enough maximum excursion, the exponential term in (6.34) will average to zero over many cycles along the length of the folded fiber. This eliminates the effects of ζ_1 and restores the imbalance between the four nonlinear phase shifts, thereby generating the nonlinear phase difference required for gain equalization.

This combination of arm length mismatch and source phase modulation is precisely what allowed $\Delta\phi^{nl}$ to be non-zero in Fig. 6.2 when $\Delta\ell = 31$ cm. With this realization, we now understand that a relative phase modulation must exist between the co-propagating cw and ccw fields in the folded fiber loop in order for a non-zero $\Delta\phi^{nl}$ to be present, thereby making gain equalization possible. To avoid the nonlinear amplitude instability discussed in Sect. 4.2, we must make the arm mismatch as small as possible. Unfortunately, as $\Delta\ell$ (and τ) goes to zero, the relative phase modulation (6.40) also goes to zero. In Sect. 6.3 we present an engineering solution to this problem and demonstrate how a folded NOLM with balanced arms can still have a non-zero $\Delta\phi^{nl}$.

When $f_{pm}\tau = 0, 1, 2, \dots$, the arm mismatch and PM frequency are synchronized such that $\Delta\phi(t) = 0$ in the folded loop. Therefore, the ‘‘fifth’’ nonlinear term exists as shown above and $\Delta\phi^{nl}$ approaches zero as demonstrated experimentally in Fig. 6.3.

It is not yet understood why the spectra in Fig. 6.3 show such abrupt changes in the measured $\Delta\phi^{nl}$. Contrary to expectations, decreasing the input to the RF amplifier that drove the phase modulator had little effect on the width of the notches. Due to complications with measuring the amplified RF signal and calibrating the phase modulator, it was difficult to determine the exact phase modulation amplitude. Since we wished to find a solution allowing operation with $\Delta\ell = 0$ (i.e., when the input phase modulation has no effect) we did not study this effect further. Instead, we focused on the method presented in Sect. 6.3.

6.2.6 Inter-channel XPM

We must now consider the interactions between multiple WDM channels at specific wavelengths λ_i . As discussed in Sect. 2.2.5, we assume that the frequency separation between channels $\Delta\nu \gg \Delta\nu_0$, where $\Delta\nu_0$ is defined in (2.7). This implies that neighboring wavelengths λ_i and

$\lambda_{i\pm 1}$ experience sufficient phase mismatch along the length of the fiber to be considered distinct when computing the nonlinear interactions (6.3).

The phase shift acquired by the cw signal \mathbf{B}_i^+ due to the presence of λ_j ($j \neq i$) is determined using the third and fourth terms in (6.8) with the matrices $\bar{n}_{j \rightarrow i}^+$ and $\bar{n}_{j \rightarrow i}^-$ defined by (6.6c) and (6.6d), respectively. We have presented the necessary tools to perform a detailed derivation of the phase shifts on each signal in the folded loop similar to that done in Sect.'s 6.2.2–6.2.3. However, determining the overall effect on the performance of the NOLM only requires considering the phase difference between cw and ccw beams. The effect of multiple WDM channels may therefore be easily deduced by considering that $\bar{n}_{j \rightarrow i}^+ = \bar{n}_{j \rightarrow i}^-$. In other words, the interaction between WDM channels is independent of the relative propagation direction. In a folded NOLM (Fig. 6.6), the cw and ccw signals \mathbf{B}_i^+ and \mathbf{C}_i^+ interact with four signals at λ_j : $|\mathbf{B}_j^\pm|^2$ and $|\mathbf{C}_j^\pm|^2$. Due to the inherent symmetry and the directional invariance of $(\bar{n}_{j \rightarrow i}^+ + \bar{n}_{j \rightarrow i}^-)$, the nonlinear phase shifts $\Phi_{\mathbf{B}^+}^{j \rightarrow i}$ and $\Phi_{\mathbf{C}^+}^{j \rightarrow i}$ must be equal. Therefore, $\Delta\phi_i^{nl}$ is independent of P_j .

This is an important characteristic of the NOLM-based gain equalizer. As discussed in Sect. 2.2.4, the independence of WDM channels allows the NOLM to adjust each channel's power solely as a function of its own power. Therefore, barring OA saturation changes, the steady-state power of the i^{th} channel will not change if other channels are introduced or removed within the NOLM chain. This feature is paramount in communication systems.

6.3 Intra-arm phase modulation

The important concept to understand from Sect. 6.2 is that a folded NOLM will accumulate no $\Delta\phi^{nl}$ when the cw and ccw signals enter the folded section with a constant phase difference. When a small arm-length mismatch is present, a sufficiently fast phase modulation of the signal will cause the “fifth” nonlinear term to no longer be phase matched throughout the folded fiber and hence it averages to zero over the length of the folded fiber loop. When this occurs, the imbalance between Kerr phase shifts is restored and gain equalization is again possible.

Because of the nonlinear amplitude stability issue (Sect. 4.2), we are required to operate the NOLM with a very small arm mismatch, namely with $\tau \ll 1/R_b$. Even though the CI data stream, by definition, is either phase- or frequency-modulated, the small-mismatch requirement will cause $\Delta\phi^{nl}$ to approach 0 because the phase difference $(\alpha - \beta)$ will be nearly constant. Without a nonlinear phase difference, gain equalization cannot work.

An ideal solution would allow the NOLM gain-equalization system to work with identical arm lengths $\ell_1 = \ell_2$, since this configuration is immune to the nonlinear amplitude-stability issue. This may be achieved by generating a time-varying phase difference from within the NOLM arms. In Fig. 6.8, we propose inserting a phase modulator (PM-1) into one arm. If the

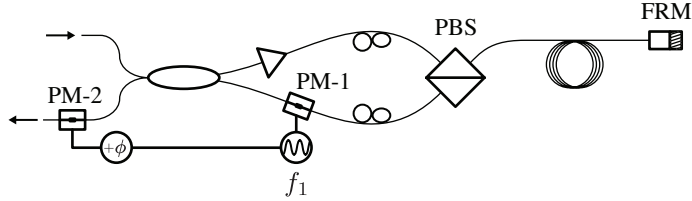


Figure 6.8: Intra-arm phase modulation.

A phase modulator PM-1 is placed within one arm of a folded NOLM with balanced arm lengths. The time-varying phase difference between cw and ccw signals disturbs the phase-matching relationship in the folded fiber loop, allowing a net $\Delta\phi^{nl}$ to accumulate. A second modulator PM-2 at the output is operated at the same frequency and with proper phase to exactly subtract the modulation imparted by PM-1.

modulation frequency $f_1 = n/\tau_{rt}$, where $n = 1, 2, 3, \dots$ and τ_{rt} is the NOLM round-trip transit time, the cw and ccw signals will be affected equally, resulting in no induced output AM.

A difficulty with this solution is that the NOLM output will now have an added phase shift from the intra-arm PM, which is unwanted as it may cause problems when the PM (or FM) data is detected. A simple solution is to remove this phase shift with a second phase modulator (PM-2) placed at the NOLM output, which must be operated with equal magnitude and exactly out of phase with the signal's modulation from PM-1.

We demonstrated the validity of this concept experimentally by including a PZT modulator in the experimental setup, as shown in Fig. 6.9. We did not demonstrate the operation of a second modulator at the output. Since our experiments use a 1-km HNL fiber coil, we need to apply a modulation at frequency $f_1 \approx n \times 100$ kHz. These relatively slow modulations are achieved using a standard PZT fiber stretcher, a piezoelectric cylinder with optical fiber wrapped around it multiple times that expands with an applied voltage. In our experiment, the PZT was operated at $f_1 = 498.3$ kHz, which corresponds to five cycles per τ_{rt} . To calibrate the PZT, we monitored the NOLM output with a photodiode and spectrum analyzer while it was operated in a power-balanced state ($L_1 = L_2$). The detected power at f and $3f$ were used to determine the phase shift using the relationship $P(f)/P(3f) = J_1(\Delta\phi)/J_3(\Delta\phi)$, where J_n are the Bessel functions of the first kind and $\Delta\phi = 2\phi_{pzt} \sin(\pi f \tau_{rt})$ is the phase difference generated by the PZT phase shift $\phi(t) = \phi_{pzt} \cdot \cos(2\pi ft)$. Since the Sagnac interferometer has zero responsivity at f_1 , we calibrated the PZT response at the frequencies $f_1 \pm 10$ kHz and averaged the two values.

Finally, the NOLM's nonlinear switching was measured for various ϕ_{pzt} values. The ratio P_A/P_B was measured and the phase difference was calculated by solving

$$\frac{P_A}{P_B} = \frac{\cos\left(+\frac{\pi}{3} + \Delta\phi^{nl}\right)}{\cos\left(-\frac{\pi}{3} + \Delta\phi^{nl}\right)}, \quad (6.41)$$

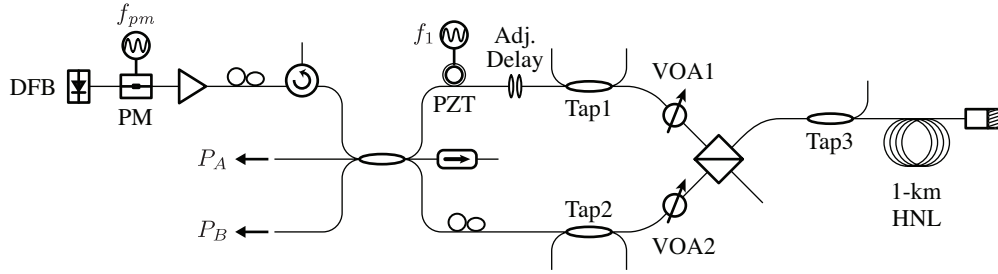


Figure 6.9: Schematic of experiment setup measuring $\Delta\phi^{nl}$ vs. intra-arm phase modulation.

A PZT fiber stretcher is placed in Arm 1 and sinusoidally modulated at $f_1 = n/\tau_{rt}$ ($n = 1, 2, 3, \dots$), so the induced phase difference has no effect on the output amplitude. The modulated phase difference between cw and ccw beams in the folded fiber will disrupt the phase-matching condition (6.32), allowing $\Delta\phi^{nl} > 0$.

which is derived from the NOLM transfer function (2.5). The input signal was phase modulated at $f_{pm} = 100$ MHz to reduce SBS. The VOAs were adjusted such that $L_1 - L_2 = 0.75$, providing a 6-dB power imbalance between cw and ccw signals (just as in Fig. 6.3). The NOLM arm lengths were balanced to within $\tau = \pm 0.1$ ns. The results are shown in Fig. 6.10 when $P_{cw} = 14.5$ mW and $P_{ccw} = 3.6$ mW upon entering the folded fiber coil (measured at Tap3). As the PZT modulation amplitude was increased, the nonlinear phase difference was restored to a maximum value of 0.15 rad. This is approximately 17% below that reported in Figs. 6.2 and 6.3, which is expected due to the reduced input power caused by the insertion loss of the PZT stretcher.⁸

When $\phi_{pzt} > \pi$, any pair of photons from Arm 1 and 2 with phase difference $(\alpha - \beta)$ will experience counter-propagating photon pairs with phases such that $(\alpha - \beta + \delta - \epsilon)$ oscillates with a magnitude greater than 2π along the fiber length. Therefore, the exponential factor in (6.34) should completely average to zero at $\phi_{pzt} = \pi$. In Fig. 6.10, we observe complete restoration of $\Delta\phi^{nl}$ at $\phi_{pzt} \approx 2$ radians. Unfortunately, we could not drive the PZT with $\phi_{pzt} \gtrsim 2.3$ rad due to its limited response at $f_1 \approx 500$ kHz. Although larger phase shifts ϕ_{pzt} were achieved when $f_1 < 500$ kHz, we did not achieve complete restoration of $\Delta\phi^{nl}$ until $f_1 \approx 500$ kHz. Further experimentation is required to understand what occurs in the regime between zero modulation ($\alpha - \beta + \delta - \epsilon = \pm\pi$) and modulation large enough to cause $e^{i(\alpha - \beta + \delta - \epsilon)}$ to average to zero during propagation. This problem might be related, and its solution shed some light on, the issue of abruptness in the frequency dependence pointed out in Fig. 6.3.

It would also be interesting to study how many phase oscillations are required within one round trip of the folded loop to achieve sufficient averaging; i.e., given $f_1 = n/\tau_{rt}$, what is the

⁸Ideally, a PZT stretcher can be fabricated with nearly 0-dB insertion loss since the optical beam never exits the single-mode fiber. In our setup, the PZT used a fiber with reduced mode-field area resulting in approximately 0.8 dB of insertion loss upon splicing it into the SMF used in the rest of the NOLM.

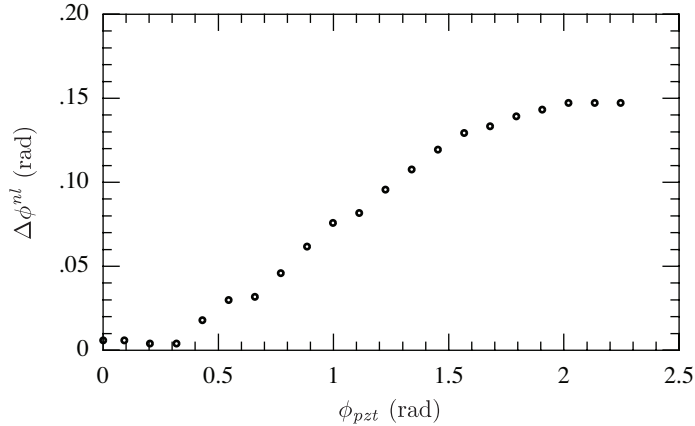


Figure 6.10: $\Delta\phi^{nl}$ vs. PZT modulation amplitude.

As ϕ_{pzt} is increased, the phase-matching condition (6.32) is no longer satisfied. The imbalance between the Kerr phase shifts that provide $\Delta\phi^{nl}$ is restored because the exponential factor in the “fifth” nonlinear term (6.34) averages to zero.

minimum allowable value of $n = 1, 2, 3, \dots$? Due to the limited bandwidth and phase response of the PZT, we were able to verify that the method works at $f_1 \geq 500$ kHz ($n \geq 5$), but we could not determine if using a smaller n is possible if larger ϕ_{pzt} were available. The above experiments will likely require replacing the PZT stretcher with an electro-optic phase modulator capable of bi-directional operation that can attain large phase shifts across a wider bandwidth. This becomes especially important if ℓ_{loop} is decreased due to the availability of fiber with larger nonlinearity, as the required modulation frequency will then increase.

Having accomplished our goal of proving that we can easily remove the deleterious effects of the “fifth” nonlinear term in a NOLM with balanced arm lengths, we will now show that using an intra-arm modulation allows us to successfully demonstrate the key operating principles of the NOLM-based gain-equalizing system.

6.4 Experiments

The introduction of an intra-arm phase modulator (Sect. 6.3) allows the folded NOLM to be operated with an arbitrarily small arm mismatch $\Delta\ell$, which is required to suppress the nonlinear amplitude instability addressed in Sect. 4.2. Without the modulator, a phase-matched four-wave mixing process between photons of all four beams in the folded loop occurs that exactly cancels out the necessary $\Delta\phi^{nl}$. The phase modulator breaks the phase-matching condition and, when its frequency is chosen appropriately, does not introduce an added amplitude modulation at the NOLM output.

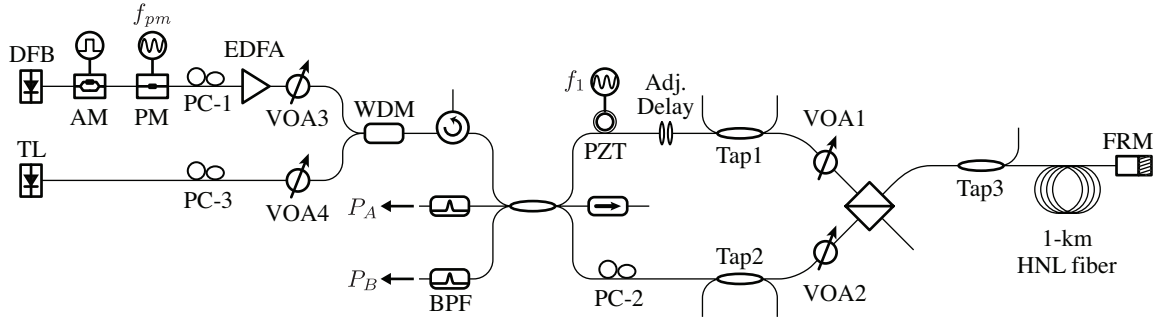


Figure 6.11: Experimental setup used to generate Fig.’s 6.12 and 6.13.

Two sources are used to simulate WDM channels at distinct wavelengths. The DFB source ($\lambda = 1559$ nm) may be pulsed using an amplitude modulator and pulse generator. Because of the high power following the EDFA, the DFB source must be phase modulated to reduce SBS. A tunable laser source (TL) is not amplified and used as a probe.

The experiments in this section were performed using the setup shown in Fig. 6.11. The DFB laser source ($\lambda = 1559$ nm) was followed by amplitude and phase modulators while an EDFA boosted its power. We found that when the EDFA pump power was changed, the birefringence in the erbium-doped fiber changed sufficiently to require readjusting PC-1 and PC-2. As a remedy, a new VOA (VOA-3) was introduced in order to easily vary the power without affecting the SOP. An external-cavity tunable diode laser (TL) was combined with the DFB source using a “red/blue” wavelength-division multiplexer (WDM), which combines pass-bands of 1530–1543 nm and 1547–1561 nm from two input fibers. After being split by the 3×3 coupler, the cw and ccw beams’ powers were varied using VOA1 and VOA2, respectively. The cw beam also experienced a phase modulation with a PZT fiber stretcher before reaching the PBS.

The arm-length difference was minimized by adding or removing fiber, while fine-tuning was performed with an adjustable delay stage composed of fiber-pigtailed collimators on translation stages placed in Arm 1, which allowed for up to 5 cm of travel. By generating rectangular pulses with the DFB and AM, we could measure the time delay between the two pulses reaching the PBS. With this method, we could achieve $\Delta\ell = 0 \pm 1$ cm ($\tau = 0 \pm 0.05$ ns). The precision was limited by pulse jitter from the electrical pulse generator, but it was sufficient for the purposes of these measurements.

The PZT fiber stretcher was operated at $f_1 = 498.3$ kHz and $\phi_{pzt} \approx 2.25$ rad, the maximum value shown in Fig. 6.10. The DFB was phase modulated at 100 MHz for SBS suppression. The NOLM contained a 1-km HNL fiber coil with $\gamma \approx 10$ ($\text{W km})^{-1}$. The fiber attenuation was 0.43 dB/km, resulting in $\ell'_{eff} = 1.78$ km for the folded fiber.

Using the 1559-nm DFB source and no amplitude modulation, we observed the NOLM output

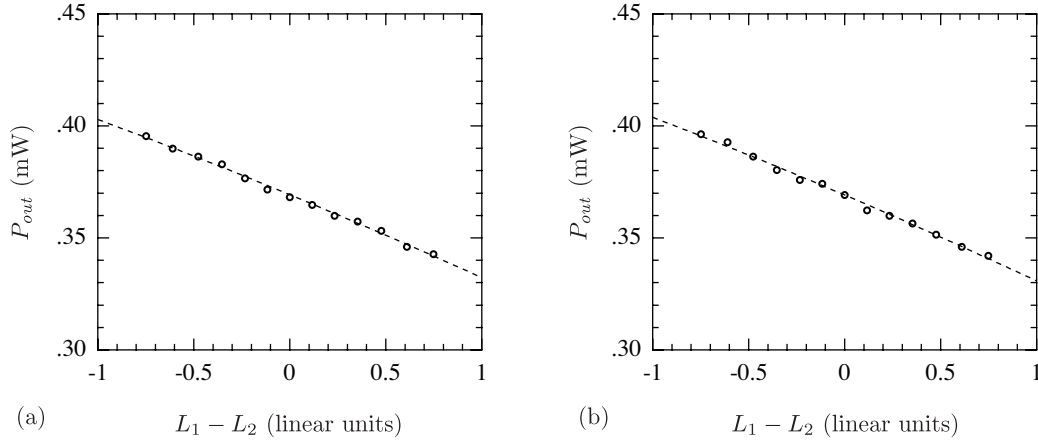


Figure 6.12: NOLM switching vs. instantaneous power.

The nonlinear phase shift is scaled by adjusting the asymmetry parameter ($L_1 - L_2$) while maintaining $L_1 L_2 = 0.25$. (a) Constant-intensity DFB signal with power from each arm $P_{arm} = 10.3$ dBm (measured with Tap6). From least-squares fit: $\gamma = 9.7 \pm 0.4$ (W km) $^{-1}$. (b) 5.5 MHz pulses are generated with 8.8% duty cycle and same average power as (a). Similar nonlinearity $\gamma = 10.1 \pm 0.5$ (W km) $^{-1}$ attained, demonstrating NOLM responds only to average power.

power dependence on asymmetry parameter ($L_1 - L_2$) shown in Fig. 6.12. We used a procedure similar to the one used in Sect. 4.1.4. The total VOA loss $L_1 L_2 = 0.25$ (-6 dB) was maintained for all measurements, thus the observed change in output power is due solely to the nonlinear phase difference (4.7). Figure 6.12(a) was measured for $P_{arm} = 10.3$ dBm, where P_{arm} is the power entering the folded fiber coil from each arm when $L_{VOA} = 0$ dB, i.e., when the VOAs are transparent. The least-squares fit (dashed line) predicts a nonlinearity $\gamma = 9.7 \pm 0.4$ (W km) $^{-1}$, where the error is computed from the fit's 95% confidence interval. This nonlinearity value is in excellent agreement with the manufacturer's specified value.

In Fig. 6.12(b), the DFB signal is pulsed using the amplitude modulator and a rectangular-pulse generator set to 5.5 MHz and 8.8% duty cycle. The input power is adjusted such that the average power is identical to that used in Fig. 6.12(a), giving a peak instantaneous power $\frac{\langle P \rangle}{0.088} \approx 11.4 \times \langle P \rangle$. The least-squares fit gives a nonlinearity $\gamma = 10.1 \pm 0.5$ (W km) $^{-1}$, where γ was calculated using (4.7) and the average signal power. This value is again consistent with the manufacturer's specified value.

This result demonstrates that increasing the instantaneous power by an order of magnitude has no measurable effect on the nonlinear phase shift. It shows that the SPM and co-propagating XPM coefficients (6.20) are indeed equal in the long, randomly birefringent fiber. This results in a net nonlinear phase difference that only depends upon the average counter-propagating power in the folded loop.

Finally, to demonstrate the expected independence of WDM channels, we examine the interaction between two signals at different wavelengths. The DFB/EDFA combination is used as a high-power pump at $\lambda_p = 1559$ nm, while the tunable laser provides a probe signal at $\lambda_s = 1540$ nm. The goal is to show that the NOLM output at λ_s is unaffected by $P(\lambda_p)$; i.e., no net $\Delta\phi^{nl}$ is generated at one wavelength by the presence of other wavelengths. The PM, PZT, and arm mismatch settings remain unchanged from the previous experiment and the AM is not used.

The DFB and TL sources each have a PC that is adjusted to assure its SOP is appropriately set upon reaching the PBS through Arm 1: PC-1 and PC-3, respectively. PC-2, however, is shared by both signals. Since the fibers used were all non-PM, the two wavelengths will have different polarization evolutions in Arm 2, thereby making it unlikely that they will be both properly aligned upon reaching the PBS. This will result in a small and manageable added PBS insertion loss (IL) for one or both signals. Our methodology for adjusting the three PCs is as follows: First, we adjust the VOAs such that only arm one is transparent ($L_1 = 1$, $L_2 = 0$) and alternately use the DFB and TL source to adjust PC-1 and PC-3 by maximizing $P(\text{Tap3})$. The VOA's roles were then reversed ($L_1 = 0$, $L_2 = 1$) and the TL source (λ_s) was used to adjust PC-2 by maximizing $P(\text{Tap3})$. Finally, using only the DFB (λ_p), we readjusted PC-1 in order to determine the added IL from transmission through the PBS from Arm 2. Fortunately, because of the small amount of fiber in each arm (< 10 m), there was less than 0.05 dB additional PBS IL at λ_p .

The wavelength-dependent SOP changes in the arms will not only add an additional IL at the PBS, but it will also change the relative SOPs of the interfering cw and ccw beams as they return to the Sagnac coupler. If these two signals are not co-polarized at interference, 100% fringe contrast will not be possible. In a real system, this reduction in contrast will reduce the NOLM's gain-flattening ability; this effect should be taken into account in a real-world system. For this experiment, since we are only using λ_p as a pump source and not measuring its interference at the Sagnac coupler, this effect is of no importance and we are concerned only with adjusting the SOP of λ_s accurately. It is for this reason that we used the TL source to adjust PC-2. In a WDM communication system, where each wavelength is a data carrier whose NOLM switching behavior is important, PM fibers may be required in the two arms depending on the amount of birefringence and/or arm length.

Using the TL source, the VOAs were adjusted to provide $L_1 = 0$ dB and $L_2 = -6$ dB ($L_1 - L_2 = 0.75$). The power entering the 1-km HNL fiber was measured using Tap3: $P_{cw}(\lambda_s) = -4.13$ dBm; $P_{ccw}(\lambda_s) = -10.13$ dBm. The NOLM output powers $P_A(\lambda_s)$ and $P_B(\lambda_s)$ were detected using tunable band-pass filters (BPFs) to remove the pump. The total pump power entering the 1-km HNL fiber $P(\lambda_p)$ (measured using Tap3) was varied using VOA3, while $P_{out}(\lambda_s)$ was recorded. As seen in Fig. 6.13, $P_A(\lambda_s)$ and $P_B(\lambda_s)$ decreased by only 2.5% and 5%, respectively, as $P(\lambda_p)$ was increased from zero to 18 mW. These very small power changes support our model,

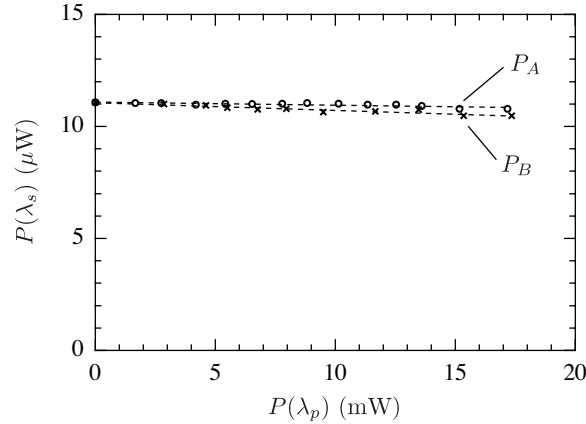


Figure 6.13: NOLM output vs. power at second wavelength.

The outputs P_A and P_B of a weak signal ($\lambda_s = 1540$ nm) were measured in NOLM pictured in Fig. 6.11. The VOA settings were $L_1 = 0$ dB and $L_2 = -6$ dB ($L_1 - L_2 = 0.75$). The total pump power entering the HNL fiber $P(\lambda_p)$ was varied with VOA3 and monitored at Tap3. P_A and P_B both decrease as $P(\lambda_p)$ is increased due to stimulated Raman scattering.

which predicts the nonlinear phase difference of a channel is independent of other channels.

To understand the origin of these small power changes, we consider the relative behavior of the two ports' output powers at λ_s versus pump power. Since the two ports experience a power changes with the same sign, they are not consistent with what should happen if the pump wave induces a $\Delta\phi^{nl}$ upon the signal. Because of the different bias phases $\phi_{bias} = \pm\pi/3$, an induced phase difference would cause the output power of one to increase while the other decreases. Instead, we observe a decreased power at *both* output ports as the pump power is increased.

This net power loss at λ_s can be understood by considering another nonlinear effect present in the NOLM: stimulated Raman scattering (SRS). Quantum mechanically speaking, Raman scattering is the process by which a photon interacts with a phonon mode, causing a change in its vibrational state. The scattered photon has less energy than the incident photon, and therefore a positive wavelength shift occurs. When two signals with adequate frequency separation $\Delta\nu$ are incident, the lower-frequency signal will experience Raman gain due to the nonlinear SRS effect [111].

In our experiment, SRS gain at $\lambda_p = 1559$ nm causes attenuation at $P(\lambda_s = 1540$ nm).⁹ Since the weak signal (λ_s) acts as the Raman pump, we can model the effect assuming near-complete pump depletion by assuming no change in power at $\lambda = 1559$ nm.¹⁰ Using the methods of [111],

⁹Note that the shorter-wavelength signal is conventionally called the Raman *pump*. In this regard, our nomenclature is reversed because the stronger signal used in our pump-probe experiment has a longer wavelength.

¹⁰This is the opposite of the condition that is most commonly experienced; namely, when the Raman pump (the signal with the shorter wavelength) has a much higher power than the longer wavelength signal (which experiences

we can calculate the gain at $\lambda_s = 1540$ nm

$$G_s = e^{-\left(\frac{g_R P(\lambda_p) \ell_{eff}}{A_{eff}}\right)}, \quad (6.42)$$

where g_R is the Raman gain coefficient in fused silica. Because we could not access the fiber ends of the pigtailed HNL-fiber spool, we could not directly measure the mode area. The nonlinearity $\gamma = \frac{2\pi n_2}{\lambda A_{eff}}$ was about 10 (W km)^{-1} , as ascertained from our experiments. Using the data presented in Table I in [61] for similar DSFs with germanium-doped cores from the same manufacturer, we can roughly estimate the nonlinear index to be $n_2 \approx 4 \times 10^{-20} \text{ m}^2/\text{W}$ and the effective area to be $A_{eff} \approx 16 \text{ }\mu\text{m}^2$. The Raman gain $g_R \approx 1.2 \times 10^{-14} \text{ m/W}$ between our signals was estimated using Fig. 8.1 in [111], resulting in $G_s \approx 0.975$ when $P(\lambda_p) = 18 \text{ mW}$ — a 2.5% loss.

The magnitude of the power reductions observed in Fig. 6.13 are consistent with the 2.5% loss expected from SRS. The small discrepancy in the losses at ports A and B implies that the pump may have a small effect on the signal's $\Delta\phi$. Whether the phase shifts originate from the Raman or Kerr effects is not known at this time. The $\sim 2.5\%$ difference between P_A and P_B requires $\Delta\phi \approx 0.007$ radians. This value is over $20\times$ smaller than the same-channel nonlinear phase difference at the same power level.¹¹

6.5 Summary

The material in this chapter was developed in response to a single requirement imposed upon the folded NOLM-based gain equalizer: the two arms that connect the Sagnac coupler to the PBS must have nearly equal lengths to achieve amplitude stability. We experimentally discovered that this constraint had the unforeseen, detrimental consequence of eliminating the nonlinear phase difference $\Delta\phi^{nl}$ that is paramount to the gain equalization action (see Sect. 6.1).

Any single WDM channel causes four fields to be present in the folded fiber coil: the cw and ccw fields co-propagate in the folded fiber, while their reflections counter-propagate in the backward direction. Adding the four self- and cross-phase modulations experienced by the cw field and subtracting the four experienced by the ccw field results in the nonlinear phase difference $\Delta\phi^{nl}$. Available models predicted each of these phase shifts and were thought to be applicable, but our experiments showed that the analysis broke down in folded NOLMs with nearly balanced arm lengths.

To solve this problem of restoring $\Delta\phi^{nl}$, we had to first develop a unified model of the third-order nonlinear interactions in a folded NOLM with randomly birefringent fiber. In Sect. 6.2, this

positive gain). In this situation, one can assume *no* pump depletion when the power of the Raman pump is nearly unchanged during propagation.

¹¹For a quick comparison, see Fig. 6.10, which used the DFB source at a similar power.

unified model was presented. We redefined the fields in the folded loop in terms of *global* eigenstates of the folded system (see Fig. 6.4), and subsequently analyzed their nonlinear interactions. This new analysis revealed in addition to the four expected phase modulations, another nonlinear interaction is present in the folded loop. Because the four fields in the folded loop all originate from the same source, their inter-related phases allow a degenerate four-wave mixing process to be phase matched along the entire fiber length. This process generates a “fifth” nonlinear phase shift whose magnitude and sign exactly eliminates $\Delta\phi^{nl}$, rendering the gain equalization functionality impossible (see Sect. 6.2.4).

Fortuitously, our experiments also provided the clue that enables us to restore the NOLM’s nonlinear phase difference. In Sect. 6.2.5, we showed that a relative phase modulation between the cw and ccw signals breaks the phase matching of the four fields in the folded loop. This was achieved automatically in NOLMs with unbalanced arm lengths and phase modulated sources, but with balanced arms, it was achieved by introducing an additional intra-arm phase modulator to remove the phase matching (see Sect. 6.3). Using this intra-arm phase modulation, we successfully demonstrated a folded NOLM with balanced arms with the necessary performance criteria:

1. Nonlinear phase difference is non-zero.
2. NOLM provides increased output power for less intense input signals;
3. Folded NOLM is desensitized to acoustic perturbations;
4. Amplitude stability is achieved because the nonlinear transfer function scales only with average signal power (i.e., independent of instantaneous power) and therefore will have no effect on the intensity noise of the input signal;
5. Transfer functions for each WDM channel are independent.

Chapter 7

Summary and discussion

7.1 Key developments

In this dissertation, we have demonstrated how a nonlinear-optical device can be used to perform automatic gain equalization in long-haul WDM communication systems. The basic building block of the system is the nonlinear-optical loop mirror: an all-fiber Sagnac interferometer that can switch power between its output ports as a function of input power. The NOLM splits an incoming signal into two beams that propagate around a common fiber loop in opposite directions (see Chapter 2). An amplifier or attenuator placed at one end of the fiber loop generates a power imbalance between the two counter-propagating beams, which, through the Kerr effect present in the loop fiber, causes the beams to acquire different, power-dependent phase shifts during propagation. The resulting nonlinear phase difference $\Delta\phi^{nl}$ generates a power-dependent NOLM output after the beams interfere at the Sagnac coupler.

NOLMs have been used by many researchers for a variety of applications [3–5, 7, 10, 11]. The following sections summarize the advancements achieved in this field in the course of our research, beginning with the initial concept of using the NOLM as a gain equalizer.

7.1.1 Gain-equalization concept

In Chapter 3, we introduced the concept of using cascaded NOLMs to perform gain equalization in communication systems consisting of a series of fiber links and optical amplifiers (OAs) by using constant-intensity (CI) modulation formats. Due to the nonlinear transfer function of the NOLM, after multiple gain-loss links the power of each WDM channel P_i approaches a steady-state value $P_i^{(\infty)}$. Even when the gain of each channel differed, the NOLM chain can maintain each channel at $P_i^{(\infty)}$ indefinitely. This behavior effectively “flattens” the gain spectrum of each OA. Successful implementation of such a system in long-haul communication links could greatly

reduce, if not eliminate, the need for gain-flattening filters, spectral monitoring, and active control of individual channel powers.

The conventional NOLM configuration uses a simple fiber loop to connect the Sagnac coupler's ports and carry the counter-propagating beams (see Fig. 2.4). While this configuration can be used for gain equalization, it was shown in Sect. 3.3 that it suffers from a nonlinear amplitude instability that causes intensity modulations to be amplified with each link. This problem can be avoided by using a "folded" loop (see Chapter 4) in which the two interfering beams *co*-propagate in the long nonlinear fiber coil (see Fig. 4.1(b)). When the two arms of the folded NOLM have equal length, two problems are solved simultaneously. First, the interferometer becomes insensitive to acoustic perturbations (see Sect. 4.1.1). Second, the nonlinear response of the NOLM becomes dependent only on the *average* power of the signals. The lack of a response to instantaneous power eliminates the NOLM's propensity to amplify intensity modulations. Unfortunately, using a folded NOLM with balanced arm lengths also introduced a dramatic, unwanted change in the device's operation, namely cancellation of the nonlinear phase difference. This issue, along with the method we used to restore functionality to the NOLM gain equalizer, is discussed in the following section.

7.1.2 Nonlinear interactions in folded NOLMs

As discussed above, the arms of a folded NOLM need to be nearly equal in length to promote amplitude stability. In Chapter 6, we experimentally demonstrated that this constraint had the unforeseen, detrimental consequence of eliminating the nonlinear phase difference $\Delta\phi^{nl}$ that is necessary for gain equalization. This behavior was not predicted using the commonly quoted nonlinear Kerr phase shifts (4.5) induced by the fields present in the folded loop.

To model the nonlinear interactions in a folded fiber, we accounted for the simultaneous presence of four distinct fields at each wavelength: two orthogonal SOPs traveling in two directions. Additionally, the backwards-propagating fields are reflections of the forward-propagating fields. This relationship causes the four fields to have a fixed phase relationship throughout the long, randomly birefringent fiber, and allows a particular set of four-wave mixing terms (6.33) to be phase matched. When this occurs, the resulting nonlinear phase difference $\Delta\phi^{nl}$ equals zero. This result, which is predicted by our model and was verified with experiments, implies that the folded NOLM with *balanced* arms *cannot* operate as a nonlinear gain equalizer as long as this additional nonlinear interaction is present.

The insight gained from our model allowed us to modify the folded NOLM such that this unwanted nonlinear interaction could be eliminated while maintaining matched arm lengths (needed for amplitude stability). This result was demonstrated in Sect. 6.3 by phase modulating the signal as it passes through one of the NOLM arms. Doing so breaks the phase-matching condition

in the folded fiber loop, causing the unwanted nonlinear effect to average to zero. The remaining Kerr phase shifts are identical to (4.5), providing the desired $\Delta\phi^{nl}$.

To summarize, by using intra-arm phase modulation, we successfully demonstrated a folded NOLM with balanced arms that had the performance criteria necessary for gain equalization:

1. NOLM provides increased output power for input signals with lower power;
2. Folded NOLM is desensitized to acoustic perturbations;
3. Amplitude stability is achieved because the nonlinear transfer function scales only with average signal power (i.e., independent of instantaneous power) and therefore will have no effect on the intensity noise of the input signal;
4. Transfer functions for each WDM channel are independent.

7.1.3 Electrostriction-induced acoustic modes

In addition to the behavior discussed in the previous section, a second unexpected nonlinear response was also observed (see Chapter 5). When an optical mode is present, the electrostrictive force (5.2) compresses and deforms the fiber, which induces an index change and birefringence, respectively. The electrostriction-induced birefringence is maximum for (and aligns with) a linearly polarized field and zero for a circularly polarized field. When the source being launched into a folded NOLM is phase modulated at frequency f_{pm} , a mismatch in NOLM arm length will cause the total field in the folded loop (i.e., the sum of the cw and ccw beams) to have a time-varying SOP. Because of the polarization dependence of electrostriction, this time-varying SOP induces a dynamic birefringence in the fiber at frequency f_{pm} .

This effect is easy to measure with the folded NOLM. The FRM returns the cw and ccw beams to the PBS in their orthogonal polarizations for any static birefringence in the folded loop. However, a dynamic birefringence will cause the beams to return in rotated SOPs, which is easily measured since it causes a change in the splitting ratio of the PBS. By using sufficiently long, high-power pulses, we were able to demonstrate electrostriction-induced excitation of the fiber's acoustic modes by measuring the change in PBS splitting across a range of frequencies f_{pm} . When f_{pm} coincided with the specific resonant frequency of a vibrational mode, a large resonant enhancement was observed (see Fig. 5.10).

Other published observations have measured thermally excited modes with relatively small amplitudes. To the best of our knowledge, this is the first measurement of optically pumped acoustic modes of a fiber. Although this work has little impact on the gain-equalization application of the NOLM, it deserves mention purely for its academic significance.

7.2 NOLM-based gain equalization: Benefits and drawbacks

The NOLM-based gain equalizer introduced in this dissertation is fundamentally different from conventional gain-flattening filters (GFFs) or dynamic gain equalizers (DGEs), which provide a fixed or tunable wavelength-selective attenuation, respectively. Instead, the folded NOLM responds automatically to the power of an individual WDM channel, with higher power channels receiving more attenuation than weaker channels. In this way, the powers of multiple channels converge after repeated amplifications.

In Sect. 1.2.3, we outlined the operating principles of a theoretical *ideal* gain equalizer. We can now compare the NOLM-based gain equalizer to the list of attributes found on page 8. The attenuation provided by the NOLM's switching behavior is wavelength-dependent, but automatically adjusts as a function of the power at each wavelength. The net gain experienced by each channel is equal after they have reached their respective steady-state powers. This behavior exists for any input WDM channel spectrum and for gain profiles with variations below a limit that is dictated by the NOLM design parameters and tolerable variation between the WDM output powers (see Sect. 3.2.2). The unique benefits of the NOLM-based gain equalizer are summarized below:

1. Fully automatic gain equalization—no monitoring or active feedback required.
2. All channels converge to a fixed (channel-dependent) power (unlike with the residual wavelength-dependent gain of flattened amplifiers).
3. Able to withstand changes in gain profile due to channel add/drop, pump power change, etc.

However, these benefits are accompanied by several system limitations:

1. Requires constant-intensity modulation formats (see Appendix A). Nearly all deployed commercial networks currently employ amplitude modulation. However, in an effort to increase spectral efficiency, there has recently been a renewed interest in CI formats, especially DPSK [112–119], for which the NOLM gain equalizer would be applicable.
2. Requires a fixed, known input SOP for each WDM channel (today's fiber links are *not* polarization controlled). This would require either using PM-fiber between repeaters, providing channel-by-channel polarization control before each NOLM, or developing some type of “automatic polarization controller”. Using PM fiber is the most practical of these three options, but it would require significant infrastructure changes since most, if not all, of the world's buried fiber is non-PM.

3. Placing the OA within the NOLM loop (i.e., NALM configuration) might lead to instabilities since it cannot be isolated (it must operate bidirectionally). Placing the OA in line with the NOLM introduces excess attenuation from VOAs, thus reducing the reach of a fiber link.
4. Cannot operate in a bidirectional link. This is a minor point since most communication links already operate with one fiber for each direction.
5. Electrical power is required to operate the intra-arm phase modulator, hindering use in undersea repeaters. However, perhaps a passive scheme can be devised to remove the phase matching of the “fifth” nonlinear term (Sect. 6.3).
6. Effect of extra phase modulation on noise performance of a phase- or frequency- modulated system.
7. Increased signal impairments from introducing a complex, nonlinear system to a network. See Sect. 7.3.

The first six of the above drawbacks require a cost analysis to determine the system’s practicality. However, the final item deserves additional research before concluding whether it constitutes a severe limitation.

7.3 Future research: Signal impairments

Now that the fundamental principles of the NOLM-based gain equalization system have been successfully demonstrated, future research should focus on its practicality. This work must necessarily include both theoretical and experimental studies of the impact of cascaded NOLMs on the integrity of the communication signal. Thus far, we have developed a nonlinear device that is capable of automatically adjusting the transmitted power of optical beams at separate wavelengths such that they do not diverge when the OA gain is non-uniform. But we have not studied the NOLM’s effects on either the noise figure (NF) of the amplifier chain or bit error rate (BER) of a detected communication signal.

In this section, we briefly discuss two possible BER-limiting effects. First, the folded loop will introduce both intensity and phase noise to the output signal if beams return to the Sagnac coupler through the wrong port of the PBS due to either its limited extinction ratio or the finite bandwidth of the FRM. Second, the use of highly nonlinear fiber and relatively large signal powers (to achieve a $\Delta\phi^{nl}$ large enough for gain equalization) in the NOLM will also increase the magnitude of optical nonlinearities that are detrimental in optical communications, e.g., pulse distortion from SPM and XPM, channel crosstalk from XPM and four-wave mixing, spontaneous Raman noise, etc. Experimental demonstrations will likely require telecom equipment capable of

CI modulation formats, which requires using either coherent detection or differential phase-shift keying (DPSK) [120, 121].

7.3.1 Impact of PBS and FRM on noise figure

This section would not be necessary if the PBS and FRM used to fold the NOLM (Fig. 4.2) behaved as *ideal* components—in practice, both devices have physical limitations. The PBS has a finite extinction ratio (ER), implying its output is not 100% polarized. Additionally, an input signal that is polarized such that it *should* entirely exit one output port will generate some leakage out of the second output port; i.e., the polarization-dependent loss is finite (an ideal PBS has infinite polarization-dependent loss). This is sometimes referred to as either the *power* extinction ratio or polarization crosstalk.

The FRM consists of a Faraday crystal placed in front of a mirror. The crystal’s length is cut such that a 45-degree rotation of the signal’s principle polarization axes occurs on each pass at the design wavelength. The combination of this rotation with the change in polarization circularity from reflection causes any incoming SOP to return from the FRM in the orthogonal state. If the wavelength of the beam differs from the design wavelength, the rotation applied by the Faraday crystal will deviate from 90° after the second pass, causing the SOP to be slightly misaligned from the desired orthogonal state. For a typical FRM designed to operate at $\lambda_0 = 1550$ nm, a linearly polarized signal experiences a 1° rotation error for every ~ 8 nm of separation between its wavelength and λ_0 . An incoming circular SOP does not experience this error—its output is orthogonal to the input solely because of the reflection from the mirror in the FRM (i.e., the rotation from the crystal is not necessary). Elliptical polarization states experience an error in rotation magnitude that is dependent on the degree of ellipticity.

The above performance limitations of *real* optical components causes some fraction of the cw and ccw beams to return to the Sagnac coupler through the wrong arms. Having not made a complete round trip around the NOLM, the mis-routed light will have an unknown phase relationship with the correctly routed cw and ccw beams. The signals will interfere when they are combined at the Sagnac coupler, which will introduce phase and intensity noise at the output.

In the folded NOLM used in our experiments, we measured the total polarization crosstalk PXT of the PBS and FRM combination. This was performed by blocking the beam at the bulk-optic delay stage (see Fig. 6.11), thus allowing only the ccw beam to reach the PBS. The ccw beam traversed the folded loop and *ideally* should have been routed by the PBS *entirely* into Arm 1. Of course, as we have discussed above, a portion of the ccw beam leaked through the PBS into Arm 2. We measured the power at the 1% couplers Tap1 and Tap2, and defined the crosstalk to be $PXT = P(\text{Tap2})/P(\text{Tap1})$. We used a 1559-nm DFB laser diode as the source and an FRM with design wavelength $\lambda_0 = 1550$ nm. Since the crosstalk is dependent on the SOP at the FRM, a polarization controller (PC-4) was placed between the PBS and Tap3 (not shown

in Fig. 6.11). By adjusting PC-4, we measured maximum and minimum values of $PXT = -21.1$ dB and -21.8 dB, respectively. It is assumed that the minimum crosstalk was observed when a circular SOP was incident upon the FRM. This level of crosstalk corresponds to more than 1 out of every 150 incident photons being mis-routed by the PBS after returning from the FRM. The beating of these photons with the signal caused the excess intensity noise shown in Fig. 4.7 and NOLM output power fluctuations that were observed at levels up to approximately ± 0.1 dB.

To detect a signal after multiple NOLM-based gain equalizers with an acceptably low BER, it is expected that the polarization crosstalk from the folded loop (i.e., the PBS, fiber coil, and FRM combination) will need to be reduced from the level present in our prototype. Further research is necessary to quantify the noise introduced by the limitations of the PBS and FRM and to determine if the minimum noise level—attained using the highest quality components available—is acceptable. Furthermore, development of an FRM with a larger operating bandwidth could decrease the noise figure.

7.3.2 Nonlinear signal impairments

Our proposed gain-equalization system utilizes the nonlinear response of an optical fiber to perform a useful function. In contrast, there are a multitude of nonlinear effects that degrade the performance of an optical communication system [73, 122, 123]. Stimulated Brillouin scattering (SBS) causes a saturation of the transmitted light. Stimulated Raman scattering (SRS) introduces channel crosstalk and wavelength-dependent gain/loss in multi-channel systems. The Kerr effect, namely SPM and XPM, cause pulse distortion, spectral broadening, and modulation instability (MI). And finally, XPM and four-wave mixing (FWM) induce channel crosstalk. These nonlinear impairments place practical limitations on the launched signal power, WDM channel spacing, bit rate, fiber dispersion, and transmission distance [72, 124, 125].

The above effects all scale with the optical power and $\frac{1}{A_{eff}}$, while the third-order $\chi^{(3)}$ nonlinearities (SPM, XPM, and FWM) also scale with the fiber's nonlinear refractive index n_2 . To perform gain equalization, we require sufficiently large Kerr phase shifts in the NOLM, which are achieved by using relatively high optical powers and a highly nonlinear (HNL) fiber with large nonlinearity $\gamma = \frac{2\pi n_2}{\lambda A_{eff}}$ (see Chapter 3). Unfortunately, increasing the NOLM's loop length, fiber nonlinearity, and/or input power will be accompanied by an increase in the degenerative nonlinear effects listed above.

We have not studied in detail the trade-off between the positive effects of NOLM-based gain-equalization and the expected nonlinear signal degradation. Now that the fundamental operating principles of the NOLM gain equalizer have been demonstrated, future research must include a thorough analysis of the nonlinear impairments experienced by the data stream after transmission through multiple NOLMs. One should be able to determine the communication system's performance limitations after defining metrics for the NOLM chain (such as the required

$\Delta\phi^{nl}$ for a given OA gain uniformity) and using the design parameters for a commercially viable NOLM. This analysis will also require assumptions about which of several existing CI modulation schemes would be used, each of which has its own unique set of benefits and drawbacks.

Appendix A

Requirement for constant-intensity signals

Chapter 3 was prefaced with the statement that only constant-intensity (CI) communication signals (e.g., phase or frequency modulated) would be assumed throughout this dissertation without further explanation. Chapter 4 discussed the effects imparted upon input signals with small amplitude modulations, leading to the conclusion that the folded NOLM must have arms with nearly equal lengths in order to be stable in the presence of intensity noise. The *balanced* folded NOLM generates nonlinear phase shifts that are proportional only to the average power of an input signal. As demonstrated in Fig. 6.12, the folded NOLM behaves identically for two signals having the same average power but drastically different peak powers. This result may erroneously leave the impression that the folded NOLM-based gain equalizer should work for amplitude-modulated communication signals. In this appendix, we briefly discuss why the folded NOLM requires CI signals.

In the folded NOLM, the requirement for CI signals originates from the interactions between multiple WDM channels. Using the techniques of Sect. 6.2, it can be shown that the nonlinear phase shifts imposed upon the signals \mathbf{B}_i^+ and \mathbf{C}_i^+ by the presence of the j^{th} WDM channel are

$$\Phi_{\mathbf{B}^+, j \rightarrow i} = \frac{8}{9}\gamma \left(2|\mathbf{B}_j^+|^2 + |\mathbf{C}_j^+|^2 + 2|\mathbf{B}_j^-|^2 + |\mathbf{C}_j^-|^2 \right) \quad \text{and} \quad (\text{A.1})$$

$$\Phi_{\mathbf{C}^+, j \rightarrow i} = \frac{8}{9}\gamma \left(|\mathbf{B}_j^+|^2 + 2|\mathbf{C}_j^+|^2 + |\mathbf{B}_j^-|^2 + 2|\mathbf{C}_j^-|^2 \right), \quad (\text{A.2})$$

respectively. It is left to the reader to derive these expressions, though they can be inferred easily by comparing the matrices (6.6a) and (6.6c) and the results of Sect. 6.2.2. We have assumed that the two channels at different wavelengths remain co-polarized throughout the folded loop. As we'll discuss later, this condition is not always satisfied, but the conclusion still holds.

If the global eigenstates \mathbf{B}_i^+ and \mathbf{C}_i^+ represent the cw and ccw beams in a folded NOLM, respectively, the nonlinear phase difference at interference at the Sagnac coupler is the difference between (A.1) and (A.2):

$$\Delta\phi_{j \rightarrow i}^{nl} = \frac{8}{9}\gamma (P_j^{cw} - P_j^{ccw} + \langle P_j^{ccw} \rangle - \langle P_j^{cw} \rangle) \ell'_{eff}, \quad (\text{A.3})$$

where the angle brackets are used because phase shifts from counter-propagating fields scale with average power. For a CI signal, the instantaneous power is equal to the average power ($P = \langle P \rangle$), and therefore $\Delta\phi_{j \rightarrow i}^{nl} = 0$. This result implies that the transfer functions of multiple WDM channels are independent (see Sect. 6.2.6). However, amplitude-modulated signals never satisfy the condition $P = \langle P \rangle$, resulting in a non-zero nonlinear phase difference $\Delta\phi_{j \rightarrow i}^{nl}$ induced upon channel i from the presence of channel j . Therefore, the channel independence of the folded NOLM is present only when CI signals are used.

The lack of channel independence with non-CI signals is made worse when one considers that in actual communication systems, the number of WDM channels N can be upwards of 100 and $\Delta\phi_{j \rightarrow i}^{nl}$ is similar in magnitude to the self-induced $\Delta\phi_i^{nl}$. Upon exiting the NOLM, channel i 's output power is determined by its total nonlinear phase shift

$$\Delta\phi_i^{nl} = \frac{8}{9}\gamma \langle P_i^{cw} - P_i^{ccw} \rangle \ell'_{eff} + \sum_{j=1, j \neq i}^N \Delta\phi_{j \rightarrow i}^{nl}, \quad (\text{A.4})$$

where the self-induced nonlinear phase difference (the first term on the right-hand side) is from (4.6). The nonlinear switching experienced by channel i has more than a small dependence upon the power at other wavelengths—it will be *dominated* by the nonlinear phase shifts imposed by the other channels (last term in (A.4)).

The above analysis assumes that the individual bits carried by each channel overlap completely. If two channels i and j have bits that are non-overlapping, the first two terms in (A.3) are zero, resulting in a different $\Delta\phi_{j \rightarrow i}^{nl}$. In reality, no effort is made to “synchronize” the multiple WDM channels, thus bit overlap is completely uncontrolled. Additionally, the group-velocity dispersion present in the fiber link will cause the channels to experience walk-off, thus the overlap between bits will vary during propagation. Finally, the data carried by each channel is different, therefore the bit-sequences differ and overlap may change from bit to bit. Since $\Delta\phi_i^{nl}$ (and thus channel i 's output power) depends on the overlap, these effects will cause unwelcome crosstalk between channels and bit distortion.

The use of AM signals requires that a solution be found for these problems. A possible remedy could be to use a fiber coil in the nonlinear loop with a large group-velocity dispersion to increase the walk-off experienced by adjacent WDM channels. The phase shifts from co-propagating fields in the folded loop (the first two terms on the right-hand side of Eq. A.3) will

then be averaged over the walk-off length. If the walk-off is sufficiently large, $\Delta\phi_{j \rightarrow i}^{nl}$ may be reduced to zero. However, given the efforts devoted to dispersion and nonlinearity management in current systems, it is unlikely that a difficult-to-compensate, highly dispersive fiber system would be welcome within a gain-flattening device.

Additionally, the polarization state of two channels will vary along the length of the fiber coil. If this polarization walk-off is large enough (i.e., when the intrinsic fiber birefringence and/or wavelength separation of the channels is large enough) the factors of the multiple terms in (A.1) and (A.2) may average to be identical. For instance, the phase shifts induced by \mathbf{B}_j^+ and \mathbf{C}_j^+ on \mathbf{B}_i^+ have different magnitudes because \mathbf{B}_j^+ and \mathbf{B}_i^+ were assumed to be co-polarized throughout the fiber, while \mathbf{C}_j^+ and \mathbf{B}_i^+ were assumed to be orthogonally polarized. But if the SOPs of channels i and j evolve differently, these relationships are no longer valid. If sufficient “walk-off” occurs between channels i and j on the Poincaré sphere, the two phase shifts will average to be identical.

In conclusion, for folded and non-folded NOLMs, non-CI modulated signals would experience bit distortion and inter-channel crosstalk. Additionally, the NOLM would not have a channel-independent nonlinear transfer function.

Appendix B

Counter-propagating nonlinear terms ζ

The counter-propagating third-order nonlinear interactions in a folded loop (6.22) were divided into three groups:

- A_1 — Interactions involving two photons from each of \mathbf{B}_i^+ and \mathbf{B}_i^- .
- A_2 — Interactions involving two photons from each of \mathbf{B}_i^+ and \mathbf{C}_i^- .
- ζ — All remaining interactions: each has one photon from \mathbf{B}_i^+ and three from some combination of \mathbf{B}_i^+ , \mathbf{C}_i^+ , \mathbf{B}_i^- , and \mathbf{C}_i^- .

As shown in Sect. 6.2.3, A_1 and A_2 give the Kerr phase shifts from counter-propagating signals that remain co-polarized and orthogonal throughout the non-PM fiber, respectively. When the four signals originate from four unique sources, it was shown that $\langle \zeta \rangle = 0$. However, some of the terms in ζ no longer average to zero when 1) the backward-propagating signals are the FRM reflections of the forward-propagating ones, and 2) the NOLM arm mismatch τ is small compared to the input signal's phase-modulation period $1/f_{pm}$. Section 6.2.4 discussed how this affects the folded NOLM with balanced arms.

In this appendix, we list ζ in its entirety for reference.

$$\begin{aligned}
\zeta = & 2P_i^{-*} |P_i^+|^2 R_i^- + \frac{2}{3} P_i^+ Q_i^{-*} Q_i^{+*} R_i^- + \frac{2}{3} P_i^{-*} |Q_i^+|^2 R_i^- + 2P_i^- |P_i^+|^2 R_i^{-*} \\
& + \frac{2}{3} P_i^{+*} Q_i^- Q_i^+ R_i^{-*} + \frac{2}{3} P_i^- |Q_i^+|^2 R_i^{-*} + \frac{2}{3} |P_i^+|^2 Q_i^{-*} S_i^- + \frac{2}{3} P_i^{-*} P_i^{+*} Q_i^+ S_i^- \\
& + 2Q_i^{-*} |Q_i^+|^2 S_i^- + \frac{2}{3} |P_i^+|^2 Q_i^- S_i^{-*} + \frac{2}{3} P_i^- P_i^+ Q_i^{+*} S_i^{-*} + 2Q_i^- |Q_i^+|^2 S_i^{-*} \\
& + 2|P_i^-|^2 P_i^{+*} R_i^+ + \frac{2}{3} P_i^{+*} |Q_i^-|^2 R_i^+ + \frac{2}{3} P_i^- Q_i^{-*} Q_i^{+*} R_i^+ + 2P_i^- P_i^{+*} R_i^{-*} R_i^+ \\
& + 2P_i^{+*} |R_i^-|^2 R_i^+ + \frac{2}{3} P_i^{+*} Q_i^- R_i^+ S_i^{-*} + \frac{2}{3} P_i^- Q_i^{+*} R_i^+ S_i^{-*} + \frac{2}{3} Q_i^{+*} R_i^- R_i^+ S_i^{-*} \quad (\text{B.1}) \\
& + \frac{2}{3} P_i^{+*} R_i^+ |S_i^-|^2 + \frac{2}{3} P_i^{-*} P_i^{+*} Q_i^- S_i^+ + \frac{2}{3} |P_i^-|^2 Q_i^{+*} S_i^+ + 2|Q_i^-|^2 Q_i^{+*} S_i^+ \\
& + \frac{2}{3} P_i^{+*} Q_i^- R_i^{-*} S_i^+ + \frac{2}{3} P_i^- Q_i^{+*} R_i^{-*} S_i^+ + \frac{2}{3} Q_i^{+*} |R_i^-|^2 S_i^+ + \frac{2}{3} P_i^{+*} R_i^{-*} S_i^- S_i^+ \\
& + 2Q_i^- Q_i^{+*} S_i^{-*} S_i^+ + 2Q_i^{+*} |S_i^-|^2 S_i^+ + 2P_i^{-*} P_i^{+*} R_i^- R_i^+ + \frac{2}{3} Q_i^{-*} Q_i^{+*} R_i^- R_i^+ \\
& + \frac{2}{3} P_i^{+*} Q_i^{-*} R_i^+ S_i^- + \frac{2}{3} P_i^{-*} Q_i^{+*} R_i^- S_i^+ + \frac{2}{3} P_i^{-*} P_i^{+*} S_i^- S_i^+ + 2Q_i^{-*} Q_i^{+*} S_i^- S_i^+
\end{aligned}$$

Abbreviations

AM	Amplitude-modulated [signal].
ASE	Amplified spontaneous emission.
BER	Bit error rate.
BPF	Band-pass filter.
ccw	Counter-clockwise [signal in loop].
CI	Constant-intensity [signal].
cw	Clockwise [signal in loop].
CW	Continuous-wave [signal].
DC	Duty cycle.
DFB	Distributed-feedback [laser diode].
DGE	Dynamic gain equalizer.
DSF	Dispersion-shifted fiber.
EDFA	Erbium-doped fiber amplifier.
ER	Extinction ratio.
FOG	Fiber-optic gyroscope.
FRM	Faraday-rotator mirror.
FWM	Four-wave mixing.
GAWBS	Guided acoustic-wave Brillouin scattering.
GFF	Gain-flattening filter.
HNL	Highly nonlinear [optical fiber].
IL	Insertion loss.
NALM	Nonlinear amplifying loop mirror.
NF	Noise figure.
NOLM	Nonlinear-optical loop mirror.
OA	Optical amplifier.
OEO	Optical-electrical-optical [regeneration].
OFA	Optical fiber amplifier.
OOO	All-optical [regeneration].

PBS	Polarizing beam splitter.
PC	Polarization controller.
PM	Phase modulation or polarization-maintaining [fiber] (by context).
PZT	Piezo-electric [fiber stretcher].
RF	Radio frequency.
SBS	Stimulated Brillouin scattering.
SMF	Single-mode fiber.
SOP	State of polarization.
SPM	Self-phase modulation.
SRS	Stimulated Raman scattering.
TL	Tunable laser.
VOA	Variable optical attenuator.
WDM	Wavelength-division multiplexed.
XPM	Cross-phase modulation.

Symbols

α_{loop}	NOLM loop attenuation.
γ	Nonlinearity coefficient; ($= \frac{2\pi n_2}{\lambda A_{eff}}$, units: $\text{W}^{-1}\text{km}^{-1}$).
δ_m	Modulation depth.
$\Delta\nu_0$	Kerr characteristic bandwidth.
$\Delta\phi^{nl}$	Nonlinear phase difference between cw and ccw beams.
$\Delta\ell$	Arm-length mismatch ($\ell_1 - \ell_2$) of folded NOLM.
λ	Vacuum wavelength of optical signal.
τ	Transit time difference between arms of folded NOLM.
τ_{loop}	Transit time of NOLM loop.
ϕ_{bias}	Bias phase of NOLM (varies with output port).
A_{eff}	Effective area of mode.
B_s	Electrostriction-induced birefringence.
f_{pm}	Phase-modulation frequency.
G	Gain (optical).
ℓ_{eff}	Effective nonlinear interaction length ($= \frac{1}{\alpha}[1 - \exp(-\alpha\ell)]$).
ℓ'_{eff}	Effective nonlinear interaction length of folded loop ($= \frac{1}{\alpha}[1 - \exp(-2\alpha\ell)]$).
ℓ_{loop}	Length of NOLM loop.
L_b	Polarization beat length.
L_{span}	Fiber-span loss.
L_{VOA}	VOA loss.
n_2	Nonlinear refractive index (units: m^2/W).
$\langle P \rangle$	Average power of signal.
$P_i^{(\infty)}$	Steady-state power level in NALM chain.
P_{peak}	Peak power of pulse.
R_b	Bit rate of WDM channel.
T_{pulse}	Pulse period.

References

- [1] J. W. Hans, G. Shanlov, E. A. Kuzin, and J. Sanchez-Mondragon, “Vector soliton fiber lasers,” *Optics Letters*, vol. 24, no. 6, pp. 376–8, 1999.
- [2] E. A. Kuzin, B. I. Escamilla, D. E. Garcia-Gomez, and J. W. Haus, “Fiber laser mode locked by a Sagnac interferometer with nonlinear polarization rotation,” *Optics Letters*, vol. 26, no. 20, pp. 1559–61, Oct. 2001.
- [3] N. J. Doran and D. Wood, “Nonlinear-optical loop mirror,” *Optics Letters*, vol. 13, no. 1, pp. 56–58, Jan. 1988.
- [4] M. E. Fermann, F. Haberl, M. Hofer, and H. Hochreiter, “Nonlinear amplifying loop mirror,” *Optics Letters*, vol. 15, no. 13, pp. 752–54, Jul. 1990.
- [5] D. J. Richardson, R. I. Laming, and D. N. Payne, “Very low threshold Sagnac switch incorporating an erbium doped fibre amplifier,” *Electronics Letters*, vol. 26, no. 21, pp. 1779–81, Oct. 1990.
- [6] L. Stampoulidis, K. Vyrsoinos, P. Bakopoulos, G. Guekos, and H. Avramopoulos, “Optical pulse compression in a polarization insensitive non-linear loop mirror,” *Optics Communications*, vol. 238, no. 1/3, pp. 105–11, Aug. 2004.
- [7] T. Sakamoto, F. Futami, K. Kikuchi, S. Takeda, Y. Sugaya, and S. Watanabe, “All-optical wavelength conversion of 500-fs pulse trains by using a nonlinear-optical loop mirror composed of a highly nonlinear DSF,” *IEEE Photonics Technology Letters*, vol. 13, no. 5, pp. 502–04, May 2001.
- [8] I. Shake, H. Takara, K. Uchiyama, S. Kawanishi, and Y. Yamabayashi, “Vibration-insensitive nonlinear optical loop mirror utilizing reflective scheme,” *IEEE Photonics Technology Letters*, vol. 12, no. 5, pp. 555–57, May 2000.

- [9] H. Sotobayashi, C. Sawaguchi, Y. Koyamada, and W. Chujo, "Ultrafast walk-off-free nonlinear optical loop mirror by a simplified configuration for 320-gbit/s time-division multiplexing signal demultiplexing," *Optics Letters*, vol. 27, no. 17, pp. 1555–57, Sep. 2002, (Edited abstract).
- [10] S. Boscolo, J. H. B. Nijhof, and S. K. Turitsyn, "Autosoliton transmission in dispersion-managed systems guided by in-line nonlinear optical loop mirrors," *Optics Letters*, vol. 25, no. 17, pp. 1240–42, Sep. 2000.
- [11] M. Jinno and M. Abe, "All-optical regenerator based on nonlinear fibre Sagnac interferometer," *Electronics Letters*, vol. 28, no. 14, pp. 1350–52, Jul. 1992.
- [12] B. E. Olsson, N. Lagerqvist, A. Boyle, and P. A. Andrekson, "Elimination of acoustic sensitivity in nonlinear optical loop mirrors," *Journal of Lightwave Technology*, vol. 17, no. 2, pp. 343–46, Feb. 1999.
- [13] J. H. Mullins, "A Bell System optical fiber system—Chicago installation." in *NTC '77 Conference Record, 5-7 Dec. 1977, Los Angeles, CA, USA*. New York, NY, USA : IEEE, 1977, 1977, pp. 14:1/1–4.
- [14] M. I. Schwartz, W. A. Reenstra, J. H. Mullins, and J. S. Cook, "The Chicago lightwave communications project," *Bell System Technical Journal*, vol. 57, no. 6, pp. 1881–88, Jul./Aug. 1978.
- [15] Nippon Telegraph and Telephone Corp. (2006, Sep.) "14 Tbps over a single optical fiber: Successful demonstration of World's largest capacity". [Online]. Available: <http://www.ntt.co.jp/news/news06e/0609/060929a.html>
- [16] N. S. Bergano and C. R. Davidson, "Wavelength division multiplexing in long-haul transmission systems," *Journal of Lightwave Technology*, vol. 14, no. 6, pp. 1299–308, Jun. 1996.
- [17] L. Kazovsky, S. Benedetto, and A. Willner, *Optical fiber communication systems*. Artech House, Inc., 1996, pp. 529–602.
- [18] R. Ramaswami and K. N. Sivarajan, *Optical Networks: A practical perspective*. Academic Press, 1998.
- [19] N. S. Bergano, "Wavelength division multiplexing in long-haul transoceanic transmission systems," *Journal of Lightwave Technology*, vol. 23, no. 12, pp. 4125–39, Dec. 2005.
- [20] K. Nagayama, M. Kakui, M. Matsui, T. Saitoh, and Y. Chigusa, "Ultra-low-loss (0.1484 dB/km) pure silica core fibre and extension of transmission distance," *Electronics Letters*, vol. 38, no. 20, pp. 1168–69, Sep. 2002.

- [21] O. Leclerc, B. Lavigne, E. Balmefrezol, P. Brindel, L. Pierre, D. Rouvillain, and F. Segueineau, "Optical regeneration at 40 gb/s and beyond," *Journal of Lightwave Technology*, vol. 21, no. 11, pp. 2779–90, Nov. 2003.
- [22] C. R. Giles and E. Desurvire, "Propagation of signal and noise in concatenated erbium-doped fiber optical amplifiers," *Journal of Lightwave Technology*, vol. 9, no. 2, pp. 147–54, Feb. 1991.
- [23] T. Y. Li, "The impact of optical amplifiers on long-distance lightwave telecommunications," *Proceedings of the IEEE*, vol. 81, no. 11, pp. 1568–79, Nov. 1993.
- [24] L. Kazovsky, S. Benedetto, and A. Willner, *Optical fiber communication systems*. Artech House, Inc., 1996, pp. 578–84.
- [25] A. E. Willner and S.-M. Hwang, "Transmission of many WDM channels through a cascade of edfa's in long-distance links and ring networks," *Journal of Lightwave Technology*, vol. 13, no. 5, pp. 802–16, May 1995.
- [26] A. R. Chraplyvy, J. A. Nagel, and R. W. Tkach, "Equalization in amplified WDM lightwave transmission systems," *IEEE Photonics Technology Letters*, vol. 4, no. 8, pp. 920–22, Aug. 1992.
- [27] A. R. Chraplyvy, R. W. Tkach, K. C. Reichmann, P. D. Magill, and J. A. NAGEL, "End-to-end equalization experiments in amplified wdm lightwave systems," *IEEE Photonics Technology Letters*, vol. 5, no. 4, pp. 428–29, Apr. 1993.
- [28] R. Ramaswami and K. N. Sivarajan, *Optical Networks: A practical perspective*. Academic Press, 1998, pp. 210–14.
- [29] A. M. Vengsarkar, J. R. Pedrazzani, J. B. Judkins, P. J. Lemaire, N. S. Bergano, and C. R. Davidson, "Long-period fiber-grating-based gain equalizers," *Optics Letters*, vol. 21, no. 5, pp. 336–8, Mar. 1996.
- [30] P. F. Wysocki, J. B. Judkins, R. P. Espindola, M. Andrejco, and A. M. Vengsarkar, "Broadband erbium-doped fiber amplifier flattened beyond 40 nm using long-period grating filter," *IEEE Photonics Technology Letters*, vol. 9, no. 10, pp. 1343–5, Oct. 1997.
- [31] M. K. Pandit, K. S. Chiang, Z. H. Chen, and S. P. Li, "Tunable long-period fiber gratings for EDFA gain and ASE equalization," *Microwave and Optical Technology Letters*, vol. 25, no. 3, pp. 181–4, May 2000.
- [32] P. G. Verly, "Design of a robust thin-film interference filter for erbium-doped fiber amplifier gain equalization," *Applied Optics*, vol. 41, no. 16, pp. 3092–6, Jun. 2002.

- [33] R. B. Sargent, "Recent advances in thin film filters," in *Optical Fiber Communication Conference (OFC), 23-27 Feb. 2004, Los Angeles, CA, USA*. Washington, DC, USA : Opt. Soc. America, 2004, 2004, p. TuD6.
- [34] B. Bakhshi, M. Manna, G. Mohs, D. I. Kovsh, R. L. Lynch, M. Vaa, E. A. Golovchenko, W. W. Patterson, W. T. Anderson, P. Corbett, S. J. Jiang, M. M. Sanders, H. F. Li, G. T. Harvey, A. Lucero, and S. M. Abbott, "First dispersion-flattened transpacific undersea system: from design to terabit/s field trial," *Journal of Lightwave Technology*, vol. 22, no. 1, pp. 233–41, Jan. 2004.
- [35] S. K. Liaw, K. P. Ho, and S. Chi, "Dynamic power-equalized EDFA module based on strain tunable fiber bragg gratings," *IEEE Photonics Technology Letters*, vol. 11, no. 7, pp. 797–799, 1999 1999.
- [36] H. S. Kim, S. H. Yun, H. K. Kim, N. Park, and B. Y. Kim, "Actively gain-flattened erbium-doped fiber amplifier over 35 nm by using all-fiber acoustooptic tunable filters," *IEEE Photonics Technology Letters*, vol. 10, no. 6, pp. 790–792, Jun. 1998.
- [37] S. H. Huang, X. Y. Zou, S. M. Hwang, A. E. Willner, Z. Bao, and D. A. Smith, "Experimental demonstration of dynamic network equalization of three 2.5-gb/s WDM channels over 1000 km using acoustooptic tunable filters," *IEEE Photonics Technology Letters*, vol. 8, no. 9, pp. 1243–5, Sep. 1996.
- [38] L. Y. Lin and E. L. Goldstein, "Opportunities and challenges for MEMS in lightwave communications," *IEEE Journal of Selected Topics in Quantum Electronics*, vol. 8, no. 1, pp. 163–72, Jan./Feb. 2002.
- [39] J. E. Ford and J. A. Walker, "Dynamic spectral power equalization using micro-optomechanics," *IEEE Photonics Technology Letters*, vol. 10, no. 10, pp. 1440–2, Oct. 1998.
- [40] C. R. Doerr, M. Cappuzzo, E. Laskowski, A. Paunescu, L. Gomez, L. W. Stulz, and J. Gates, "Dynamic wavelength equalizer in silica using the single-filtered-arm interferometer," *IEEE Photonics Technology Letters*, vol. 11, no. 5, pp. 581–3, 1999 1999.
- [41] K. Inoue, T. Kominato, and H. Toba, "Tunable gain equalization using a Mach-Zehnder optical filter in multistage fiber amplifiers," *IEEE Photonics Technology Letters*, vol. 3, no. 8, pp. 718–20, Aug. 1991.
- [42] C. R. Doerr, L. W. Stulz, R. Pafchek, L. Gomez, M. Cappuzzo, A. Paunescu, E. Laskowski, L. Buhl, H. K. Kim, and S. Chandrasekhar, "An automatic 40-wavelength channelized equalizer," *IEEE Photonics Technology Letters*, vol. 12, no. 9, pp. 1195–7, Sep. 2000.

- [43] K. Suzuki, T. Kitoh, S. Suzuki, Y. Inoue, Y. Hibino, T. Shibata, A. Mori, and M. Shimizu, "PLC-based dynamic gain equaliser consisting of integrated Mach-Zehnder interferometers with C- and L-band equalising range," *Electronics Letters*, vol. 38, no. 18, pp. 1030–31, Aug. 2002.
- [44] S. Li, K. S. Chiang, and W. A. Gambling, "Gain flattening of an erbium-doped fiber amplifier using a high-birefringence fiber loop mirror," *IEEE Photonics Technology Letters*, vol. 13, no. 9, pp. 942–4, 2001.
- [45] J. K. Bae, J. H. Bae, S. H. Kim, N. Park, and S. B. Lee, "Dynamic EDFA gain-flattening filter using two LPFGs with divided coil heaters," *IEEE Photonics Technology Letters*, vol. 17, no. 6, pp. 1226–28, Jun. 2005.
- [46] Y. J. Rao, A. Z. Hu, and Y. C. Niu, "A novel dynamic LPFG gain equalizer written in a bend-insensitive fiber," *Optics Communications*, vol. 244, no. 1, pp. 137–40, Jan. 2005.
- [47] Y. Jeong, H. R. Kim, S. Baek, Y. Kim, Y. W. Lee, B. Lee, and S. D. Lee, "Electrical modulation of an etched long-period fiber grating with a liquid-crystal cladding," in *LEOS 2001. 14th Annual Meeting of the IEEE Lasers and Electro-Optics Society, 12-13 Nov. 2001, San Diego, CA, USA*, vol. 2. Piscataway, NJ, USA : IEEE, 2001, 2001, pp. 780–81.
- [48] T. Zhu and Y. J. Rao, "All-fiber dynamic gain equalizer based on a twisted long period grating written by high frequency CO₂ laser pulses," in *OFCNFOEC 2006. 2006 Optical Fiber Communication Conference and National Fiber Optic Engineers Conference, 5-10 March 2006, Anaheim, CA, USA*. Piscataway, NJ, USA : IEEE, 2006, 2006.
- [49] J. Ferry, J. L. Pleumeekers, A. Mathur, A. G. Dentai, and P. W. Evans, "Large-scale photonic integrated circuits: a new architecture for commercial telecommunications networks," *Photonics Spectra*, vol. 40, no. 3, pp. 78–82, Mar. 2006.
- [50] R. Nagarajan, C. H. Joyner, R. P. Schneider, J. S. Bostak, T. Butrie, A. G. Dentai, V. G. Dominic, P. W. Evans, M. Kato, M. Kauffman, D. J. H. Lambert, S. K. Mathis, A. Mathur, R. H. Miles, M. L. Mitchell, M. J. Missey, S. Murthy, A. C. Nilsson, F. H. Peters, S. C. Pennypacker, J. L. Pleumeekers, R. A. Salvatore, R. K. Schlenker, R. B. Taylor, H. S. Tsai, M. F. V. Leeuwen, J. Webjorn, M. Ziari, D. Perkins, J. Singh, S. G. Grubb, M. S. Reffle, D. G. Mehuys, F. A. Kish, and D. F. Welch, "Large-scale photonic integrated circuits," *IEEE Journal of Selected Topics in Quantum Electronics*, vol. 11, no. 1, pp. 50–65, Jan./Feb. 2005.
- [51] G. B. Malykin, "Earlier studies of the Sagnac effect," *Uspekhi Fizicheskii Nauk*, vol. 40, no. 3, pp. 317–21, Mar. 1997.

- [52] E. J. Post, "Sagnac effect," *Reviews of Modern Physics*, vol. 39, no. 2, pp. 475–93, Apr. 1967.
- [53] S. Rashleigh, "Origins and control of polarization effects in single-mode fibers," *Journal of Lightwave Technology*, vol. LT-1, no. 2, pp. 312–31, Jun. 1983.
- [54] H. C. Lefevre, "Single-mode fibre fractional wave devices and polarisation controllers," *Electronics Letters*, vol. 16, no. 20, pp. 778–80, Sep. 1980.
- [55] R. A. Bergh, H. C. Lefevre, and H. J. Shaw, "An overview of fiber-optic gyroscopes," *Journal of Lightwave Technology*, vol. LT/2, no. 2, pp. 91–107, Apr 1984.
- [56] —, "All-single-mode fiber-optic gyroscope," *Optics Letters*, vol. 6, no. 4, pp. 198–200, Apr. 1981.
- [57] R. G. Priest, "Analysis of fiber interferometer utilizing 3×3 fiber coupler," *IEEE Transactions on Microwave Theory and Techniques*, vol. MTT/30, no. 10, pp. 1589–91, Oct. 1982.
- [58] R. W. Boyd, *Nonlinear optics*. Academic Press, 1992, ch. 1.
- [59] G. P. Agrawal, *Nonlinear fiber optics*, 2nd ed. Academic Press, 1995, pp. 42–43.
- [60] K. S. Kim, R. H. Stolen, W. A. Reed, and K. W. Quoi, "Measurement of the nonlinear index of silica-core and dispersion-shifted fibers," *Optics Letters*, vol. 19, no. 4, pp. 257–59, Feb. 1994.
- [61] T. Okuno, M. Onishi, T. Kashiwada, S. Ishikawa, and M. Nishimura, "Silica-based functional fibers with enhanced nonlinearity and their applications," *IEEE Journal of Selected Topics in Quantum Electronics*, vol. 5, no. 5, pp. 1385–91, Sep./Oct. 1999.
- [62] K. Otsuka, "Nonlinear antiresonant ring interferometer," *Optics Letters*, vol. 8, no. 9, pp. 471–73, Sep. 1983.
- [63] G. P. Agrawal, *Nonlinear fiber optics*, 2nd ed. Academic Press, 1995, p. 376.
- [64] S. V. Chernikov and J. R. Taylor, "Measurement of normalization factor of n_2 for random polarization in optical fibers," *Optics Letters*, vol. 21, no. 19, pp. 1559–61, Oct. 1996.
- [65] S. G. Evangelides, L. F. Mollenauer, J. P. Gordon, and N. S. Bergano, "Polarization multiplexing with solitons," *Journal of Lightwave Technology*, vol. 10, no. 1, pp. 28–35, Jan. 1992.
- [66] P. K. A. Wai, C. R. Menyuk, and H. H. Chen, "Stability of solitons in randomly varying birefringent fibers," *Optics Letters*, vol. 16, no. 16, pp. 1231–33, Aug. 1991.

- [67] R. A. Bergh, "All-fiber gyroscope with optical-Kerr-effect compensation," Ph.D. dissertation, Stanford University, May 1983.
- [68] G. P. Agrawal, *Nonlinear fiber optics*, 2nd ed. Academic Press, 1995, pp. 239–43.
- [69] B. Crosignani and A. Yariv, "Kerr effect and chromatic dispersion in fiber-optic gyroscopes," *Journal of Lightwave Technology*, vol. LT/3, no. 4, pp. 914–18, Aug. 1985.
- [70] N. J. Frigo, H. F. Taylor, L. Goldberg, J. F. Weller, and S. C. Rashleigh, "Optical Kerr effect in fiber gyroscopes: effects of nonmonochromatic sources," *Optics Letters*, vol. 8, no. 2, pp. 119–21, Feb. 1983.
- [71] H. J. R. Dutton, *Understanding Optical Communications*. Prentice Hall PTR, 1999.
- [72] A. R. Chraplyvy, "Limitations on lightwave communications imposed by optical-fiber nonlinearities," *Journal of Lightwave Technology*, vol. 8, no. 10, pp. 1548–57, Oct. 1990.
- [73] J. Toulouse, "Optical nonlinearities in fibers: review, recent examples, and systems applications," *Journal of Lightwave Technology*, vol. 23, no. 11, pp. 3625–41, Nov. 2005.
- [74] D. M. Baney and J. Stimple, "WDM EDFA gain characterization with a reduced set of saturating channels," *IEEE Photonics Technology Letters*, vol. 8, no. 12, pp. 1615–17, Dec. 1996.
- [75] A. R. Chraplyvy, R. W. Tkach, L. L. Buhl, and R. C. Alfarness, "Phase modulation to amplitude modulation conversion of CW laser light in optical fibres." *Electronics Letters*, vol. 22, no. 8, pp. 409–11, Apr. 1986.
- [76] K. Tajima, "Self-amplitude modulation in PSK coherent optical transmission systems," *Journal of Lightwave Technology*, vol. LT-4, no. 7, pp. 900–04, Jul. 1986.
- [77] A. R. Chraplyvy, R. W. Tkach, L. L. Buhl, and R. C. Alfarness, "Phase modulation to amplitude modulation conversion of CW laser light in optical fibres," *Electronics Letters*, vol. 22, no. 8, pp. 409–11, Apr. 1986.
- [78] B. Jopson and A. Gnauck, "Dispersion compensation for optical fiber systems," *IEEE Communications Magazine*, vol. 33, no. 6, pp. 96–102, Jun. 1995.
- [79] W. K. Marshall, B. Crosignani, and A. Yariv, "Laser phase noise to intensity noise conversion by lowest-order group-velocity dispersion in optical fiber: exact theory," *Optics Letters*, vol. 25, no. 3, pp. 165–67, Feb. 2000.
- [80] G. J. Meslener, "Chromatic dispersion induced distortion of modulated monochromatic light employing direct detection," *IEEE Journal of Quantum Electronics*, vol. QE/20, no. 10, pp. 1208–16, Oct. 1984.

- [81] M. Murakami and M. Amemiya, "Simple and accurate zero dispersion wavelength measurement for long haul optical amplifier systems using induced phase to amplitude modulation conversion," *Electronics Letters*, vol. 31, no. 8, pp. 666–68, Apr. 1995.
- [82] B. J. Vakoc, "Development of a novel Sagnac interferometer-based fiber-optic acoustic sensor array," Ph.D. dissertation, Stanford University, 2001.
- [83] M. Martinelli, "A universal compensator for polarization changes induced by birefringence on a retracing beam," *Optics Communications*, vol. 72, no. 6, pp. 341–44, Aug. 1989.
- [84] B. J. Vakoc, M. J. F. Digonnet, and G. S. Kino, "Demonstration of a folded Sagnac sensor array immune to polarization-induced signal fading," *Applied Optics*, vol. 42, no. 36, pp. 7132–36, Dec. 2003.
- [85] G. R. Fowles, *Introduction to Modern Optics*. Courier Dover Publications, 1989, pp. 33–38.
- [86] C. B. Clausen, J. Povlsen, and K. Rottwitt, "Polarization sensitivity of the nonlinear amplifying loop mirror," *Optics Letters*, vol. 21, no. 19, pp. 1535–37, Oct. 1996.
- [87] D. A. Fishman and J. A. Nagel, "Degradations due to stimulated Brillouin scattering in multigigabit intensity-modulated fiber-optic systems," *Journal of Lightwave Technology*, vol. 11, no. 11, pp. 1721–28, Nov. 1993.
- [88] Y. Aoki, K. Tajima, and I. Mito, "Input power limits of single-mode optical fibers due to stimulated Brillouin scattering in optical communication systems," *Journal of Lightwave Technology*, vol. 6, no. 5, pp. 710–19, May 1988.
- [89] R. W. Boyd, *Nonlinear optics*. Academic Press, 1992, pp. 327–31.
- [90] E. L. Buckland and R. W. Boyd, "Electrostrictive contribution to the intensity-dependent refractive index of optical fibers," *Optics Letters*, vol. 21, no. 15, pp. 1117–19, 1996.
- [91] —, "Measurement of the frequency response of the electrostrictive nonlinearity in optical fibers," *Optics Letters*, vol. 22, no. 10, pp. 676–78, 1997.
- [92] E. Dianov, A. Luchnikov, A. Pilipetskii, and A. Starodumov, "Electrostriction mechanism of soliton interaction in optical fibers," *Optics Letters*, vol. 15, no. 6, pp. 314–16, 1990.
- [93] A. Fellegara, A. Melloni, and M. Martinelli, "Measurement of the frequency response induced by electrostriction in optical fibers," *Optics Letters*, vol. 22, no. 21, pp. 1615–17, 1997.
- [94] A. Melloni, M. Martinelli, and A. Fellegara, "Frequency characterization of the nonlinear refractive index in optical fiber," *Fiber and Integrated Optics*, vol. 18, no. 1, pp. 1–13, 1999.

- [95] G. P. Agrawal, *Nonlinear fiber optics*, 2nd ed. Academic Press, 1995, pp. 370–403.
- [96] E. Dianov, A. Luchnikov, A. Pilipetskii, and A. Starodumov, “Long-range interaction of soliton pulse trains a single mode fiber,” *Soviet Lightwave Communication*, vol. 1, p. 37, 1991.
- [97] L. du Mouza and Y. Jaouen, “Measurement of the dynamic frequency shift generated by the electrostriction-induced acoustic effect in an optical fiber,” in *ECOC 97, 22–25 September 1997*, no. 448, 1997, pp. 107–110.
- [98] L. du Mouza, Y. Jaouen, and C. Chabran, “Transverse Brillouin effect characterization in optical fibers and its geometrical aspects,” *IEEE Photonics Technology Letters*, vol. 10, no. 10, pp. 1455–57, 1998.
- [99] Y. Jaouen and L. du Mouza, “Transverse Brillouin effect produced by electrostriction in optical fibers and its impact on soliton transmission systems,” *Optical Fiber Technology*, vol. 7, no. 3, pp. 141–69, 2001.
- [100] E. A. Golovchenko and A. N. Pilipetskii, “Acoustic effect and the polarization of adjacent bits in soliton communication lines,” *Journal of Lightwave Technology*, vol. 12, no. 6, pp. 1052–56, Jun. 1994.
- [101] K. Smith and L. Mollenauer, “Experimental observation of soliton interaction over long fiber paths: discovery of a long-range interaction,” *Optics Letters*, vol. 14, no. 22, pp. 1284–86, Nov. 1989.
- [102] P. D. Townsend, A. J. Poustie, P. Hardman, and K. Blow, “Measurement of the refractive-index modulation generated by electrostriction-induced acoustic waves in optical fibers,” *Optics Letters*, vol. 21, no. 5, pp. 333–35, Mar. 1996.
- [103] A. S. Dement’ev, E. K. Maldutis, and S. V. Sakalauskas, “Electrostrictive birefringence in isotropic solids induced by high-intensity laser radiation,” *Soviet Journal of Quantum Electronics*, vol. 8, no. 4, pp. 449–53, Apr. 1978.
- [104] D. Zwillinger, Ed., *Standard mathematical tables and formulae*. CRC Press, 1996, ch. 6, p. 516.
- [105] R. Shelby, M. Levenson, and P. Bayer, “Resolved forward Brillouin scattering in optical fibers,” *Physical Review Letters*, vol. 54, no. 9, pp. 939–42, Mar. 1985.
- [106] —, “Guided acoustic-wave Brillouin scattering,” *Physical Review B (Condensed Matter)*, vol. 31, no. 8, pp. 5244–52, Apr. 1985.

- [107] A. Poustie, "Guided acoustic-wave Brillouin scattering with optical pulses," *Optics Letters*, vol. 17, no. 8, pp. 574–76, Apr. 1992.
- [108] A. J. Poustie, "Bandwidth and mode intensities of guided acoustic-wave Brillouin scattering in optical fibers," *Journal of the Optical Society of America B: Optical Physics*, vol. 10, no. 4, pp. 691–696, April 1993.
- [109] "Corning SMF-28 fiber data sheet," Available at www.corning.com, Oct. 1999.
- [110] C. R. Menyuk, "Nonlinear pulse propagation in birefringent optical fibers," *IEEE Journal of Quantum Electronics*, vol. QE/23, no. 2, pp. 174–76, Feb 1987.
- [111] G. P. Agrawal, *Nonlinear fiber optics*, 2nd ed. Academic Press, 1995, pp. 316–21.
- [112] P. Devgan, R. Tang, V. S. Grigoryan, and P. Kumar, "Highly efficient multichannel wavelength conversion of DPSK signals," *Journal of Lightwave Technology*, vol. 24, no. 10, pp. 3677–82, 2006.
- [113] V. S. Grigoryan, P. S. Cho, and I. Shpantzer, "Nonlinear penalty reduction of RZ-DBPSK versus RZ-OOK modulation format in fiber communications," in *ECOC 2002. 28th European Conference on Optical Communication, 8-12 Sept. 2002, Copenhagen, Denmark*, P. Danielsen, Ed. Piscataway, NJ, USA : IEEE, 2002, 2002.
- [114] I. Kang, C. Xie, C. Dorrer, and A. Gnauck, "Implementations of alternate-polarisation differential-phase-shift-keying transmission," *Electronics Letters*, vol. 40, no. 5, pp. 333–35, Mar. 2004.
- [115] J. Leibrich, C. Wree, and W. Rosenkranz, "CF-RZ-DPSK for suppression of XPM on dispersion-managed long-haul optical WDM transmission on standard single-mode fiber," *IEEE Photonics Technology Letters*, vol. 14, no. 2, pp. 155–57, Feb. 2002.
- [116] J. H. Sinsky, A. Adamiecki, A. Gnauck, C. A. Burrus, J. Leuthold, O. Wohlgenuth, S. Chandrasekhar, and A. Umbach, "RZ-DPSK transmission using a 42.7-Gb/s integrated balanced optical front end with record sensitivity," *Journal of Lightwave Technology*, vol. 22, no. 1, pp. 180–85, Jan. 2004.
- [117] X. Wei, A. H. Gnauck, D. M. Gill, X. Liu, U. V. Koc, S. Chandrasekhar, G. Raybon, and J. Leuthold, "Optical $\pi/2$ -DPSK and its tolerance to filtering and polarization-mode dispersion," *IEEE Photonics Technology Letters*, vol. 15, no. 11, pp. 1639–41, Nov. 2003.
- [118] C. Wree, N. Hecker-Denschlag, E. Gottwald, P. Krummrich, J. Leibrich, E. D. Schmidt, B. Lankl, and W. Rosenkranz, "High spectral efficiency 1.6-b/s/Hz transmission (8 x 40 Gb/s with a 25-GHz grid) over 200-km SSMF using RZ-DQPSK and polarization multiplexing," *IEEE Photonics Technology Letters*, vol. 15, no. 9, pp. 1303–05, Sep. 2003.

- [119] B. Zhu, L. E. Nelson, S. Stulz, A. H. Gnauck, C. Doerr, J. Leuthold, L. Gruner-Nielsen, M. O. Pedersen, J. Kim, and R. L. Lingle, "High spectral density long-haul 40-Gb/s transmission using CSRZ-DPSK format," *Journal of Lightwave Technology*, vol. 22, no. 1, pp. 208–14, Jan. 2004.
- [120] Y. Yamamoto and T. Kimura, "Coherent optical fiber transmission systems," *IEEE Journal of Quantum Electronics*, vol. QE/17, no. 6, pp. 919–35, Jun. 1981.
- [121] J. Salz, "Coherent lightwave communications," *AT&T Technical Journal*, vol. 64, no. 10, pp. 2153–209, Dec. 1985.
- [122] E. H. Lee, K. H. Kim, and H. K. Lee, "Nonlinear effects in optical fiber: advantages and disadvantages for high capacity all-optical communication application," *Optical and Quantum Electronics*, vol. 34, no. 12, pp. 1167–74, Dec. 2002.
- [123] G. P. Agrawal, *Nonlinear fiber optics*, 2nd ed. Academic Press, 1995.
- [124] L. G. L. Wegener, M. L. Povinelli, A. G. Green, P. P. Mitra, J. B. Stark, and P. B. Littlewood, "The effect of propagation nonlinearities on the information capacity of WDM optical fiber systems: cross-phase modulation and four-wave mixing." *Physica D*, vol. 189, no. 1/2, pp. 81–99, Feb. 2004.
- [125] M. C. Wu and W. I. Way, "Fiber nonlinearity limitations in ultra-dense WDM systems," *Journal of Lightwave Technology*, vol. 22, no. 6, pp. 1483–1497, Jun. 2004.